UNIVERSITÀ DEGLI STUDI DELL'INSUBRIA

PhD Program in Chemical and Environmental Sciences (XXXIV Cycle)

Close-range and satellite remote sensing techniques for the cryosphere monitoring

PhD Thesis

Supervisor: Prof. Mauro Guglielmin

Candidate: Giulia Tarca
Nr: 739159

Academic year: 2020/2021

CONTENTS

1. Introduction

1.1. Motivation and aims

"Cryosphere" comes from the Greek "krios", meaning cold, and is defined as the portions of Earth's surface where water is in solid form. It is composed by snow cover, glaciers, ice sheets, ice caps, ice shelves, frozen lakes and rivers (freshwater ice), sea ice, icebergs, permafrost and frozen ground (Barry & Gan, 2011) (Fig. 1).

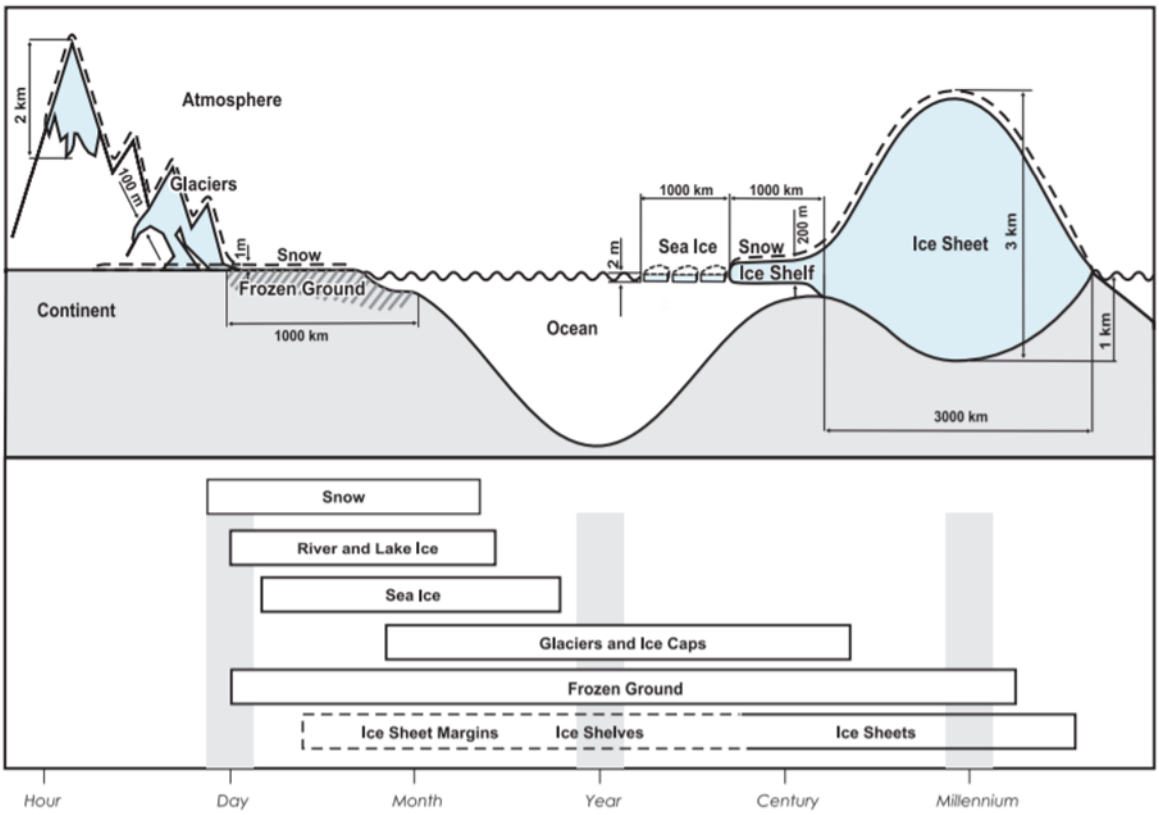

Figure 1 Components of the cryosphere and their spatial and temporal scales. Source: IPCC (2006).

The cryosphere covers a mean total area of 68 million km^2 (ranging between 78 million in the northern winter and 58 million in the northern summer), about the 13% of the Earth's surface (Ohmura, 2014) and ice stores about 75% of the world's freshwater (Kotwicki, 2009).

In the last decades, climate change has impacted the cryosphere, whose components are sensitive to air temperatures and precipitation changes, with mass loss from glaciers and ice sheets, reduction in snow cover and Arctic sea ice extent and thickness, and increased permafrost temperature (IPCC, 2019). The changes experienced by the cryospheric components take place at different spatial scales, from sub-meters to thousands of kilometers, and different temporal scales, from daily to millennial or longer (Fig. 1).

Due to the importance of the cryosphere in Earth's system and its sensitivity to climate change, it is of primary importance the monitoring of the state and evolution of its components, that requires investigations on a wide range of spatial and temporal scales.

The aim of this thesis was to use different remote sensing techniques to investigate and monitor two important cryospheric components, snow cover and glaciers, with a particular focus on the supraglacial debris for these latter. We used mainly close-range remote sensing techniques, as timelapse photography, ground-based thermal imaging, ground-based photography, UAV imaging, but also satellite remote sensing, in some cases integrated with field measurements and observations, in order to be able to investigate snow cover and glaciers at a high spatial and/or temporal resolution. The research was carried out both in polar (Antarctic) and in high-mountain (Alpine) areas. Four case studies are presented in the thesis, the first regarding snow cover in Antarctica, the other three regarding glaciers in the Alps.

The term "remote sensing" can be defined as the "acquisition of physical data of an object without touch or contact" (Lintz & Simonett, 1976) or "the practice of deriving information about the Earth's land and water surfaces using images acquired from an overhead perspective, using electromagnetic radiation in one or more regions of the electromagnetic spectrum, reflected or emitted from the Earth's surface" (Campbell & Wynne, 2011). So

remote sensing refers to obtaining information about objects of areas by using electromagnetic radiation, emitted or reflected, without being in direct contact with the object or area. Remote sensing can be classified based on the platform on which the sensor that acquires data is mounted. While a definition of satellite remote sensing is easy, as it refers to sensors mounted on satellites, for close-range remote sensing, it is difficult to find a straightforward definition although the term is widely used. Breithaupt & Matthews, (2001) used “close-range” to refer to a distance between the sensor and the object lower than 300 m. On one side, satellite remote sensing offers the advantages to cover large areas and gives the possibility to monitor remote areas that are difficult to reach, as the high-mountain and polar areas usually are, on the other side close-range remote sensing techniques can provide high spatial and temporal resolutions that are beyond the capabilities of satellite borne methods, although limited to more restricted areas. The close-range and satellite remote sensing techniques used in this thesis and their application are:

- In the case study (1) we used time lapse photography to investigate the small-scale spatial and temporal variability of snow cover at Signy Island (maritime Antarctica). High-resolution orthophoto and digital elevation models from UAV were also used to map land cover and obtain topographic parameters;
- In the case study (2) we used ground-based thermal imaging (or thermography) to analyse surface temperature distribution and estimate supraglacial debris thickness at high-spatial resolution on a small alpine glacier (Gran Zebrù glacier, Ortles-Cevedale group, Italy). The results were then compared to that obtained from ASTER data;
- In the case study (3) the evolution of the sparse debris cover during the melting season at two small Alpine glaciers (Gran Zebrù and Sforzellina, Ortles-Cevedale group, Italy) and its impact on glacier albedo, ablation and surface temperatures were

investigated. To do so ground-based (handheld) photography and thermal imaging were used, but also field measurements.

- In the case study (4) we used satellite images from the recently launched PlanetScope constellation, offering daily data at high resolution, to monitor small glaciers located in different sectors of the Alps.

1.2. Snow cover and glaciers

1.2.1. Snow cover in maritime Antarctica

Snow cover is an important component of the global climate system, as it modifies energy and moisture fluxes between the ground surface and the atmosphere, and acts as a water store in hydrological systems (Brown and Robinson, 2005). Snow characteristics, such as its high albedo and emissivity (that tend to cool the snow surface), high absorptivity (that in contrast tends to warm the surface), and low thermal conductivity make it an effective insulator of the ground and terrestrial ecosystems below (Zhang, 2005).

The spatial and temporal distribution of snow cover influences the biogeochemical conditions (moisture, temperature, chemistry) in the underlying soil, which in turn can determine the distribution of soil invertebrates and microbiota (Gooseff et al., 2003). It also affects vegetation (Callaghan et al., 2011) by influencing the temperature regime through its insulation qualities and also the availability of water and light (Kappen et al., 1995, Winkler et al., 2000), affecting the species distributions, growing season length and phenology (Borner et al., 2008). Snow cover also has a significant influence on permafrost distribution, temperatures and thickness (Zhang, 2005). A further important feature of snow cover lies in its spatial variability at the local scale, as accumulation, redistribution and ablation processes are affected by features such as microclimate, topography, and characteristics of vegetation (Neumann et al., 2006).

In Antarctica, most of the studies focusing on snow cover have studied snow accumulation on Antarctic sea ice or on glaciers and ice sheets, while only few have studied snow cover in terrestrial habitats, mostly focusing only on the temporal or only on the spatial variability, or covering short periods.

The maritime Antarctica has been recognised as a key region for the assessment and monitoring of climate change and its impacts (Cannone et al., 2006), as this wetter region shows higher sensitivity to climate change than the cold and dry Continental Antarctic, due to its climatic and geographical characteristics (Smith, 1984).

Temperatures measured in the maritime Antarctica (at Orcadas Station, Laurie Island, South Orkney Islands) showed an air warming in the 20th century, with an increase of +0.21°C per decade since 1904 (Turner et al., 2014), while more recent data show a cooling 0.2 °C comparing the decades 1996–2005 and 2006–2015 (Oliva et al., 2017).

In a climate change framework, more detailed studies of snow cover spatial and temporal distribution in maritime Antarctica are required, to understand the climatic conditions and the surface characteristics that influence its variability but also to understand the impact of this variability on underlying ecosystems, soil processes and permafrost.

1.2.2. Alpine glaciers

The European Alps host 4395 glaciers (larger than 0.01 km^2) at present (2015), that cover a total area of 1805.9 km^2, of which 49.4% is found in Switzerland, 20% in Austria, 18% in Italy and 12.6% in France (Paul et al., 2020). In the Alps small glaciers prevail, indeed 92% of the glaciers have an area smaller than 1 km^2, while only 1.6% are larger than 5 km^2 (Paul et al., 2020).

Alpine glaciers have been impacted by climate change. The Greater Alpine Region experienced a temperature increase of 1.2 °C in the 20th century, rising about twice as much as the global mean (Auer et al., 2007). Glaciers in the Alps have been retreating since the end of the Little Ice Age (e.g. Zemp, 2006) and are undergoing a rapid shrinkage and downwasting, with an area loss of ~39 ± 9 $km^2\ a^{-1}$ (~1.8% a^{-1}), regionally variable ice thickness changes (−0.5 to −0.9 m a^{-1}) and a mass loss of 1.3 ± 0.2 Gt a^{-1} between 2000 and 2014 (Sommer et al., 2020).

The reconstructed environmental equilibrium-line altitudes (ELAs) across the European Alps showed a mean of 2980 m a.s.l. in the period 1901-1930, then between 1901−1930 and 1971−2000 it rose by 1.6 m yr^{-1}, being 3094 m a.s.l. in the period 1971−2000 and rising to 3234 m a.s.l. in the last 30 years (1991-2020), rising by 254 m with respect to the period 1901-1930 (Žebre et al., 2021).

Simulations of the future evolution of glaciers in the Alps, based on different climate scenarios, indicate that by 2100 between -63% and -94% of the actual (2017) glacier volume and between -62% and -91% of the glacier area will be lost (Zekollari et al., 2019). The environmental ELA is projected to rise to 3288 m a.s.l., 3484 m a.s.l. or 3880 m a.s.l. under three different emission scenarios (Žebre et al., 2021).

The retreat of Alpine glaciers has important impacts on ecosystems (e.g. Cannone et al., 2008; Franzetti et al., 2020), on river runoff and thus on hydropower production (e.g. Patro et al.,

2018; Schaefli et al., 2019; Puspitarini et al., 2020) and agriculture (e.g. Beniston et al., 2012), on natural hazards (e.g. Chiarle et al., 2007; Gobiet et al., 2014), but also on tourism (e.g. Ritter et al., 2012; Pröbstl-Haider et al., 2016).

In this context, small glaciers are showing largest relative area decrease respect to the large glaciers (e.g. Linsbauer et al., 2021). For the Italian glaciers, Smiraglia et al. (2015) reported strongest area reduction for small glaciers (< 1 km^2) in the period from 1959-1961 to 2005-2011. Also, Carturan et al. (2013a) found a tendence to a greater relative area loss with decreasing initial size for the glaciers of the Ortles-Cevedale (Italian Alps) in the period 1987-2009. In the Swiss Alps, Linsbauer et al. (2021), found an area decrease of -60% for glaciers <0.1 km^2, -39% for glaciers 0.1-1 km^2, -21% for glaciers 1-10 km^2 and -13% for glaciers >10 km^2 in the period between 1973 and 2016. However, some studies found that very small glaciers in some sectors of the Alps seem resilient to climate warming, as reported by Carturan et al. (2013b), Colucci (2016), Colucci et al. (2021) and De Marco et al. (2020) in the Julian Alps (Eastern Italian Alps), and by Scotti et al. (2014) in the Orobie (Central Italian Alps), both being maritime areas (where mean annual precipitation is high), with glaciers showing higher sensitivity to winter precipitation than to summer temperature, but also by Scotti & Brardinoni (2018) in the Viola Valley (Central Italian Alps), suggesting a climate-glacier decoupling thanks to their location in sheltered sites surrounded by high and steep rock walls or in niches, with increased convexity and roughness, where wind drift accumulation is favoured but also avalanching.

Therefore, in this thesis we decided to focus on small glaciers (case studies (2), (3) and (4)), that despite their relevance are the less studied, since Alpine glacier research focuses mainly

on medium and large glaciers (Huss & Fischer, 2016). In particular in the case studies (2) and (3) we focus on small Alpine glaciers located in the Ortles-Cevedale group (Central Italian Alps, Italy), while in the case study (4) on glaciers located in different sectors of the Alpine chain (Fig. 2).

Figure 2 Examples of some small Alpine glaciers studied in this thesis. From the top to the bottom: Gran Zebrù glacier (Ortles-Cevedale); Sforzellina glacier (Ortles-Cevedale); Pizzo Ferrè glacier (Tambò-Stella); Solda Orientale glacier (Ortles-Cevedale).

The Ortles-Cevedale group is the largest glacierized group of the Italian Alps, covering 76.8 km^2, about 3.5 % of the total Alpine glacier area and it comprises Forni glacier, the largest Italian valley glacier (~11 km^2) (Carturan et al., 2013a). The highest peaks of the mountain group are Ortles (3905 m a.s.l.), Gran Zebrù (3851 m a.s.l.) and Cevedale (3769 m a.s.l.). The glaciers of the Ortles-Cevedale group are undergoing rapid shrinkage (Fig. 3). An area reduction of about 40% was reported by D'Agata et al. (2014) for the period 1954-2007, while Carturan et al. (2013a) reported a reduction of 23% for the period 1987-2009.

Figure 3 Example of the area reduction undergone by Gran Zebrù glacier (Ortles-Cevedale, Italy). At the top photograph from 1907 (A.Corti), at the bottom photograph from 2020. Gran Zebrù glacier is one of the glaciers studied in this thesis (case studies (2), (3) and (4)).

1.2.2.1. Supraglacial debris

Similarly to other regions in the world, as in the Karakoram (Xie et al., 2020), Himalayas (Bolch et al., 2008; Jiang et al., 2018), Caucasus (Stokes et al., 2007) and Patagonia (Glasser et al., 2016), an expansion of the supraglacial debris cover has been reported also in the Alps (Kellerer-Pirklbauer, 2008; Azzoni et al., 2018; Mölg et al., 2019). In Figure 3 is reported as example one of the glaciers studied in this thesis, where it is possible to see the expansion of the supraglacial debris cover between 2003 and 2015.

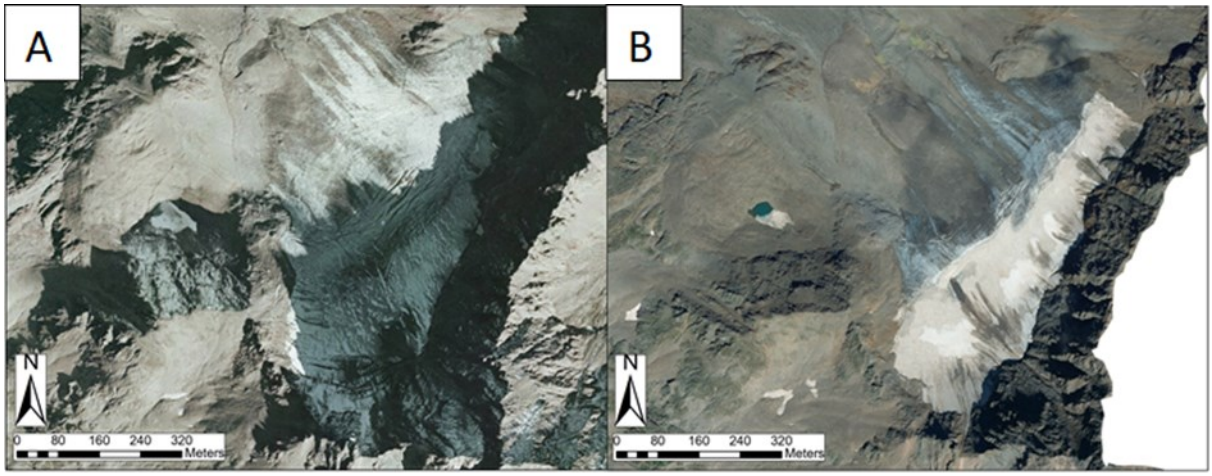

Figure 3 Example of Sforzellina glacier, a small glacier of the Ortles-Cevedale, where it is possible to see the glacier retreat and the supraglacial debris expansion between the orthophoto of 2003 (A) and 2015 (B). Source: Geoportale Regione Lombardia.

Supraglacial debris has not negligible impacts on glaciers. Østrem (1959) found higher ablation rates under thin debris (less than the 'critical thickness') compared to clean ice and decreasing ablation rates under thicker debris covers. The critical thickness is defined as the thickness at which the ablation rate for debris covered ice and debris free ice are equal (e.g. Mattson, 1993). Thin debris increases the melt rate of the underlying ice due to the low albedo of the debris that increases the absorption of the solar radiation and to the rapid transmission of heat to the ice surface, while thicker debris decreases the melt rate as it acts as a barrier to

heat transfer (Clark et al., 1994). A range of critical thicknesses have been measured on different glaciers in the world, with values between 15 mm and 115 mm, decreasing at increasing latitude and elevation, but possibly also influenced by other factors and processes (e.g. meteorological conditions, debris lithology, etc.) (Reznichenko et al., 2010). More recently, other studies showed that a thin debris layer does not enhance glacier melt compared to clean ice, for example in New Zealand (Brook et al., 2013; Hagg et al., 2014) and in the Karakoram (Muhammad et al., 2020). The quantity, distribution and granulometry of debris on the glacier surfaces can be highly variable, from dust particles to boulders having a diameter of different meters and from a minimal presence to the complete cover of a glacier tongue (Paul et al., 2004). When debris covers at least 50% of the ablation zone, a glacier is defined as debris-covered glacier (Kirkbride, 2011). Some debris-covered glaciers are found in the Alps, for example Miage glacier, Venerocolo glacier and Solda Occidentale glacier (Fig. 4).

Figure 4 Examples of debris-covered glaciers in the Alps. From the top to the bottom: Miage glacier (Mont Blanc Massif, Valle d'Aosta, Italy); Venerocolo glacier (Adamello group, Lombardia, Italy); Solda Occidentale glacier (Ortles-Cevedale group, Südtirol, Italy).

Due to the importance of the supraglacial debris cover in influencing glacier ablation, it is important to map not only the extension of the debris cover, but also its thickness. While mapping the extension of the supraglacial debris cover is a task that can be done using different remote sensing data, from satellite images, to high-resolution orthophoto or UAV images, mapping the debris thickness on glaciers remains an important issue.

Another open issue in the research concerning supraglacial debris is related to the sparse debris. We talk about sparse debris (or dirty ice) when debris does not form a complete cover on the glacier surface. While the evolution and the effects of the complete debris cover on glaciers have been widely studied, the evolution and the effects of the sparse debris have been poorly investigated. Only a recent work by Fyffe et al. (2020) studied the influence of sparse debris on the ablation rates, finding that at moderate percentage of debris cover(c. 30–80%), ablation has similar values and is enhanced (+3.7%) compared to clean ice (with 0-15% of debris), while when the debris becomes complete, there is a very abrupt decrease in ablation (by 61.6% compared to a partial debris cover).

1.3. Contribution to scientific papers

The manuscripts that compose this thesis were published or are intended to be published on scientific journals:

1) Tarca, G., Guglielmin, M., Convey, P., Worland, M. R., & Cannone, N. (2022). Small-scale spatial–temporal variability in snow cover and relationships with vegetation and climate in maritime Antarctica. *Catena*, 208, 105739.

2) Tarca, G., & Guglielmin, M. (2022). Using ground-based thermography to analyse surface temperature distribution and estimate debris thickness on Gran Zebrù glacier (Ortles-Cevedale, Italy). *Cold Regions Science and Technology*, 103487.

3) Tarca, G., & Guglielmin, M. Evolution of the sparse debris cover during the ablation season at two small Alpine glaciers (Gran Zebrù and Sforzellina, Ortles-Cevedale group). Submitted to the journal Geomorphology.

4) Tarca, G., Hoelzle, M., & Guglielmin, M. Using PlanetScope images to investigate the evolution of small glaciers in the Alps. Submitted to the journal Remote Sensing of Environment.

2. Small-scale spatial–temporal variability in snow cover and relationships with vegetation and climate in maritime Antarctica

Catena 208 (2022) 105739

Contents lists available at ScienceDirect

Catena

journal homepage: www.elsevier.com/locate/catena

Small-scale spatial–temporal variability in snow cover and relationships with vegetation and climate in maritime Antarctica

G. Tarca [a], M. Guglielmin [a,*], P. Convey [b,c], M.R. Worland [b], N. Cannone [d]

[a] Center for Climate Change Research, Department of Theoretical and Applied Sciences, Insubria University, Via J.H., Dunant, 3, 21100 Varese, Italy
[b] British Antarctic Survey, NERC, High Cross, Madingley Road, Cambridge CB3 0ET, United Kingdom
[c] Department of Zoology, University of Johannesburg, Auckland Park 2006, South Africa
[d] Dept. Science and High Technology, Insubria University, Via Valleggio, 11, 22100 Como, Italy

ARTICLE INFO

Keywords:
Snow
Vegetation
Antarctica
Climate change
ENSO

ABSTRACT

Snow cover changes can have important effects on ecosystems, especially where spatial variability in cover is high, influencing the biogeochemical conditions of the underlying soil as well as the vegetation. In this study, snow thickness and areal distribution were monitored using a time lapse camera over a grid of 15 × 20 m between 2009 and 2017 at Signy Island (60°S, South Orkney Islands, maritime Antarctica). The data obtained confirmed high spatial and temporal variability in snow cover. Over the study period, the mean annual snow depth ranged between 5.6 cm (2017) and 11.1 cm (2012) while the maximum of the mean daily snow depth across the entire grid ranged between 17.1 cm (2017) and 50.1 cm (2015). No temporal trend was apparent but there was a strong correlation with mean annual air temperature, suggesting that possible future warming could decrease snow depth in the area. A negative correlation was identified between the winter Southern Oscillation Index (SOI) and mean annual snow depth, indicating an influence of El Niño–Southern Oscillation (ENSO) on snow cover in this part of Antarctica. There was considerable small-scale spatial variability in snow depth at each individual stake, with mean values between 3.9 and 25.3 cm and maximum values between 27 and 85 cm. Snow depth variability was influenced primarily by microtopography and wind direction, but also by the land cover type (vegetation). Our data highlight that spatial monitoring of snow accumulation is required at small physical scale to predict future effects of climatic changes on these sensitive maritime Antarctic terrestrial ecosystems.

1. Introduction

Snow cover is an important component of the global climate system, as it modifies energy and moisture fluxes between the ground surface and the atmosphere, and acts as a water store in hydrological systems (Brown and Robinson, 2005). Snow characteristics, such as its high albedo and emissivity (that tend to cool the snow surface), high absorptivity (that in contrast tends to warm the surface), and low thermal conductivity make it an effective insulator of the ground and terrestrial ecosystems below (Zhang, 2005).

The spatial and temporal distribution of snow cover influences the biogeochemical conditions (moisture, temperature, chemistry) in the underlying soil, which in turn can determine the distribution of soil invertebrates and microbiota (Gooseff et al., 2003). Snow also affects vegetation (Callaghan et al., 2011) by influencing the temperature regime through its insulation qualities and also the availability of water and light (Kappen et al., 1995; Winkler et al., 2000). It thereby controls species distributions, growing season length and phenology (Borner et al., 2008). In Antarctica snow has both positive and negative effects on vegetation (Green et al., 2011). In continental Antarctica, lichens and mosses remain inactive at sub-zero temperatures even when the external air and surrounding exposed substrates warm due to the insulating effect of snow, prolonging the duration of winter conditions (Pannewitz et al., 2003). In contrast, snow cover in the maritime Antarctic can protect the underlying vegetation and soils from temperature extremes during winter, and heterogeneity in the depth of snow leads to local variations in minimum temperatures (Davey et al., 1992; Convey et al., 2018). Transmission of light through relatively thin snow cover can warm the ground below, leading to melting at the base of the snowpack and the formation of what are effectively miniature greenhouses within which soil microbial communities can become active (Cockell et al., 2002). Snow cover also has a significant influence on permafrost distribution,

* Corresponding author.
E-mail address: mauro.guglielmin@uninsubria.it (M. Guglielmin).

https://doi.org/10.1016/j.catena.2021.105739
Received 21 March 2021; Received in revised form 14 September 2021; Accepted 17 September 2021
Available online 27 September 2021

temperatures and thickness (Zhang, 2005). A further important feature of snow cover lies in its spatial variability at the local scale, as accumulation, redistribution and ablation processes are affected by features such as microclimate, topography, and characteristics of vegetation (Neumann et al., 2006).

A limited number of studies have examined the spatial and temporal variability of snow cover in Antarctica. Of these, most have studied snow accumulation on Antarctic sea ice (e.g. Massom et al., 1998; Worby et al., 2008; Pfaffhuber et al., 2017; Arndt and Paul, 2018) or on glaciers and ice sheets (e.g. Richardson et al., 1997; Braaten, 2000; Frezzotti et al., 2005; Arthern et al., 2006; Rotschky et al., 2007; Banta et al., 2008; Genthon et al., 2016; Bertler et al., 2018), while only a few have focused on snow variability in terrestrial habitats (e.g. Guglielmin et al., 2014a,b).

In the maritime Antarctic, the temporal pattern of snow cover evolution was studied during the period 2009–2014 by De Pablo et al. (2017) while Fassnacht et al. (2013) mapped snow cover and depth focusing on spatial distribution but not considering temporal variability. Both studies took place on Byers Peninsula, Livingston Island, in the South Shetland Islands. Guglielmin et al. (2014a,b) investigated spatial and temporal variability of snow depth at Rothera Point, Adelaide Island, documenting large variability both spatially and temporarily, but based on a limited dataset derived from a small number of stakes (5) and a shorter study period of only 3 years.

Hrbáček et al. (2016) recorded snow depth using an ultrasonic depth sensor on the Ulu Peninsula (James Ross Island, north-eastern Antarctic Peninsula) for the period from 1 March 2011 to 11 June 2012 while, more recently, at the same site Hrbáček et al. (2021) analysed the temporal variability of snow depth over a shorter period (from 10 January to 25 January 2018). Although the latter study assessed the spatial distribution of snow cover and snow depth using different promising methods including UAV, GPR scanning and mechanical probing, these measurements took place on only a single day. Finally, at Signy Island the first data from a monitoring program started in the 2009 (February to October 2009) were reported by Guglielmin et al. (2012).

The influence of the snow cover thickness on the underlying ground temperature and on vegetation is related to its permanence commonly referred to threshold depths such as 5, 10 and 30 cm. Snow cover <5 cm significantly decreases the ground surface temperature both through the albedo effect and the greater sensible heat gradient (e.g. Guglielmin et al., 2014a,b; Keller and Gubler, 1993), while a depth of 10 cm can reduce visible light transmission to about 5% of the incident irradiance and transmission in the near-infrared to less than 1% (Perovich, 2007). Finally, 30 cm snow depth can effectively decouple ground surface temperature from air temperature (Schneider et al., 2012; Convey et al., 2015, 2018).

Whether snow cover variability, which is crucial for the underlying ecosystems, is related only to the variability of local surface characteristics (such as topography, vegetation or ground characteristics) (i.e. Walker et al., 2001), to local variability in precipitation patterns or wind redistribution (which can influence accumulation as well as melting) (Mott et al., 2018), or to the regional climate continues to be debated. In Maritime Antarctica, it is known that air temperature and precipitation are influenced by regional circulation features such as the El Niño–Southern Oscillation (ENSO) and the Southern Annular Mode (SAM) (Clem et al., 2016; van Wessem et al., 2017). However, the relationship between snow cover and such features are not well known.

More detailed study of snow spatial and temporal variability is required to better understand the influence of snow cover and its heterogeneity on underlying ecosystems, soil processes and permafrost. The long-term monitoring dataset obtained over the period 2009–2017 on the spatial and temporal variability of snow cover and depth at Signy Island, South Orkney Islands, allows us to hypothesize that: (a) air warming decreased snow depth in this area, (b) temporal variations of snow cover are influenced more by ENSO than by SAM, (c) the spatial variability of snow is mainly related to microtopography and wind direction, and d) land cover type (vegetation) follows the patterns of snow cover presence and persistence.

2. Study area

The study site is located on Signy Island (60°43′S, 45°38′W; South Orkney Islands, maritime Antarctic) (Fig. 1). Signy Island has a surface area of about 19 km^2, reaching a maximum height of 288 m a.s.l., with about half of its area currently covered by a permanent small ice cap (Guglielmin et al., 2008). Signy has a cold oceanic climate, with mean annual air temperatures of around −3.5 °C and mean monthly air temperatures above 0 °C for at least one (and up to three) months each summer (Guglielmin et al., 2008). A characteristic of the island's climate is the high cloudiness of at least of 6–7 oktas year-round (Guglielmin et al., 2008). The only long data series for annual precipitation in the South Orkney Islands is located at Orcadas Station (Laurie Island, c. 50 km from Signy Island), where an increase in precipitation has been recorded since 1960, that has accelerated since 1993 (Royles et al., 2012; Cannone et al., 2006). Between 1960 and 2009 strong air warming was recorded, especially during the summer (1.2 °C, Cannone et al., 2006). However, Oliva et al. (2017), comparing the decades 1996–2005 and 2006–2015, reported a cooling of 0.2 °C in the Orcadas data.

The island's bedrock is characterised by metamorphic rock outcrops (Smith, 2007) while soils are predominantly Gelisols with a prevalence of Psammoturbels and Haplorthels (Guglielmin et al., 2008) due to presence of continuous permafrost with quite variable active layer thickness (0.4 to >3 m; Guglielmin et al., 2008, 2012). The vegetation of Signy Island is rich and diverse, and representative of the maritime Antarctic. It comprises both the Antarctic herb tundra formation, where the two native vascular plants *Deschampsia antarctica* Desv. and *Colobanthus quitensis* Bartl. occur, as well as the more common Antarctic nonvascular cryptogam tundra formation (Gimingham and Smith, 1970; Smith, 1972).

3. Methods

3.1. Data

Climatic data for the period 2009–2017 were recorded by an automatic weather station (AWS) CR23X (Campbell Scientific, UK) located within the snow grid. The snow grid is located on the summit of the Backslope (unofficial name) at 110 m a.s.l. The Backslope is a gentle north-oriented slope rising behind Signy Research Station from the shore of Factory Cove. The AWS measured air temperature, wind speed, wind direction and incoming shortwave radiation using a net radiometer (CNR1, Kipp and Zonen). Wind data are available only for the period 2009–2011 and 2013, due to malfunctioning of the sensors. Temperature data are not available for some months in 2014. Incoming shortwave radiation measurement included diffuse and direct incoming radiation in the spectral range 305–2800 nm but, due to large data gaps from technical failure of sensor, data were available from the complete years 2009–2012 and 2016.

To assess the relationship between snow cover/depth and precipitation we used data from the Orcadas AWS (Orcadas Station, Laurie Island, c. 50 km east of Signy Island) that provides the only precipitation data available from the South Orkney Islands.

In addition, monthly Southern Oscillation Index (SOI) (that measures El Niño–Southern Oscillation (ENSO) variability), and monthly mean Antarctic Oscillation index (AAO) (that corresponds to the Southern Annular Mode (SAM)), were obtained from the NOAA Climate Prediction Center (https://www.cpc.ncep.noaa.gov/).

An automatic time-lapse digital snow camera (PENTAX EI-2000, 2 megapixels) was installed in February 2009 by one of the authors (M.R. W.). The camera recorded 2 images per day of a matrix of 19 banded snow stakes, that formed an irregular grid of 15 × 20 m (Fig. 1). The

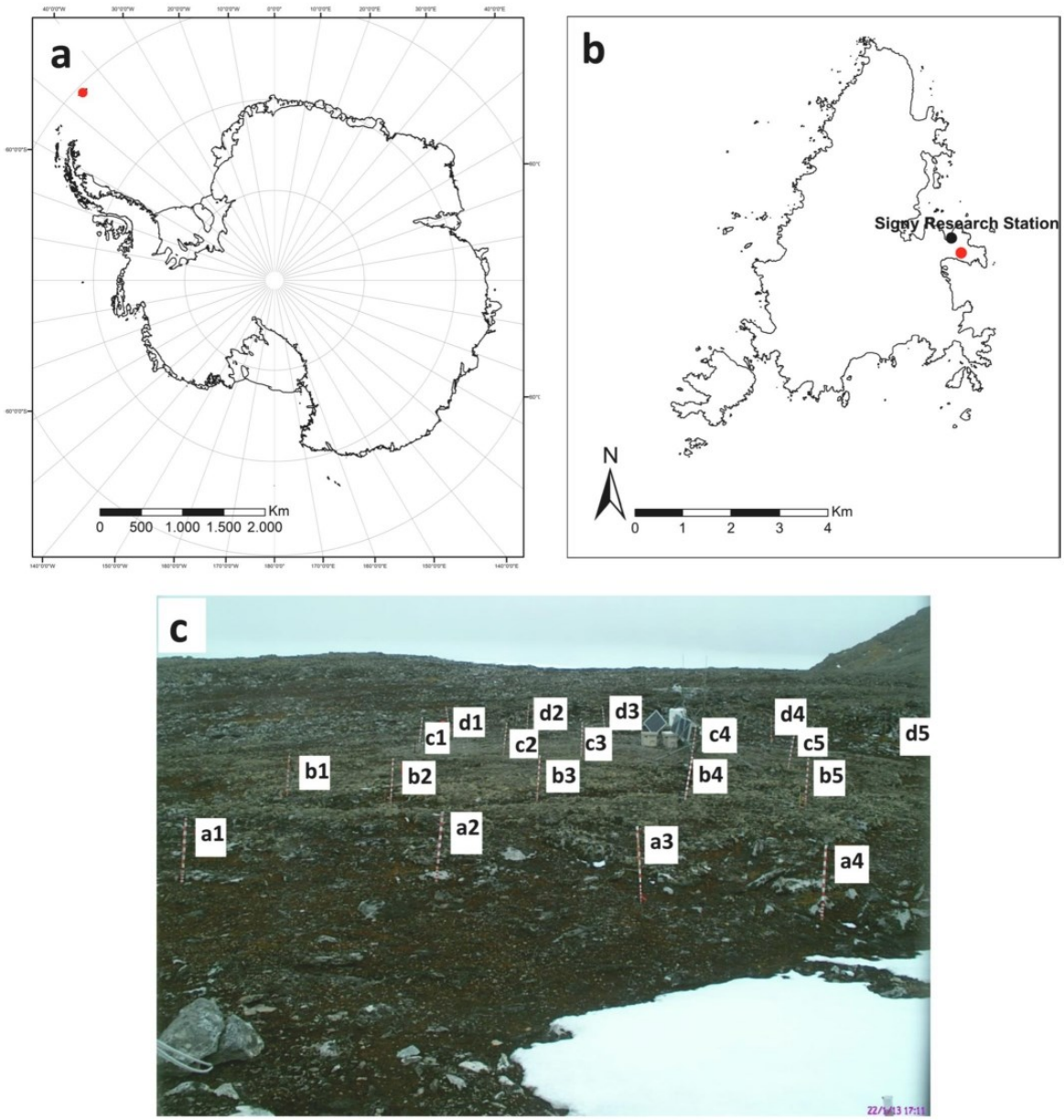

Fig. 1. (a) Location of Signy Island; (b) of the study site (red point) and Signy Research Station (black point); (c) example of an image of the snow grid at Signy Island taken on 22 January 2013. (For interpretation of the references to colour in this figure legend, the reader is referred to the web version of this article.)

stakes were marked with 10 narrow (2 cm wide) alternate white and red bands over the lower 20 cm above the ground level and with 5 cm wide bands above these to a height of 85 cm (Guglielmin et al., 2012). Snow depth at each stake was obtained by visually counting the bands. In case of a snow height falling between two bands, we estimated an intermediate value. For each day the sharper picture was chosen (two pictures were taken at a 30 min interval) as all the pictures were not readable for different reasons (for instance due to snow or drops of water on the lens or the occurrence of fog) (Fig. S1, Supplementary Materials). When the camera resolution was not able to resolve the graduation of the stakes, as in the case of the most distant stakes or with low atmospheric visibility, snow depth was calculated as the difference between the length of the stake emerging from the snow and the total length of the stake, measuring the number of pixels using ArcGIS 10.4. Examples of snow depth measurements in three different conditions are shown in Fig. S2 (Supplementary Materials). In addition, if the stake was inclined, a trigonometric correction was applied to estimate the true height. The accuracy of the directly observed snow depth measurements was 2 cm and, in case of pixel measurement, the maximum pixel size was 1.8 cm. Snow depth data were obtained for each stake, except for stake c4 that was often covered by stake b4 and was therefore excluded from the results. Snow depth measurements were carried out for the period from

February 2009 to December 2017, excluding November 2009 to March 2010. For each day the mean, maximum and minimum depth values for the entire grid were computed. The snow season was calculated as the period when at least five days of snow cover and no more than five snow-free days occurred.

3.2. Data analyses

To document topographic and land cover characteristics of the monitored area, we used an orthophoto and a digital elevation model (DEM) generated from a drone flight performed on 8 January 2018 (just after the end of the study period of the snow monitoring) using a DJI Inspire 2 mounting a DJI Zenmuse X5S 20 MP camera. The DEM had a resolution of 0.048 m and was used to derive the following topographic parameters: elevation, slope, aspect, topographic position index (TPI). These parameters were calculated using ArcGIS 10.4. The TPI provides information on the relative position of a cell in relation to the surrounding terrain at a specific spatial scale (Revuelto et al., 2014), measuring the difference between the elevation at the central point (z_0) and the average elevation ($\bar{z}$) around it within a predetermined radius (R) (De Reu et al., 2013):

$$TPI = z_0 - \bar{z} \quad (1)$$

$$\bar{z} = \frac{1}{n_R}\sum_{i \in R} z_i \quad (2)$$

Positive TPI values indicate that the central point is located higher than its average surroundings, while negative values indicate a position lower than the average. The TPI was calculated for 0.05, 0.1, 0.15, 0.20, 0.3, 1.0 and 1.5 m radial distances for each pixel. We present only TPI at 1 m as an example, as it is meaningful because it covers the same area as the vegetation surveys. For each stake in the grid, we assessed elevation, slope and aspect (all calculated as the average in a 0.3 m buffer), and TPI at 0.05, 0.1, 0.15, 0.20, 0.3, 1.0 and 1.5 m.

The land cover and vegetation of the grid were mapped using the available high resolution orthophoto (0.048 m). We performed a supervised maximum likelihood classification using ArcGIS 10.4 to map six different classes in the image: (1) bare soil; (2) rocks; (3) macrolichens (*Usnea* spp. *Umbilicaria* spp., *Himantormia lugubris*); (4) xeric mosses (*Andreaea* spp.); (5) hygric mosses (*Sanionia uncinata*); (6) instruments (e.g., AWS and snow cam). In order to train the classifier, we selected four training samples (3940 pixels) from the orthophoto for bare ground, eight (1180 pixels) for rocks, three (2785 pixels) for macrolichens, eight (1038 pixels) for xeric mosses, one (1115 pixels) for hygric mosses and four (1203 pixels) for instruments (as shown in Fig. S3). The accuracy of this classification was successively verified through 100 points randomly distributed on the orthophoto. Additionally, to better describe the six classes of coverage of the supervised map obtained radiometrically, a physiognomic survey of the vegetation in field plots of 1 × 1 m at each node of the grid was carried out to provide the total vegetation cover (%), the cover (%) of mosses and macrolichens for each node of the grid, allowing provision of their associated ecological information.

To study the spatial variability of snow depth we calculated a normalized index of variability (*Iv*), as described by Hinkel and Nelson (2003) (in %), given by:

$$Iv = \left(\frac{SDi - SDavg}{SDavg}\right) * 100 \quad (3)$$

where *SDi* is the snow depth at a stake in a selected year and *SDavg* is the average snow depth for the entire grid. Positive index values indicate that the stakes have a snow depth greater than the average and negative values indicate lower than average depth. The interannual node variability (INV, %) was also calculated to determine consistency during the period of record. INV values of 0–19% describe low variability, 20–29% moderate variability and >30% high variability (Smith et al., 2009).

Forward stepwise multiple regressions were used to analyse the influence of topography on the snow depth spatial distribution and identify the topographic variables that best explained the snow distribution in this area, and linear regressions to test the effect of climatic factors (air temperature at 160 cm, wind speed, incoming shortwave radiation and annual precipitation at Orcadas) on snow depth and its temporal variability.

We also analysed the temporal distribution of the snow cover with respect to the major snow cover thickness thresholds (5, 10 and 30 cm). We analysed the relationship between the permanence of different snow depth classes (0 cm; ≤5 cm; 5–10 cm; 10–30 cm; >30 cm) and vegetation (same classes as used for the supervised classification) using Pearson correlation analyses. These analyses were carried out using the software Statsoft 10.0©.

4. Results

4.1. Climate

In the period 2009–2017 the mean annual air temperature ranged between −4.2 °C (2012 and 2015) and −2.7 °C (2010), with an overall mean of −3.5 °C and no trend apparent through the period (Table 1). Mean seasonal air temperatures also did not show any trend over the study period. The warmest month was variable but most commonly January and February, ranging between −0.5 °C (2013) and + 1.9 °C (2009), while the coldest month (mainly August) ranged between −14.2 (2011) and −7.2 °C (2010) (Table 1). Daily mean temperatures reached a maximum of + 10.0 °C in 2013, and a minimum of −27.7 °C in 2012 (Table 1). Wind speed close to the ground (60 cm above the surface) ranged between mean annual values of 3.2 m s^{-1} (2013) and 4.9 m s^{-1} (2009), with an overall mean of 4.1 m s^{-1} (Table 1). The daily maximum wind speed was 15.6 m s^{-1}, recorded in 2013. Prevalent wind direction over the period was NNW, but wind direction showed some intra-annual and inter-annual variability (Fig. 2). Mean annual incoming shortwave radiation ranged from 77 to 89 W m^{-2}, without any temporal trend (Table 1). Annual precipitation registered at Orcadas was between 430 mm (2017) and 1404 mm (2010), with an average of 1039 mm per year between 2009 and 2017.

The mean annual AAO ranged between −0.193 (2009) and 0.786 (2010), with negative values in 2009 and 2011, and positive values in the other years. The mean annual SOI ranged between −0.792 (2015) and 1.400 (2011), with negative values in 2014, 2015 and 2016 and positive values in the other years (Table 1).

4.2. Temporal and spatial variability of snow cover

Daily snow depth measured at the Signy snow grid (Fig. 3) reached a maximum in 2015 (50 cm), while during the other years the maximum snow depth was 40 cm. Frequent snowfall occurred throughout the year, including the summer, and a continuous snow-free season was never observed during the study. Due to the extreme conditions some data gaps occurred after the installation of the snow lapse-rate camera, although the main gap was during the first summer (November 2009 to March 2010) and, subsequently, only September and November 2013 did not have enough data. There were occasional missing days in the time series, due to malfunctioning of the camera or the impossibility of seeing the stakes in the images (examples in Fig. S1, Supplementary Material).

Across the entire grid snow cover showed inter-annual variability ranging between 5.6 cm (2017) and 11.1 cm (2012) (Table 1). Annual means did not show a temporal trend in the study period while the maximum snow depth on the entire grid ranged between 17.1 (2017) and 50.1 cm (2015) (Table 1). The snow season started between 14 March (2014) and 22 April (2013). The end of the snow season showed higher inter-annual variability, occurring between 5 November (2011)

Table 1
Main climatic parameters at the Signy snow grid, climatic indices and snow data for the 2009–2017 period. Annual values of mean air temperature (MAAT), maximum monthly T, minimum monthly T, maximum daily T, minimum daily T, mean shortwave incoming radiation (SWIN), mean wind speed, precipitation at Orcadas, mean Antarctic Oscillation index (AAO), mean Southern Oscillation Index (SOI), mean snow depth and maximum snow (NA: no data available).

	2009	2010	2011	2012	2013	2014	2015	2016	2017
MAAT (°C)	−3.5	−2.7	−3.4	−4.2	−3.6	NA	−4.2	−3.7	−3
Max monthly T (°C)	1.9(JAN)	1.1(NOV)	1.8(FEB)	0.4(FEB)	−0.5(OCT)	NA	−0.1(DEC)	0.4(FEB)	1.2(JAN)
Min monthly T (°C)	−12.0(AUG)	−7.2(AUG)	−14.2(AUG)	−9.8(JUL)	−8.1(JUN)	−12.5(AUG)	−9.2(SEP)	−11.8(AUG)	−7.3(JUN)
Max daily T (°C)	6.6	5.4	8.9	7.7	10.1	NA	4.3	3.1	3.3
Min daily T (°C)	−25.8	−22	−26.6	−27.7	−25.3	NA	−21.3	−20.1	−21.2
SWIN (Wm^{-2})	81	80	81	89	NA	NA	NA	77	NA
Wind speed (ms^{-1})	4.6	4.9	3.8	NA	3.2	NA	NA	NA	NA
Precipitation (mm)	889	1404	1238	666	1335	1178	1321	890	430
AAO	−0.193	0.786	−0.055	0.133	0.032	0.079	0.714	0.567	0.446
SOI	0.245	0.908	1.400	0.133	0.450	−0.133	−0.792	−0.192	0.358
Mean snow depth (cm)	NA	NA	7.2	11.1	NA	8.3	10.8	6.6	5.6
Max snow depth (cm)	35.2	40.2	28.9	26.9	37.4	27.1	50.1	39.4	17.1

and 21 January (2013). Therefore, snow duration ranged between 198 and 291 days (Table 2). The snow-free season was never continuous, being interrupted by 7 to 15 snowfall events each year (Fig. 3).

Snow depth showed large spatial variability, with mean snow depth for the entire study period being between 3.9 (stake b5) and 25.3 cm (stake d4) (Table 3, Fig. 4). Values greater than 20 cm were recorded at only two stakes (d4 and d5), while most stakes (11 out of 18) showed values lower than 10 cm. The mean snow depth for the entire grid was 10.0 cm, while the measured maximum depth varied between 27 and 85 cm (Table 3). Row "d" of the grid exhibited the highest values, although the location of the AWS close to stakes d3 and d4 may have affected snow distribution at these points (Fig. 5b).

The percentage of snow-free days in the entire study period varied between 26% (stakes a4, d5) and 54% (stake c1). The days with a snow depth < 5 cm ranged between 4% (d5) and 21% (c5), depth 5–10 cm ranged between 5% (d4) and 37% (b4), depth 10–30 cm ranged between 8% (b5) and 46% (b2), and depth > 30 cm ranged from 0% (b4, b5, c3, c5) to 41% (d4) (Fig. 6). The normalized index of variability (Iv) confirmed the high spatial variability of snow depth in the study area, with values ranging from −61% to 153% (Table 3). The inter-annual node variability was also high at most of the stakes over the study period (Table 3), with a mean INV for the entire grid of 74%, indicating that the spatial variability was not consistent between years.

4.3. Topography

Elevation in the grid ranged between 109.1 and 112.9 m a.s.l., with a mean of 110.4 m a.s.l. (Fig. 7) Slope ranged between 0 and 80° (discounting the areas occupied by the instruments), but the mean surface slope was almost flat (6.7°). The pixels included all aspects, from flat to 360°, with a mean southward aspect (179°). Pixels with a north/north-east/north-west aspect were less represented than those with a south/south-east/south-west aspect, covering respectively 17 and 52% of the grid area. Fig. 7 shows a small prevalence across the grid area of pixels with negative values (53%) over those with positive (47%), indicating that depressions were slightly more widespread than reliefs.

The stakes were located at elevations between 110.0 and 110.5 m a.s.l. (Table 4). Slopes around stakes ranged between 2 and 26°, with a mean of 5°, indicating that most of the stakes were located in an almost flat area, except stake d5 (26°) (Table 4). Aspect ranged between 93 (east) and 282 (west) degrees, with a mean of 187 (south) degrees (Table 4). TPI at 1.0 m was negative at 12 stakes and positive at 6 stakes, indicating that most of the stakes were located lower than their surroundings in depressed areas. The mean TPI was −0.0058, ranging between −0.0661 and 0.008 (Table 4).

4.4. Land cover classification

The supervised classification was performed on a total area of about 849 m^2 (35.7 × 23.8 m) with an overall accuracy of 82%, visually evaluated at 100 random points (the confusion matrix of the classification is presented in Table 5). The prevalent surface was classified as macrolichens, covering more than 34% of the area, with xeric mosses and bare ground contributing almost the same area (22.2% and 21.7% respectively) (Fig. 8). Rock outcrops contributed >19%, while hygric mosses contributed only 2.5%, almost completely confined to a single patch.

4.5. Role of topography and climate in influencing spatial and temporal snow variability

The forward stepwise multiple regression between snow depth at each stake (excluding stakes d3 and d4, potentially affected by the presence of the AWS) and elevation, slope and aspect indicated that mean snow depth was significantly influenced by slope ($\beta = 0.71$, $p = 0.002$). The multiple regression with the different TPI showed that snow depth at each stake was significantly influenced by TPI at 1.0 m ($\beta = -0.73$, $p = 0.001$). The negative correlation with the TPI at 1.0 m indicates that snow tended to accumulate in depressions as would be expected with drifting snow (e.g., Fig. 5a, b). This suggests that snow depth was locally influenced by the microtopography calculated in a radius of 1 m.

The high spatial variability of snow cover at small scale was clearly related to microtopography, which influenced the distribution of accumulation and the post-depositional processes, in particular wind redistribution. Snow tended to accumulate where the TPI was negative and on the leeward side of blocks (e.g., Fig. 5). For example, excluding d3 and d4, having mean snow depths greater than the mean of the entire grid due to the accumulation of snow caused by the presence of the AWS, d5 featured the highest mean snow depth (22.7 cm) and the most negative TPI (Table 3), being located at the base of a rock outcrop on the leeward side.

Mean annual air temperature was the only factor that significantly influenced mean annual snow depth, and there was a significant strong negative correlation between mean annual snow depth and mean annual air temperature ($r = -0.92$; $p = 0.029$) (Fig. 9). The correlation between air temperature and snow depth is confirmed also by monthly data, with a significant correlation between the mean monthly air temperature and the mean monthly snow depth ($r = -0.67$; $p < 0.001$) (Fig. 9). It is notable that months with positive mean monthly air temperatures were always characterized by mean snow depths lower than 5 cm (showing a maximum of 2.8 cm). We also found a strong negative correlation between mean annual air temperature and the snow cover duration in the different years ($r = -0.92$; $p = 0.027$). There was no statistically significant correlation between the mean annual snow depth and annual precipitation registered at Orcadas ($r = 0.33$; $p = 0.518$).

Analysing the relationships between the snow cover and the regional climate indices AAO and SOI at monthly, seasonal and annual scales, we

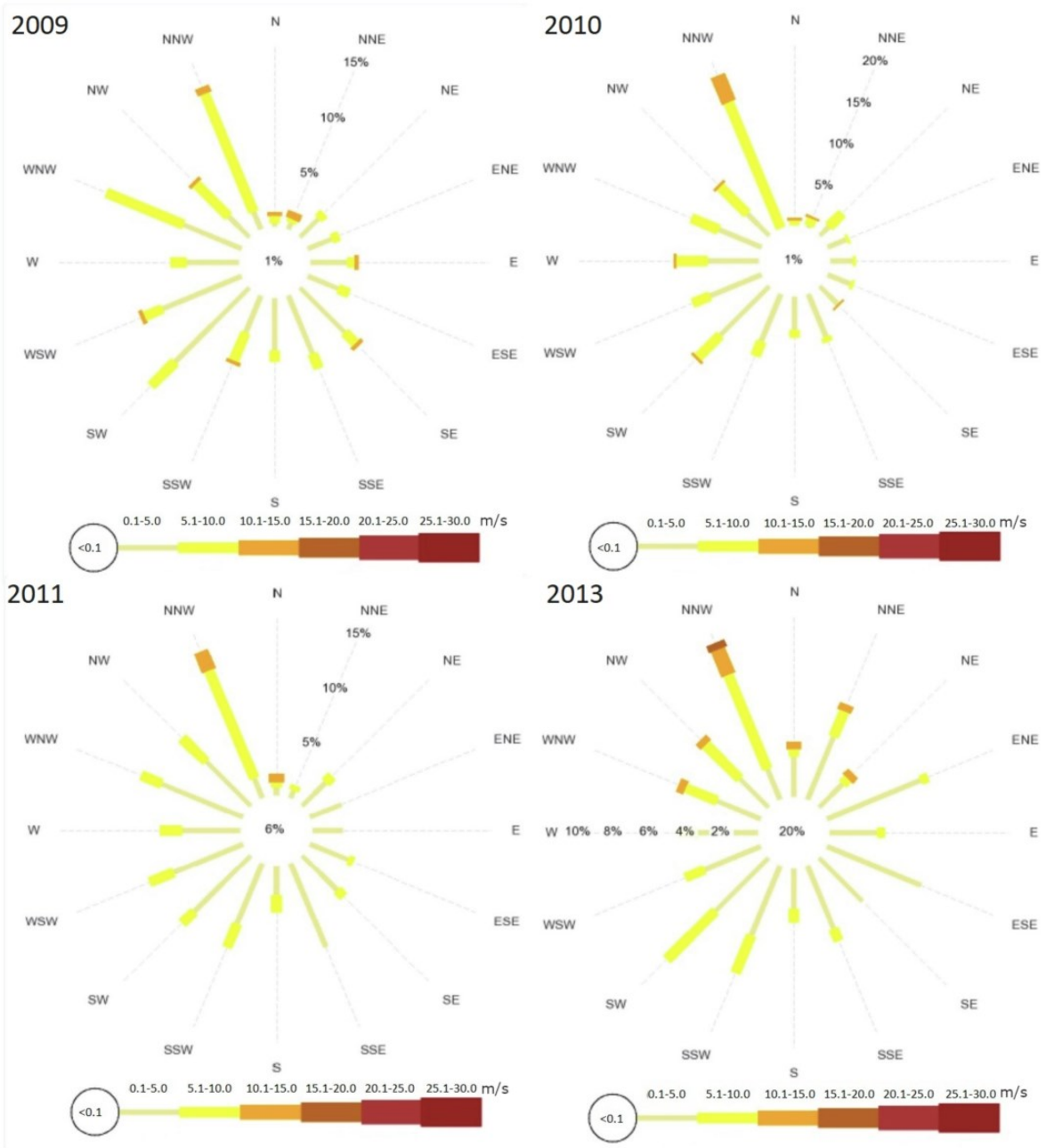

Fig. 2. Wind rose plots, representing wind speed and direction at the Signy snow grid, related to the years 2009, 2010, 2011 and 2013. Despite a certain variability, NNW winds are always the dominant.

identified only a negative correlation between winter SOI and mean annual snow depth over the study period which approached statistical significance ($r = -0.80$, $p = 0.056$). All other relationships were not statistically significant.

4.6. Relationship with vegetation

Within the snow grid, six snow stakes were positioned on bare ground/rocks, four on xeric moss, eight on macrolichens and one on hygric moss. There was very good correspondence between field vegetation data and the supervised classification of vegetation for the plots with high vegetation cover dominated by xeric mosses (100%) and macrolichens (87.5%). However, correspondence between field data and the supervised classification was poor for barren ground/rocks (25%) and was not evaluated for hygric mosses as only one plot was available. TPI showed a good relationship with distribution of the moss-

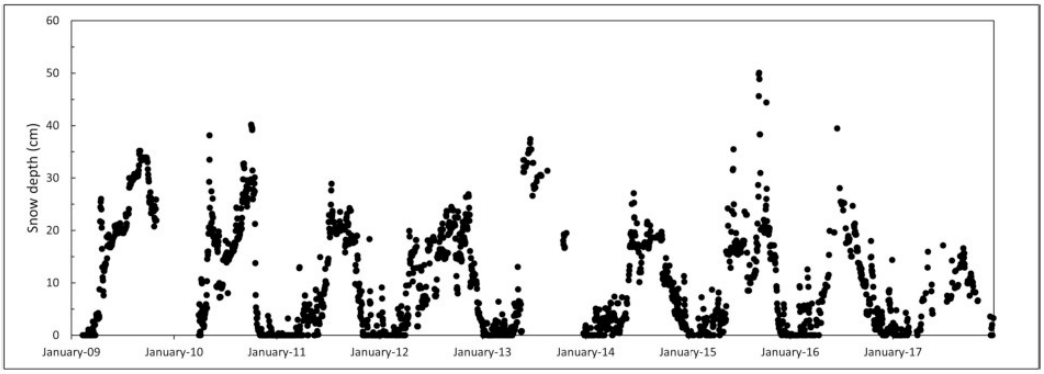

Fig. 3. Temporal evolution of daily snow depth (cm) at the Signy snow grid from 2009 to 2017. Each point represents the mean value of the snow depths measured at the 18 stakes daily.

Table 2
Snow timing at the Signy snow grid in the study period. Snow cover season start, snow cover season end, snow cover duration (days) and number of snow events occurring during the snow-free season. NA: no data available. In this case we also included 2013 because the data gap is distributed in a way that permitted the definition of the start and the end of the snow season as well as the exact number of snow events in the snow-free season. Two snow-free seasons in which occasional missing data do not permit the counting of the exact number of snow events but only their minimum number are marked in **bold**.

Year	Snow cover start	Snow cover end	Duration	Snow events
2010	NA	10/11/2010	NA	9
2011	07/04/2011	05/11/2011	212	9
2012	05/04/2012	21/01/2013	291	12
2013	22/04/2013	06/11/2013	198	15
2014	14/03/2014	28/12/2014	289	**>10**
2015	04/04/2015	30/12/2015	270	7
2016	09/04/2016	06/12/2016	241	**>7**

Table 3
Summary of snow spatial variability at the 18 stakes of the Signy snow grid in the period between 2009 and 2017. For each stake mean snow depth (cm), standard deviation (cm), maximum snow depth (cm), normalized index of variability (Iv) (%), interannual node variability (INV) (%) are presented. For spatial relationships see Fig. 4.

Stake	Elevation (m)	Slope (degrees)	Aspect (degrees)	TPI 1.0 m
a1	110.33	2	245	0.0035
a2	110.26	3	165	−0.0030
a3	110.16	4	197	−0.0062
a4	110.02	4	123	−0.0154
b1	110.36	4	115	−0.0087
b2	110.35	7	93	−0.0008
b3	110.38	4	93	0.0051
b4	110.35	2	201	0.0087
b5	110.27	3	216	0.0031
c1	110.50	3	201	−0.0036
c2	110.43	3	203	−0.0080
c3	110.41	2	223	−0.0020
c5	110.20	4	214	0.0006
d1	110.52	3	224	0.0040
d2	110.49	3	222	−0.0128
d3	110.44	3	185	−0.0023
d4	110.22	5	162	−0.0000
d5	110.09	26	282	−0.0661

dominated vegetation, with TPI values < 0 for 75% of xeric mosses and where the hygric mosses occurred.

There was a gradient of mean snow depth across the six classes of the supervised classification, with the highest values for hygric moss (22.7 cm), followed by bare ground (12.9 ± 7.7 cm), and rocks (11.7 cm), and lower values characterizing xeric mosses (8.9 ± 3.6 cm) and macrolichens (6.7 ± 2.8 cm). A similar gradient characterized the relationship between the supervised vegetation classes and the maximum snow depth, consistent with the statistically significant correlation at plot scale between mean and maximum snow depth ($ß = +0.76$; $p < 0.001$).

Macrolichens had the lowest negative value of the index of variability (−34.5%), with this index also being negative for xeric mosses (−11.6%). The other classes generated positive values: rocks 17.0%, bare ground 47.0% and hygric moss 126.9%.

Mosses exhibited significant positive correlation with days of snow cover > 30 cm ($ß = +0.64$; $p = 0.004$) and negative correlation with snow-free days (snow = 0 cm) ($ß = -0.51$; $p = 0.032$). Macrolichens showed the highest correlation with days with snow cover between 5 and 10 cm ($ß = +0.59$; $p = 0.01$). All vegetated soils were characterized by a relatively high number of days without snow cover (31–38%). Among vegetated plots, there was a clear gradient of decreasing snow cover depth from hygric moss (associated with a longer period of deeper snow cover > 30 cm) (39.5%) to xeric mosses (associated with snow cover of 10–30 cm) (26%), while macrolichens were associated with snow cover of 5–10 cm. Barren ground and rock outcrop exhibited similar features to xeric mosses (Fig. 6).

5. Discussion

5.1. Air warming and decreased snow depth

Temporal and spatial variability of snow cover is very complex to explain because it can be related to both climatic conditions (air temperature and total precipitation), that control the total amount of snow precipitation, and to the surface characteristics that influence deposition, post-depositional processes and melting (e.g., Liston and Sturm, 1998).

Considering the primary relationships with climate, a significant and strong negative correlation was identified between mean annual snow depth and mean annual air temperature, consistent with the results previously reported by Guglielmin et al. (2012) at the same site. Mean monthly data also showed a negative correlation between air temperature and snow depth (Fig. 9b). This relationship suggests that, during colder years, there is an increase in mean annual snow depth resulting from an increase in the fraction of the total precipitation falling as snow independently from the total precipitation, as well as to a reduction of the melting rate. Although no data are available from Signy Island documenting total precipitation over the entire study period, using precipitation data from the Orcadas AWS in the same archipelago we found a weak and not statistically significant correlation between total

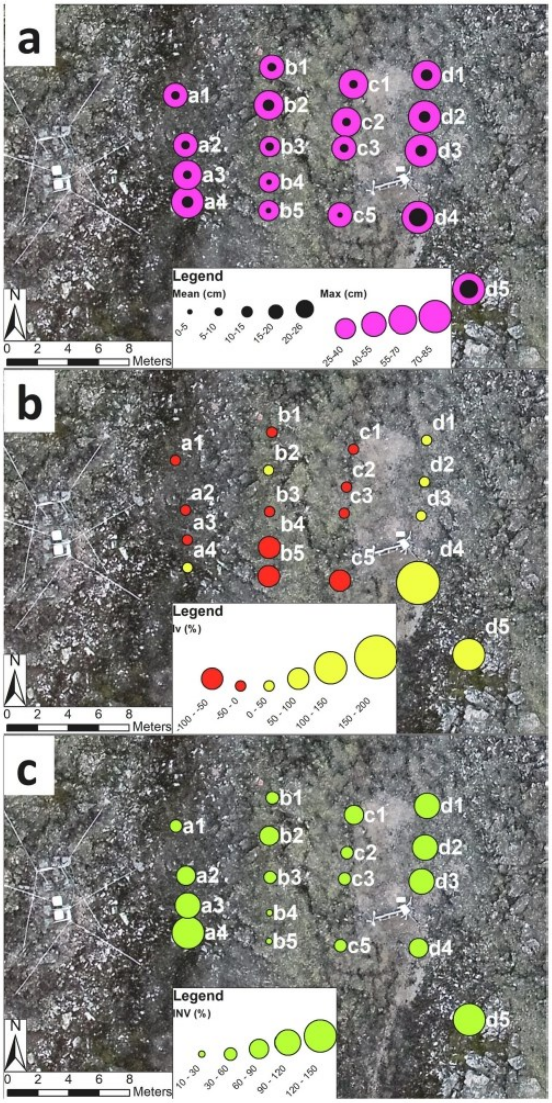

Fig. 4. Spatial snow variability at each snow stake in the Signy snow grid throughout the study period. (a) Mean (orange) and maximum (brown) snow depth (cm); (b) Normalized index of variability (Iv) (%) (negative values in red, positive values in yellow); (c) Interannual node variability (INV) (%). Values are reported in Table 4. (For interpretation of the references to colour in this figure legend, the reader is referred to the web version of this article.)

annual precipitation and mean annual snow depth. As an example, at Orcadas the year 2011 was characterized by a MAAT of −3.4 °C with 178 days with some precipitation and a total of 1238 mm while, while 2012 had a MAAT of −4.2 °C with 175 days with some precipitation but only 666 mm of total precipitation. In these two years the number of days with snow cover increased being, respectively, 90 (with total snow accumulation of 176 cm) and 109 (with 226 cm). These data are consistent with warmer air temperature being associated with greater total annual precipitation and more rainfall. Further, in 2011 five months registered positive mean temperatures (January, February, March, November, December), while in 2012 only two (January, February) did so. The more abundant snowfall coupled with warmer

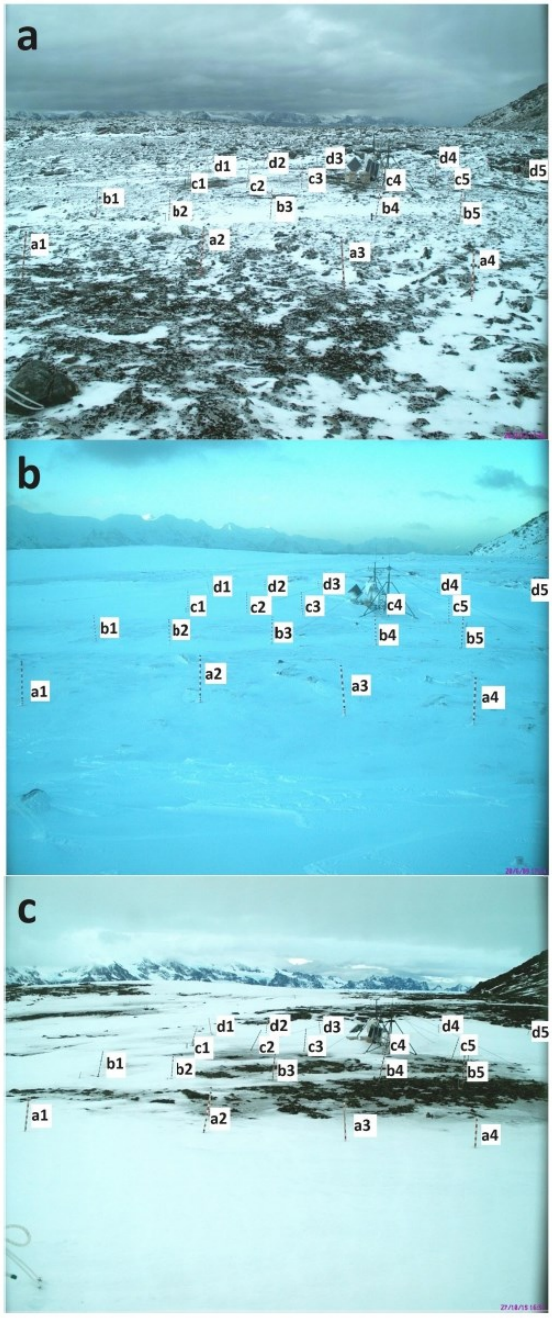

Fig. 5. Examples of snow distribution at the Signy snow grid: (a) Snow tends to accumulate in depressions. Image taken on 20/02/2013. (b) Snow redistribution by wind tends to lead to accumulation in the presence of obstacles, for example the stake d5 is completely covered by snow. The presence of the AWS also acts as an obstacle, leading to an accumulation of snow at stake d4. Image taken on 20/06/2009. (c) Snow located on Usnea lichen formation melts earlier than on other landcover types. Image taken on 27/10/2015.

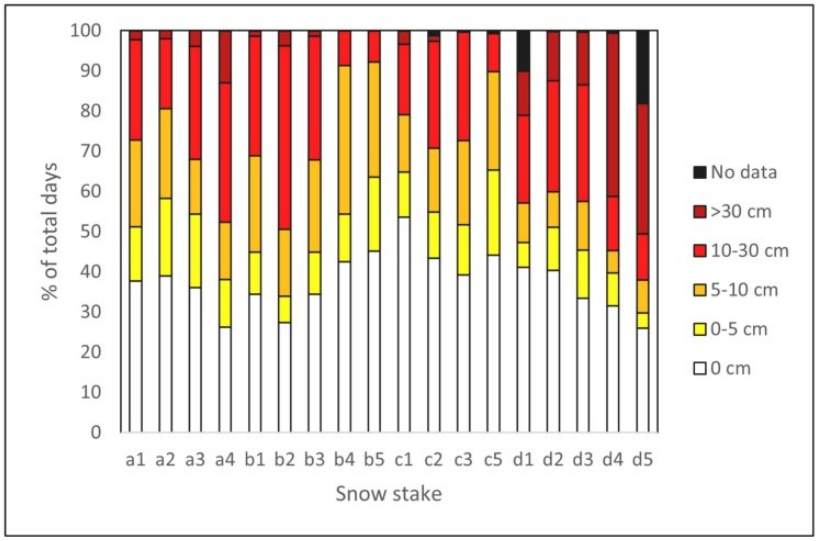

Fig. 6. Percentage of days representing five snow cover classes (0 cm, 0–5 cm, 5–10 cm, 10–30 cm, >30 cm) for each stake. The data gaps are 1% in c2 and d4), 10% in d1; 18% in d5 (18% gap).

temperatures suggested increased snowmelt in 2011 relative to 2012.

5.2. Temporal variation in snow cover and regional climatic features: ENSO and SAM

At Signy Island we measured maximum daily snow depths on the entire grid ranging between 17.1 (2017) and 50.1 cm (2015), with a maximum value of 85 cm reached by stake d2 but only for 4 days in the entire study period. These patterns differ from those observed at the Limnopolar Lake CALM site on Byers Peninsula, Livingston Island (South Shetland Islands), where De Pablo et al. (2017) showed that snow depth reached at least 80 cm each year in the period 2009–2014.

Our data showed that the snow cover season at Signy is characterized by sometimes considerable inter-annual variability in its duration, starting between 14 March and 22 April and ending between 5 November and 21 January. Hrbáček et al. (2016) also reported variability in the period of continuous snow cover at James Ross Island (Antarctic Peninsula), which lasted from 22 March to 20 September in 2011, and from 8 May to 12 December in 2012. De Pablo et al. (2017) reported low variability in snow cover onset (between 14 and 24 March) at Livingston Island in the period 2009–2014, while the cover period ended between 15 December and 15 February, showing higher variability.

The lack of a continuous snow-free season at Signy Island during the study period (Table 2) provides a further contrast with the observations of De Pablo et al. (2017), where the first and last days of continuous snow cover could be clearly identified. Comparing the MAAT between these two sites, that at Signy was always lower than at Livingstone Island (by between 0.5 and 1.8 °C), with a mean of 1 °C lower at Signy in the period 2009–2013. The colder air temperatures generally experienced at Signy Island likely underlie the different characteristics of the snow-free season at these two sites.

The statistically significant and strong negative correlation between mean annual and monthly snow depth, and mean annual and monthly air temperature (Fig. 9a, b) are consistent with results previously reported by Guglielmin et al. (2012) from the same site. This is consistent with a stronger regulatory effect of air temperature on snow depth with respect to precipitation, with increasing temperatures reducing the snow depth, as also reported in other regions of the world such as the Tibetan Plateau (Shen et al., 2021).

It is known that aspects of the Maritime Antarctic climate (air temperature, precipitation, wind) are influenced by regional circulation features such as ENSO and SAM (Clem et al., 2016; van Wessem et al., 2017). However, the relationships between the snow cover and these regional climatic features are not well known. Our data do not identify any strong relationships with these two indices. However, although not statistically significant, the negative correlation between winter SOI and mean annual snow depth over the study period was much higher (both as r and p values) than any other relationship, suggesting a more important role of ENSO than SAM in influencing temporal variability of snow cover at Signy Island.

To our knowledge, there are no other studies addressing the relationship between snow cover and ENSO/SAM in the maritime Antarctic, but studies do consider their impacts on the climate of the Antarctic Peninsula. Clem et al. (2016) showed that the atmospheric circulation changes associated with ENSO and SAM phases have impacts on Antarctic Peninsula temperatures that change both spatially and seasonally. During summer, SAM is significantly correlated with both western and north-east Peninsula temperatures, with positive SAM conditions associated with warming on the north-east Peninsula during summer but cooling on the western Peninsula. The relationship with ENSO becomes stronger during winter and spring on both sides of the Peninsula and is stronger for the western Peninsula (except during winter), while the relationship with SAM is statistically significant during all seasons for the north-east Peninsula. van Wessem et al. (2017) considered the impact of SAM end ENSO on freshwater fluxes in the Antarctic Peninsula (AP), finding a strong relationship with SAM and a weak relationship with ENSO during summer over the period 1979–2014. When a positive SAM coincides with a La Niña event, there are stronger westerly winds and snowfall is enhanced in the western Antarctic Peninsula and reduced in the eastern Peninsula, while snowmelt shows a negative anomaly to the west and a positive anomaly to the east. When a positive SAM occurs during an El Niño event, winds are more northerly and lead to enhanced orographic snowfall over the western Peninsula mountains, a reduction of snowfall and increase of rainfall over the ocean, as well as positive snow melt anomalies both in the western and eastern Peninsula. From these studies it is clear that the influences of ENSO and SAM across the Peninsula vary in both space and time. Our results are more

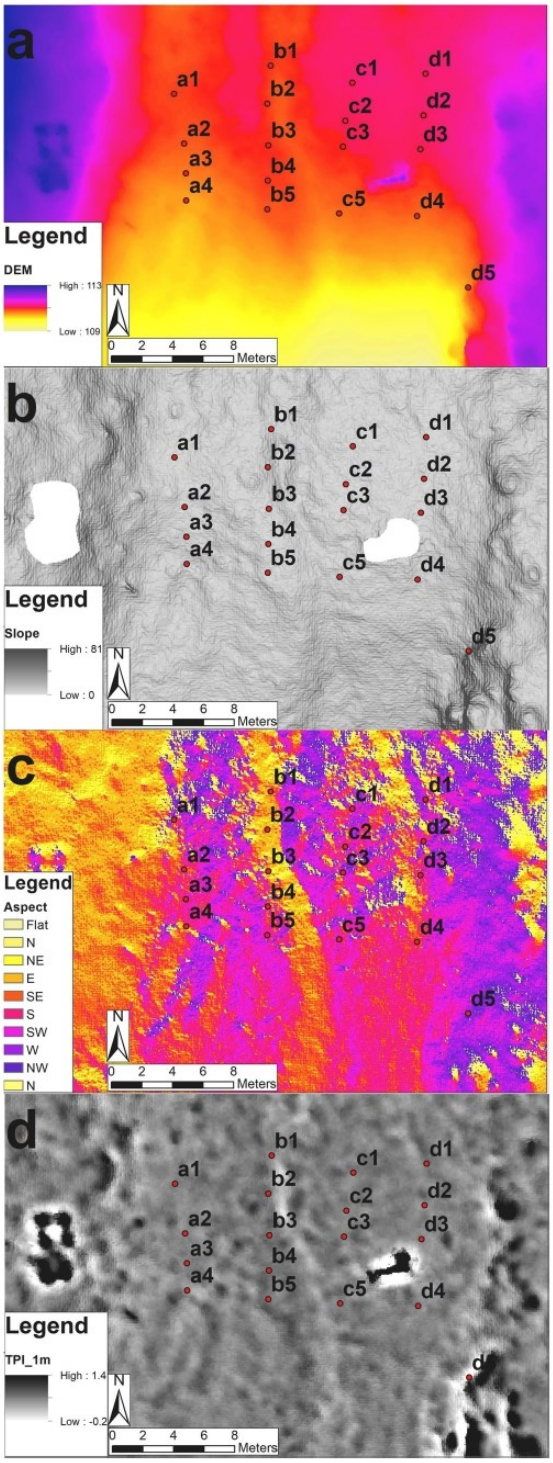

Fig. 7. Topographic maps of the study area derived from the DEM obtained from the UAV flight performed on 08/01/2018: (a) elevation (m a.s.l.); (b) slope (degrees); (c) aspect (degrees) and d) TPI at 1.0 m.

consistent with those of Clem et al. (2016), in which ENSO has stronger impact during winter, although longer time series are needed to establish the significance of the trends we observed.

5.3. Spatial snow variability: The roles of metre-submetre scale topography and of wind direction.

The high inter-annual variability of snow depth recorded at each stake within our survey grid shows that the spatial distribution and depth of snow cover is not only affected by fixed controls such as the underlying topography and vegetation, which are consistent from year to year, but that it may be related to a possible change of wind direction. Analysis of wind direction and wind speed data available from the AWS located within the snow grid for the years 2009, 2010, 2011 and 2013 offer some support for this hypothesis, with wind direction and speed changing from year to year (Fig. 2). The large spatial variability in snow depth is consistent with other studies carried out in the maritime Antarctic, for example that Guglielmin et al. (2014a,b) at Rothera Point, Adelaide Island.

The spatial variability at the grid scale showed that the snow depth was not influenced by elevation or aspect but was positively correlated with slope and negatively correlated with TPI at 1 m, as snow tends to accumulate more in depressions and less on flat surfaces. The scale of TPI influencing snow depth depends on the specific metre-submetre scale topography of this surface and on the scale at which we analysed the spatial distribution. We investigated the spatial variability of snow depth on a surface of about 15 × 20 m, with the stakes being separated by 2–5 m from each other. This is consistent with other studies indicating microtopography as the main driver of the snow cover spatial variability at the point scale (1–10 m) (e.g. López-Moreno et al., 2011).

Other studies have demonstrated the importance of TPI in influencing the spatial variability of snow depth, although at different scales. Revuelto et al. (2014) found that TPI at a scale of 25 m was the best topographic variable explaining snow depth distribution in a small mountain catchment of the central Spanish Pyrenees (ranging from 2000 to 2300 m a.s.l.). López-Moreno et al. (2017), in a study in the same mountain range but focusing on a large mountain hillslope (ranging from 1900 to 3050 m a.s.l.) found a better correlation between snow depth and TPI at 200 m radial distance and suggested that the radial distances of TPI should be adjusted depending on the characteristics of the study area.

The metre- and submetre-scale variations in snow depth found at the Signy snow grid may have potentially important implications for the ground thermal regime, influencing variation in the mean annual ground surface temperature (Davey et al., 1992; Gisnås et al., 2014; Convey et al., 2018) and underlying vegetation type (Evans et al., 1989). Documenting these variations is, therefore, a key requirement in both permafrost and ecological studies.

5.4. Relationships between snow cover and vegetation

Our data confirm the good discrimination for moss-dominated and macrolichen vegetation, while separation between soils and rocks is not easy even with high resolution images available here and as already outlined by previous studies (e.g. Vieira et al., 2014; Casanovas et al., 2015; Calviño-Cancela and Martín-Herrero, 2016; Miranda et al., 2020). Our data confirm that moss ecology with reference to moisture availability (wet, mesic, dry conditions) and the occurrence of macrolichens can be used as bioindicators of snow thickness from the thicker to the thinner, consistent with the available literature (e.g. Cannone et al., 2006; Favero-Longo et al., 2012). Xeric moss vegetation dominated by *Andreaea* spp. was associated with thinner snow cover, as reported by Collins (1976) for this species on Signy Island. This xeric community of small cushion mosses occurs in exposed, dry to moist habitats, with intermittent water supply once spring snow melt has ceased (e.g. Gimingham and Smith, 1971; Collins, 1976; Fowbert, 1996; Davey,

Table 4
Main topographic parameters calculated at each stake of the Signy snow grid from the digital elevation model: elevation (m above sea level), slope at a 0.3 m buffer (degrees), aspect at a 0.3 m buffer (degrees), TPI at 1.0 m.

	a1	a2	a3	a4	b1	b2	b3	b4	b5	c1	c2	c3	c5	d1	d2	d3	d4	d5
Mean (cm)	7.1	5.9	8.3	14.1	7.7	11.8	8.0	4.5	3.9	5.7	7.2	6.6	4.2	11.7	12.4	14.0	25.3	22.7
SD (cm)	8.5	7.9	10.9	14.6	8.3	10.5	8.5	4.9	4.6	9.0	9.0	7.4	5.6	16.2	16.5	17.6	25.7	22.2
Max (cm)	45	45	65	75	55	65	40	27	35	65	60	50	55	65	85	80	85	75
Iv (%)	−29	−41	−17	41	−23	18	−20	−55	−61	−43	−29	−34	−58	17	24	40	153	127
INV (%)	56	63	107	135	31	79	39	13	27	84	56	34	37	108	120	118	88	135

Table 5
Confusion matrix of the supervised maximum likelihood classification of the orthophoto of the study area, the table is expressed in number of pixels. Overall accuracy (OA), user's accuracy and producer's accuracy for the six classes are given (expressed in percentages).

		Reference data						
		Hygric mosses	**Rocks**	**Instruments**	**Bare ground**	**Macrolichens**	**Xeric mosses**	**User's accuracy (%)**
Classified	**Hygric mosses**	6	0	0	0	0	0	100
	Rocks	0	16	1	0	7	1	64
	Instruments	0	0	7	0	0	0	100
	Bare ground	0	0	0	20	3	0	87
	Macrolichens	0	0	0	0	17	0	100
	Xeric mosses	1	0	0	0	5	16	73
	Producer's accuracy (%)	86	100	88	100	53	94	**OA** 82%

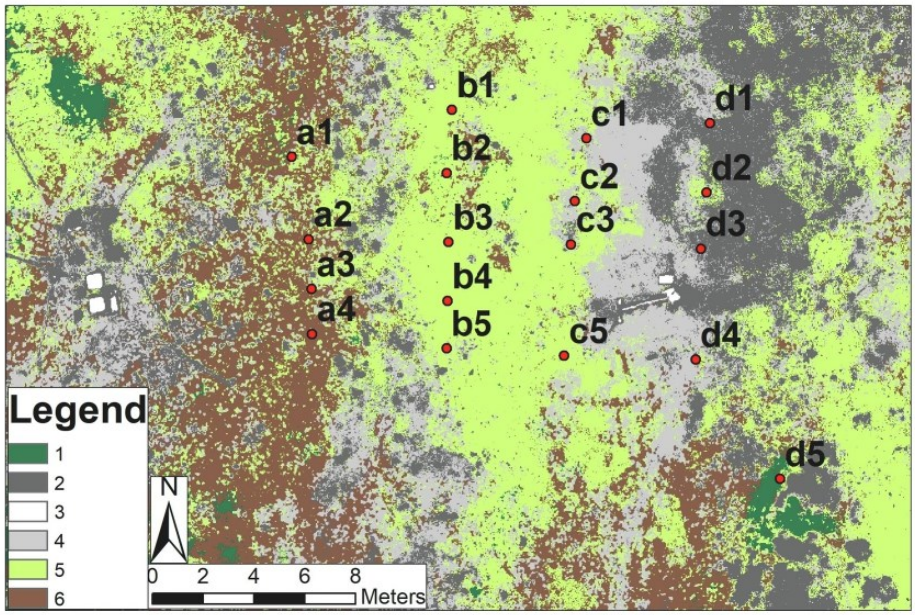

Fig. 8. Classification map of the landcover types on the orthophoto of the Signy snow grid area. A supervised maximum likelihood classification was used. The six classes are: (1) hygric mosses (Sanionia uncinata); (2) rocks; (3) instruments; (4) bare ground; (5) macrolichens (*Usnea spp., Umbilicaria, Himantormia*); (6) xeric mosses (*Andreaea spp.*). Snow stakes indicated by red dots. (For interpretation of the references to colour in this figure legend, the reader is referred to the web version of this article.)

1997). Different ecological requirements characterize the hygric moss community dominated by *Sanionia uncinata*, which is associated with the thickest snow cover in our study site, again in agreement with Collins (1976). This community requires higher water availability and occurs in mesic and hydric habitats, which are typified by continuous water supply from the onset of the spring melt through most of the growing season (Gimingham and Smith, 1971; Collins, 1976; Fowbert, 1996; Davey, 1997).

The macrolichen vegetation dominated by *Usnea* is found in a range of environments, including locations both sheltered from and exposed to strong winds, as well as in both humid and dry areas (Schroeter et al., 1995; Smith, 1996; Øvstedal and Smith, 2001; Schlensog et al., 2013; Vieira et al., 2014). Our analyses indicate that this vegetation is limited to areas with low mean snow cover, consistent with the suggestion of Vieira et al. (2014) that this vegetation formation can be used as an indicator of low snow accumulation. Moreover, our data show that presence of this vegetation is associated with earlier snow melt (as shown in Fig. 5c), as the structure, colour and thermal properties of the macrolichen favour the early melting and delay snow accumulation (Cannone et al., 2006). Manipulation experiments on Signy Island

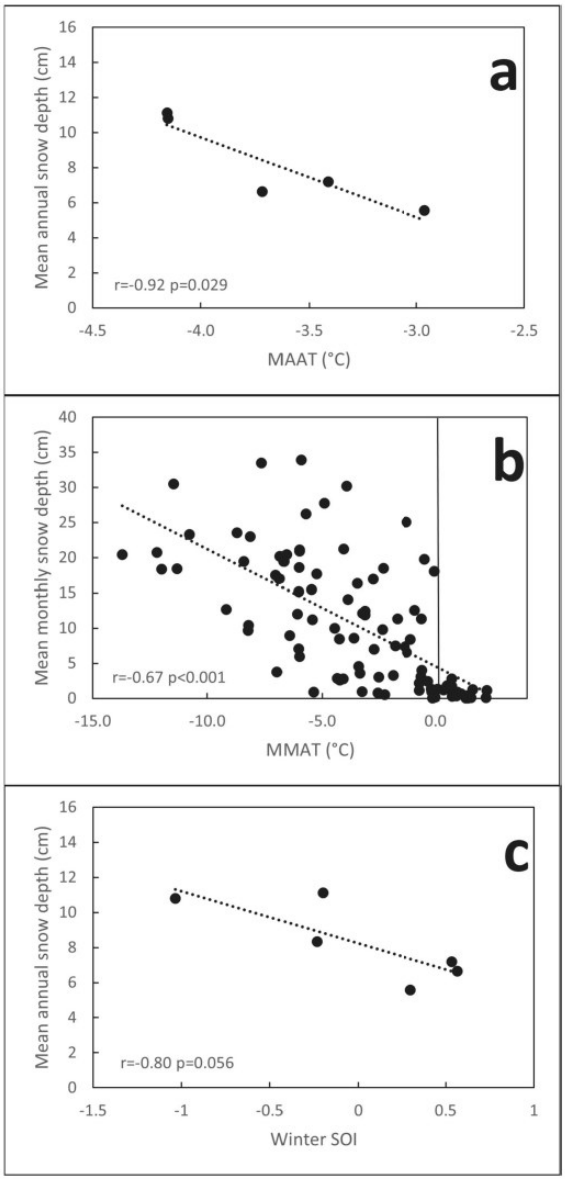

Fig. 9. Relationships between mean annual snow depth (cm) and climatic factors: (a) mean annual air temperature (MAAT °C); (b) mean monthly air temperature (MMAT °C) and SOI index.

simulating predicted climate changes showed that *U. antarctica* declined inside Open Top Chambers (OTC) and suggested that this trend was most likely caused by greater winter snow accumulation associated with an increase in net winter respiration rates driven by the higher temperatures and lower light levels inside the OTCs (Bokhorst et al., 2016). The current study's data confirm the ecological association of this macrolichen vegetation with shallow snow cover and illustrate the potential high sensitivity of this vegetation type to increases in winter snow depth or duration.

6. Conclusions

Consistent with our hypotheses, our data confirmed that snow cover depth is influenced by air temperature, showing a strong negative correlation, meaning that current and future air warming could decrease snow depth in this area. We also highlight the potential influence of regional climatic features on snow cover, with a negative correlation between winter SOI and mean annual snow depth, implying that ENSO (and not SAM) influences snow cover in this part of Antarctica. Our data demonstrate the importance of microtopography and wind direction, as well as of land cover type (vegetation), on snow cover patterns, as these factors influence the processes of accumulation, redistribution and ablation of snow. Our study highlights the importance of the spatial monitoring of snow accumulation at small physical scale in order to predict future effects of climatic change on sensitive maritime Antarctic terrestrial ecosystems.

Declaration of Competing Interest

The authors declare that they have no known competing financial interests or personal relationships that could have appeared to influence the work reported in this paper.

Acknowledgments

We thank the British Antarctic Survey for logistical support in the different Antarctic campaigns and, in particular, Alex Taylor for providing the UAV image of the grid. This research was funded by the grant PNRA 2016_00224. Peter Convey is supported by NERC core funding to the British Antarctic Survey's 'Biodiversity, Evolution and Adaptation' Team. We also thank two anonymous reviewers and the Editor for their helpful suggestions.

Appendix A. Supplementary material

Supplementary data to this article can be found online at https://doi.org/10.1016/j.catena.2021.105739.

References

Arndt, S., Paul, S., 2018. Variability of winter snow properties on different spatial scales in the Weddell Sea. J. Geophys. Res. Oceans 123 (12), 8862–8876.
Arthern, R.J., Winebrenner, D.P., Vaughan, D.G., 2006. Antarctic snow accumulation mapped using polarization of 4.3-cm wavelength microwave emission. J. Geophys. Res.: Atmos. 111 (D6).
Banta, J.R., McConnell, J.R., Frey, M.M., Bales, R.C., Taylor, K., 2008. Spatial and temporal variability in snow accumulation at the West Antarctic Ice Sheet Divide over recent centuries. J. Geophys. Res.: Atmos. 113 (D23).
Bertler, N.A., Conway, H., Dahl-Jensen, D., Emanuelsson, D.B., Winstrup, M., Vallelonga, P.T., Keller, E.D., 2018. The Ross Sea Dipole - temperature, snow accumulation and sea ice variability in the Ross Sea region, Antarctica, over the past 2700 years. Clim. Past 14, 193–214.
Bokhorst, S., Convey, P., Huiskes, A.d., Aerts, R., 2016. *Usnea antarctica*, an important Antarctic lichen, is vulnerable to aspects of regional environmental change. Polar Biol. 39 (3), 511–521.
Borner, A.P., Kielland, K., Walker, M.D., 2008. Effects of simulated climate change on plant phenology and nitrogen mineralization in Alaskan Arctic tundra. Arct. Antarct. Alp. Res. 40 (1), 27–38.
Braaten, D.A., 2000. Direct measurements of episodic snow accumulation on the Antarctic polar plateau. J. Geophys. Res.: Atmos. 105 (D8), 10119–10128.
Brown, R.D., Robinson, D.A., 2005. Snow and Snow Cover. In: Oliver, J.E. (Eds.), Encyclopedia of World Climatology. Encyclopedia of Earth Sciences Series. Springer, Dordrecht.
Callaghan, T.V., Johansson, M., Brown, R.D., Groisman, P.Y., Labba, N., Radionov, V., Bradley, R.S., Blangy, S., Bulygina, O.N., Christensen, T.R., Colman, J.E., Essery, R.L. H., Forbes, B.C., Forchhammer, M.C., Golubev, V.N., Honrath, R.E., Juday, G.P., Meshcherskaya, A.V., Phoenix, G.K., Pomeroy, J., Rautio, A., Robinson, D.A., Schmidt, N.M., Serreze, M.C., Shevchenko, V.P., Shiklomanov, A.I., Shmakin, A.B., Sköld, P., Sturm, M., Woo, M.-k., Wood, E.F., 2011. Multiple effects of changes in Arctic snow cover. Ambio 40 (S1), 32–45.
Calviño-Cancela, M., Martín-Herrero, J., 2016. Spectral discrimination of vegetation classes in ice-free areas of Antarctica. Remote Sensing 8 (10), 856. https://doi.org/10.3390/rs8100856.

Cannone, N., Ellis Evans, J.C., Strachan, R., Guglielmin, M., 2006. Interactions between climate, vegetation and the active layer in soils at two Maritime Antarctic sites. Antarct. Sci. 18 (3), 323–333.
Casanovas, P., Black, M., Fretwell, P., Convey, P., 2015. Mapping lichen distribution on the Antarctic Peninsula using remote sensing, lichen spectra and photographic documentation by citizen scientists. Polar Res. 34 (1), 25633. https://doi.org/10.3402/polar.v34.25633.
Clem, K.R., Renwick, J.A., McGregor, J., Fogt, R.L., 2016. The relative influence of ENSO and SAM on Antarctic Peninsula climate. J. Geophys. Res.: Atmos. 121 (16), 9324–9341.
Cockell, C.S., Rettberg, P., Horneck, G., Wynn-Williams, D.D., Scherer, K., Gugg-Helminger, A., 2002. Influence of ice and snow covers on the UV exposure of terrestrial microbial communities: dosimetric studies. J. Photochem. Photobiol., B 68 (1), 23–32.
Collins, N.J., 1976. The development of moss-peat banks in relation to changing climate and ice cover on Signy Island in the maritime Antarctic. British Antarctic Survey Bulletin 43, 85–102.
Convey, P., Abbandonato, H., Bergan, F., Beumer, L.T., Biersma, E.M., Bråthen, V.S., D'Imperio, L., Jensen, C.K., Nilsen, S., Paquin, K., Stenkewitz, U., Svoen, M.E., Winkler, J., Müller, E., Coulson, S.J., 2015. Survival of rapidly fluctuating natural low winter temperatures by High Arctic soil invertebrates. J. Therm. Biol. 54, 111–117.
Convey, P., Coulson, S.J., Worland, M.R., Sjöblom, A., 2018. The importance of understanding annual and shorter term temperature patterns and variation in the upper layers of polar soils for terrestrial biota. Polar Biol. 41, 1587–1605.
Davey, M.C., Pickup, J., Block, W., 1992. Temperature variation and its biological significance in fellfield habitats on a maritime Antarctic island. Antarct. Sci. 4 (4), 383–388.
Davey, M.C., 1997. Effects of short-term dehydration and rehydration on photosynthesis and respiration by Antarctic bryophytes. Environ. Exp. Bot. 37 (2-3), 187–198.
de Pablo, M.A., Ramos, M., Molina, A., 2017. Snow cover evolution, on 2009–2014, at the Limnopolar Lake CALM-S site on Byers Peninsula, Livingston Island, Antarctica. Catena 149, 538–547.
De Reu, J., Bourgeois, J., Bats, M., Zwertvaegher, A., Gelorini, V., De Smedt, P., Chu, W., Antrop, M., De Maeyer, P., Finke, P., Van Meirvenne, M., Verniers, J., Crombé, P., 2013. Application of the topographic position index to heterogeneous landscapes. Geomorphology 186, 39–49.
Evans, B.M., Walker, D.A., Benson, C.S., Nordstrand, E.A., Petersen, G.W., 1989. Spatial interrelationships between terrain, snow distribution and vegetation patterns at an arctic foothills site in Alaska. Holoarctic Ecology 12, 270–278.
Fassnacht, S.R., López-Moreno, J.I., Toro, M., Hultstrand, D.M., 2013. Mapping snow cover and snow depth across the Lake Limnopolar watershed on Byers Peninsula, Livingston Island, Maritime Antarctica. Antarct. Sci. 25 (2), 157–166.
Favero-Longo, S.E., Worland, M.R., Convey, P., Lewis Smith, R.I., Piervittori, R., Guglielmin, M., Cannone, N., 2012. Primary succession of lichen and bryophyte communities following glacial recession on Signy Island, South Orkney Islands, Maritime Antarctic. Antarct. Sci. 24 (4), 323–336.
Fowbert, J.A., 1996. An experimental study of growth in relation to morphology and shoot water content in maritime Antarctic mosses. New Phytologist 133, 363–373.
Frezzotti, M., Pourchet, M., Flora, O., Gandolfi, S., Gay, M., Urbini, S., Vincent, C., Becagli, S., Gragnani, R., Proposito, M., Severi, M., Traversi, R., Udisti, R., Fily, M., 2005. Spatial and temporal variability of snow accumulation in East Antarctica from traverse data. J. Glaciol. 51 (172), 113–124.
Genthon, C., Six, D., Scarchilli, C., Ciardini, V., Frezzotti, M., 2016. Meteorological and snow accumulation gradients across Dome C, East Antarctic plateau. Int. J. Climatol. 36 (1), 455–466.
Gimingham, C.H., Smith, R.I.L., 1970. Bryophyte and lichen communities in the maritime Antarctic. In: Holdgate, M.W. (Ed.), Antarctic Ecology. Academy Press, London, pp. 752–785.
Gimingham, C.H., Smith, R.I.L., 1971. Growth form and water relations of mosses in the maritime Antarctic. Br. Antarctic Survey Bull. 25, 1–21.
Gisnås, K., Westermann, S., Schuler, T.V., Litherland, T., Isaksen, K., Boike, J., Etzelmüller, B., 2014. A statistical approach to represent small-scale variability of permafrost temperatures due to snow cover. The Cryosphere 8 (6), 2063–2074.
Gooseff, M.N., Barrett, J.E., Doran, P.T., Fountain, A.G., Lyons, W.B., Parsons, A.N., Porazinska, D.L., Virginia, R.A., Wall, D.H., 2003. Snow-patch influence on soil biogeochemical processes and invertebrate distribution in the McMurdo Dry Valleys, Antarctica. Arct. Antarct. Alp. Res. 35 (1), 91–99.
Green, T.G.A., Sancho, L.G., Pintado, A., Schroeter, B., 2011. Functional and spatial pressures on terrestrial vegetation in Antarctica forced by global warming. Polar Biol. 34 (11), 1643–1656.
Guglielmin, M., Dalle Fratte, M., Cannone, N., 2014a. Permafrost warming and vegetation changes in continental Antarctica. Environ. Res. Lett. 9 (4), 045001. https://doi.org/10.1088/1748-9326/9/4/045001.
Guglielmin, M., Ellis Evans, C.J., Cannone, N., 2008. Active layer thermal regime under different vegetation conditions in permafrost areas. A case study at Signy Island (Maritime Antarctica). Geoderma 144 (1-2), 73–85.
Guglielmin, M., Worland, M.R., Cannone, N., 2012. Spatial and temporal variability of ground surface temperature and active layer thickness at the margin of maritime Antarctica, Signy Island. Geomorphology 155-156, 20–33.
Guglielmin, M., Worland, M.R., Baio, F., Convey, P., 2014b. Permafrost and snow monitoring at Rothera Point (Adelaide Island, Maritime Antarctica): Implications for rock weathering in cryotic conditions. Geomorphology 225, 47–56.
Hinkel, K.M., Nelson, F.E., 2003. Spatial and temporal patterns of active layer thickness at Circumpolar Active Layer Monitoring (CALM) sites in northern Alaska, 1995–2000. J. Geophys. Res.: Atmos. 108 (D2), 8168.
Hrbáček, F., Láska, K., Engel, Z., 2016. Effect of snow cover on the active-layer thermal regime–a case study from James Ross island, Antarctic Peninsula. Permafrost Periglacial Process. 27 (3), 307–315.
Hrbáček, F., Engel, Z., Knažková, M., Smolíková, J., 2021. Effect of summer snow cover on the active layer thermal regime and thickness on CALM-S JGM site, James Ross Island, eastern Antarctic Peninsula. Catena 207, 105608. https://doi.org/10.1016/j.catena.2021.105608.
Kappen, L., Sommerkorn, M., Schroeter, B., 1995. Carbon acquisition and water relations of lichens in polar regions—potentials and limitations. The Lichenologist 27 (6), 531–545.
Keller, F., Gubler, H., 1993. Interaction between snow cover and high mountain permafrost, Murtel –Corvatsch, Swiss Alps. 6th International Conference on Permafrost, Beijing, China, vol. 1. South China University of Technology Press, Beijing, pp. 332–337.
Liston, G.E., Sturm, M., 1998. A snow-transport model for complex terrain. J. Glaciol. 44 (148), 498–516.
López-Moreno, J.I., Fassnacht, S.R., Beguería, S., Latron, J.B.P., 2011. Variability of snow depth at the plot scale: implications for mean depth estimation and sampling strategies. The Cryosphere 5 (3), 617–629.
López-Moreno, J.I., Revuelto, J., Alonso-González, E., Sanmiguel-Vallelado, A., Fassnacht, S.R., Deems, J., Morán-Tejeda, E., 2017. Using very long-range terrestrial laser scanner to analyze the temporal consistency of the snowpack distribution in a high mountain environment. J. Mountain Sci. 14 (5), 823–842.
Massom, R.A., Lytle, V.I., Worby, A.P., Allison, I., 1998. Winter snow cover variability on East Antarctic sea ice. J. Geophys. Res. Oceans 103 (C11), 24837–24855.
Miranda, V., Pina, P., Heleno, S., Vieira, G., Mora, C., Schaefer, C.E.G.R., 2020. Monitoring recent changes of vegetation in Fildes Peninsula (King George Island, Antarctica) through satellite imagery guided by UAV surveys. Sci. Total Environ. 704.
Mott, R., Vionnet, V., Grünewald, T., 2018. The Seasonal Snow Cover Dynamics: Review on Wind-Driven Coupling Processes. Front. Earth Sci. 6, 197. https://doi.org/10.3389/feart.2018.00197.
Neumann, N.N., Derksen, C., Smith, C., Goodison, B., 2006. Characterizing local scale snow cover using point measurements during the winter season. Atmos. Ocean 44 (3), 257–269.
Oliva, M., Navarro, F., Hrbáček, F., Hernández, A., Nývlt, D., Pereira, P., Ruiz-Fernández, J., Trigo, R., 2017. Recent regional climate cooling on the Antarctic Peninsula and associated impacts on the cryosphere. Sci. Total Environ. 580, 210–223.
Øvstedal, D.O., Smith, R.I.L., 2001. Lichens of Antarctica and South Georgia. A Guide to their Identification and Ecology. Cambridge University Press, Cambridge, p. 411.
Pannewitz, S., Schlensog, M., Green, T.G.A., Sancho, L.G., Schroeter, B., 2003. Are lichens active under snow in continental Antarctica? Oecologia 135 (1), 30–38.
Perovich, D.K., 2007. Light reflection and transmission by a temperate snow cover. J. Glaciol. 53 (181), 201–210.
Pfaffhuber, A.A., Lieser, J.L., Haas, C., 2017. Snow thickness profiling on Antarctic sea ice with GPR—Rapid and accurate measurements with the potential to upscale needles to a haystack. Geophys. Res. Lett. 44 (15), 7836–7844.
Revuelto, J., López-Moreno, J.I., Azorín-Molina, C., Vicente-Serrano, S.M., 2014. Topographic control of snowpack distribution in a small catchment in the central Spanish Pyrenees: intra-and inter-annual persistence. The Cryosphere 8 (5), 1989–2006.
Richardson, C., Aarholt, E., Hamran, S.-E., Holmlund, P., Isaksson, E., 1997. Spatial distribution of snow in western Dronning Maud Land, East Antarctica, mapped by a ground-based snow radar. J. Geophys. Res. Solid Earth 102 (B9), 20343–20353.
Rotschky, G., Holmlund, P., Isaksson, E., Mulvaney, R., Oerter, H., Van Den Broeke, M.R., Winther, J.-G., 2007. A new surface accumulation map for western Dronning Maud Land, Antarctica, from interpolation of point measurements. J. Glaciol. 53 (182), 385–398.
Royles, J., Ogée, J., Wingate, L., Hodgson, D.A., Convey, P., Griffiths, H., 2012. Carbon isotope evidence for recent climate-related enhancement of CO_2 assimilation and peat accumulation rates in Antarctica. Glob. Change Biol. 18, 3112–3124.
Schneider, S., Hoelzle, M., Hauck, C., 2012. Influence of surface and subsurface heterogeneity on observed borehole temperatures at a mountain permafrost site in the Upper Engadine, Swiss Alps. The Cryosphere 6 (2), 517–531.
Schlensog, M., Green, T.G.A., Schroeter, B., 2013. Life form and water source interact to determine active time and environment in cryptogams: an example from the maritime Antarctic. Oecologia 173 (1), 59–72.
Schroeter, B., Olech, M., Kappen, L., Heitland, W., 1995. Ecophysiological investigations of *Usnea antarctica* in the maritime Antarctic. I. Annual microclimate conditions and potential primary production. Antarct. Sci. 7, 251–260.
Shen, L., Zhang, Y., Ullah, S., Pepin, N., Ma, Q., 2021. Changes in snow depth under elevation-dependent warming over the Tibetan Plateau. Atmos. Sci. Lett. e1041.
Smith, R.I.L., 1972. Vegetation of the South Orkney Islands with particular reference to Signy Island. British Antarctic Survey Scientific Reports No. 68. British Antarctic Survey, Cambridge.
Smith, R.I.L., 1996. Terrestrial and freshwater biotic components of the western Antarctic Peninsula. In: Hofmann, E.E., Ross, R.M., Quetin, L.B. (Eds.), Foundations for Ecological Research West of the Antarctic Peninsula, Antarctic Research Series, vol. 70. American Geophysical Union, Washington, pp. 15–59.
Smith, R.I.L., 2007. Half a continent in a square kilometre: the exceptional lichen diversity of a small Antarctic island. Bibliotheca Lichenologica 95, 387–403.
Smith, S.L., Wolfe, S.A., Riseborough, D.W., Nixon, F.M., 2009. Active-layer characteristics and summer climatic indices, Mackenzie Valley, Northwest Territories, Canada. Permafrost Periglac. Process. 20 (2), 201–220.

van Wessem, J.M., Meredith, M.P., Reijmer, C.H., van den Broeke, M.R., Cook, A.J., 2017. Characteristics of the modelled meteoric freshwater budget of the western Antarctic Peninsula. Deep Sea Res. Part II 139, 31–39.
Vieira, G., Mora, C., Pina, P., Schaefer, C.E.R., 2014. A proxy for snow cover and winter ground surface cooling: mapping *Usnea* sp. communities using high resolution remote sensing imagery (maritime Antarctica). Geomorphology 225, 69–75.
Walker, D.A., Billings, W.D., De Molenaar, J.G., 2001. Snow-vegetation interactions in tundra environments. Snow Ecol. 266–324.
Winkler, J.B., Kappen, L., Schulz, F., 2000. Snow and ice as an important ecological factor for the cryptogams in the maritime Antarctic. In: Davison, W., Howard-Williams, C., Broady, P. (Eds.), Antarctic Ecosystems: Models for a Wider Ecological Understanding. New Zealand Natural Sciences, Christchurch, New Zealand, pp. 220–224.
Worby, A.P., Markus, T., Steer, A.D., Lytle, V.I., Massom, R.A., 2008. Evaluation of AMSR-E snow depth product over East Antarctic sea ice using in situ measurements and aerial photography. J. Geophys. Res. Oceans 113 (C5).
Zhang, T., 2005. Influence of the seasonal snow cover on the ground thermal regime: An overview. Rev. Geophys. 43, RG4002.

Appendix A. Supplementary material

The following are the Supplementary data to this article:

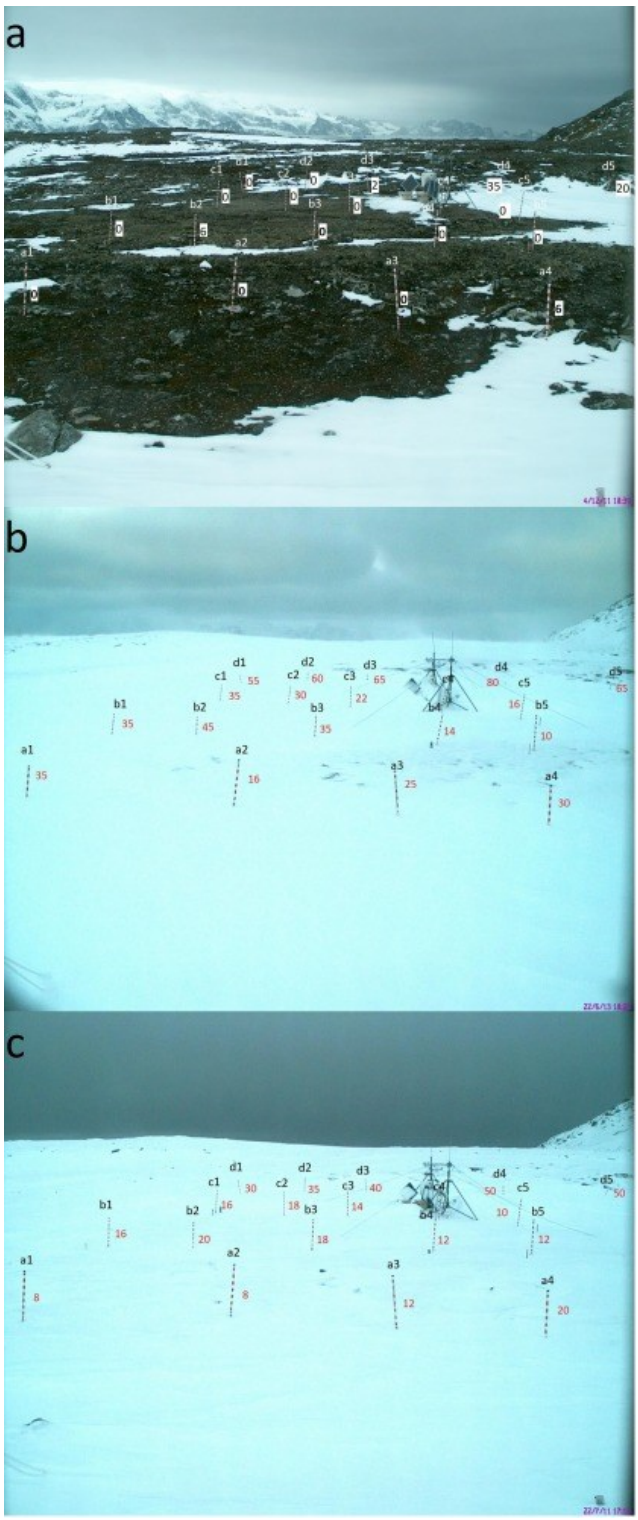

Supplementary Fig. S1.

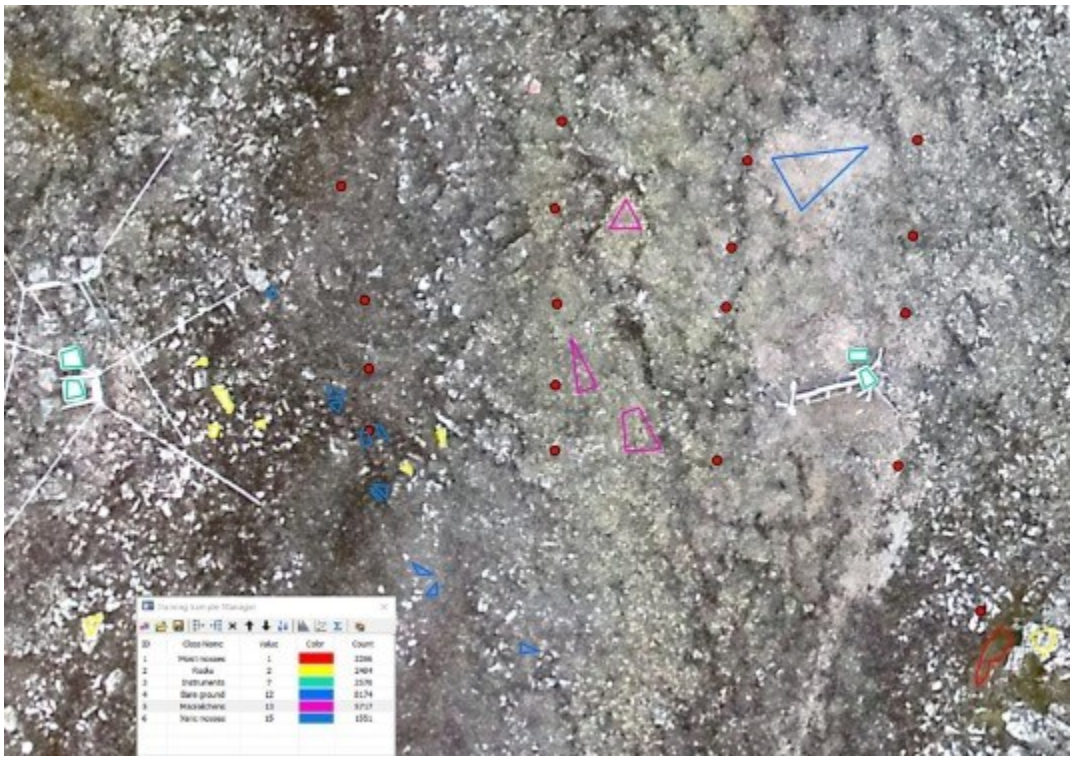

Supplementary Fig. S2.

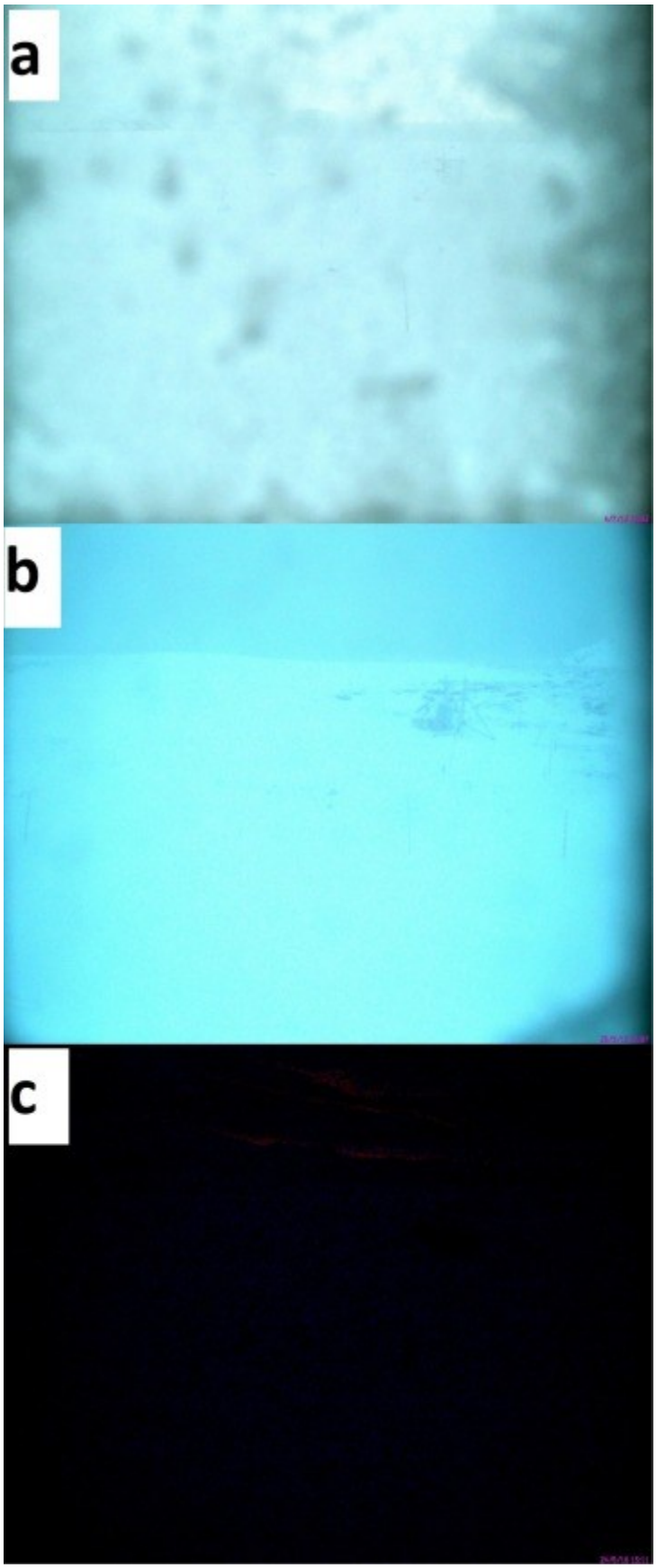

Supplementary Fig. S3.

3. Using ground-based thermography to analyse surface temperature distribution and estimate debris thickness on Gran Zebrù glacier (Ortles-Cevedale, Italy)

Cold Regions Science and Technology 196 (2022) 103487

Contents lists available at ScienceDirect

Cold Regions Science and Technology

journal homepage: www.elsevier.com/locate/coldregions

Using ground-based thermography to analyse surface temperature distribution and estimate debris thickness on Gran Zebrù glacier (Ortles-Cevedale, Italy)

Giulia Tarca, Mauro Guglielmin *

Department of Theoretical and Applied Sciences, Insubria University, Via J.H. Dunant, 3, 21100 Varese, Italy

ARTICLE INFO

Keywords:
Thermography
Glacier
Surface temperatures
Supraglacial debris

ABSTRACT

In this paper we used ground-based thermal infrared imaging to investigate the spatial variability of surface temperatures on a mountain glacier at high spatial resolution and to estimate the supraglacial debris thickness distribution. The surveyed area is the eastern tongue of Gran Zebrù glacier, a small mountain glacier of the Ortles-Cevedale group (Italy). A FLIR E85 Thermal Camera was used to obtain a panoramic thermal image of the glacier surface on 30 September 2019 that was calibrated and georeferenced in order to obtain surface temperatures.

Based on field data, debris thickness and debris surface temperature were correlated by using an exponential equation. The equation was used to estimate debris thickness on the glacier from the temperature data.

The results show a spatial variability of surface temperatures, with the lowest temperatures found on snow and ice surfaces, and the highest on supraglacial debris. The estimated debris thicknesses show an inhomogeneous distribution, with a calculated mean debris thickness of 0.09 m in the areas of continous debris coverage. We found a good correspondence between measured and estimated debris thickness at 30 validation points (RMSE = 0.04 m and r = of 0.92). We demonstrated that ground-based thermal imaging can provide very high resolution maps of glacier surface temperatures and of debris thickness that can be used for the estimation of glacier ablation, with a spatial resolution more suitable than that offered by satellite data, especially for glaciers with a small area and with a heterogeneous surface.

1. Introduction

Surface temperature is an important parameter for estimating the effect of climate change on glaciers (Haq, Jain, and Menon, 2013) and is influenced by the presence of supraglacial debris (e.g. Lo Vecchio et al., 2018).

Debris cover on glaciers influences melt rates, with an increase of the ablation rate under thin layers (less than the 'critical thickness') compared to clean ice, and a decrease in case of thick debris cover (Östrem, 1959). The 'critical thickness' is defined as the thickness at which the melt rate is equivalent to that on bare ice (Nakawo and Rana, 1999). Having an important effect on ablation, debris cover consequently influences mass balance and glacier behaviour (e.g. Reznichenko, Davies, Shulmeister, and McSaveney, 2010). Therefore, it is important to correctly quantify not only the extension of the debris cover on glaciers, but also its thickness.

Surface temperatures derived from thermal infrared (TIR) satellite imagery, like ASTER, Landsat 7 and Landsat 8, have been previously used to estimate debris thicknesses for glacier surfaces. Some studies took advantage from the relationship existing between surface temperature and debris thickness that is obtained experimentally, and applied it to the thermal data derived from satellite to infer debris thicknesses on the entire glacier (e.g. Mihalcea et al., 2008a; Mihalcea et al., 2008b; Soncini et al., 2016). Warmer areas are correlated to a thicker debris cover, while colder areas correspond to a thin debris cover (e.g. Taschner and Ranzi, 2002). Other studies employing satellite data combined surface temperature estimates with energy balance models (Foster, Brock, Cutler, and Diotri, 2012; Rounce and McKinney, 2014; Schauwecker et al., 2015). Satellite thermal imagery is characterized by a low spatial resolution, with pixel sizes of 60 m Landsat 7, 90 m ASTER and 100 m Landsat 8 respectively, not being able to represent the local variability of debris thickness. Indeed, debris thickness can vary greatly

* Corresponding author.
E-mail address: mauro.guglielmin@uninsubria.it (M. Guglielmin).

https://doi.org/10.1016/j.coldregions.2022.103487
Received 19 May 2020; Received in revised form 30 October 2021; Accepted 14 January 2022
Available online 20 January 2022

over short spatial scales and a higher resolution will more clearly constrain its heterogeneity. Moreover, quantifying the small-scale spatial distribution of debris is important to understand how it influences ablation and therefore impact glacier behaviour (Nicholson, McCarthy, Pritchard, and Willis, 2018).

Infrared thermal imaging (or thermography) is a method that detects the radiation emitted by an object in the infrared range of the electromagnetic spectrum. According to the Stefan-Boltzmann law, there is a relation between radiated energy and temperature, therefore it is possible to calculate the temperature of a material by measuring its radiation emission (Shea and Jamieson, 2011).

At the best of our knowledge there are few studies that have used high-resolution infrared thermal imaging to map surface temperatures on glaciers. Hopkinson, Barlow, Demuth, and Pomeroy (2010) used oblique thermal imagery and lidar to map spatial and temporal moraine temperature patterns on the Peyto Glacier (Rocky Mountains, Canada), Aubry-Wake et al. (2015) used ground-based thermal infrared imagery to obtain spatially distributed surface temperature on the Cuchillacocha Glacier (Cordillera Blanca, Peru), while Kraaijenbrink et al. (2018) used a thermal infrared sensor mounted on an unmanned aerial vehicle (UAV) to map surface temperatures on the debris-covered Lirung Glacier (Central Himalaya, Nepal). Distributed glacier surface temperature could be useful to evaluate glacier melt patterns or to evaluate melt models. Nevertheless, ground-based thermography has never been used to estimate debris thicknesses on glaciers.

The main aims of this study are to use ground-based thermal infrared imagery: i) to understand the spatial variability of surface temperatures and II) to estimate the debris thickness distribution on the same glacier at high spatial resolution.

2. Study area

The investigated area is the eastern tongue of Gran Zebrù glacier. Gran Zebrù glacier is a mountain glacier of the Ortles-Cevedale group (Central Italian Alps) and it's located in Cedec Valley, Valtellina (Fig. 1). The eastern tongue has a south-facing aspect and currently covers an

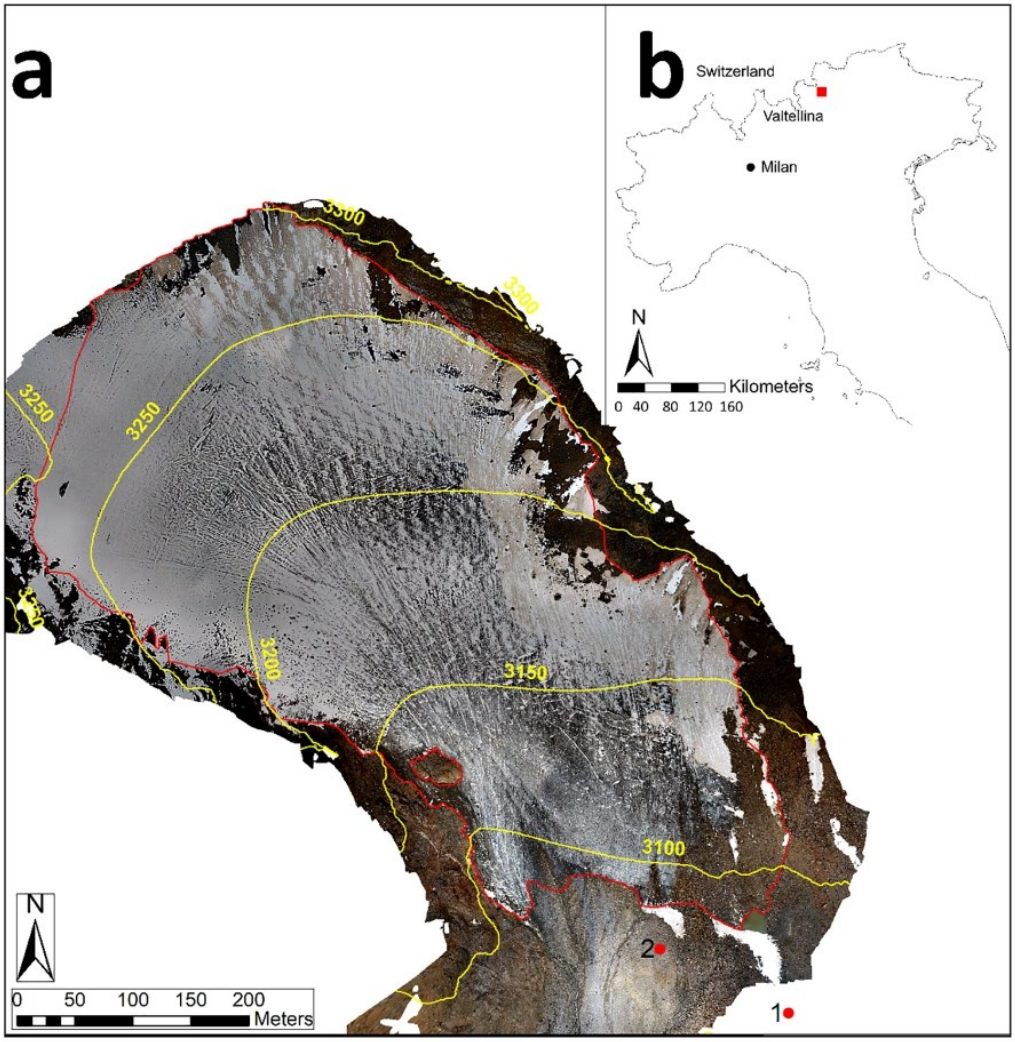

Fig. 1. Location of Gran Zebrù glacier. a) Eastern tongue of Gran Zebrù glacier. The red line represents the glacier outline in 2019. Point 1 represents the position of the thermal camera. Point 2 is the location of the automatic weather station. Base map is an orthophoto of 2019. In yellow are the contour lines every 50 m. b) Location of Gran Zebrù glacier (red square) respect to Italy. (For interpretation of the references to colour in this figure legend, the reader is referred to the web version of this article.)

area of 0.22 km^2, extending between 3080 and 3300 m a.s.l. The glacier has a mean slope of 20 degrees and a standard deviation of 8 degrees.

The Ortles-Cevedale glaciers underwent a reduction of surface area of approximately 40% from 1954 to 2007 (D'Agata, Bocchiola, Maragno, Smiraglia, and Diolaiuti, 2014).

Part of the glacier surface is debris covered and with sparse debris also present, particularly on the lowest elevations. Geologically, the glacier covers an area characterized by the tectonic Zebrù line, dividing the Campo Nappe (south) from the Ortler Nappe (north), the first composed mainly of micaschist and paragneiss, the second of dolomite and limestone (Montrasio et al., 2012).

3. Data and methods

3.1. Data

We used a hand-held FLIR E85 Thermal Camera to take thermal images of the glacier surface on 30 September 2019 at 11.18 (local time, GMT +2). A total of 17 photos were taken to cover the entire surface. The camera has a spectral range of 7.5–14.0 μm, an IR Resolution of 384 × 288 (110,592 pixels) and an accuracy of ±2 K. The field of view is 24° x 18°. The camera takes also visible images of the scenes with a 5 MP resolution. The images were taken from a rocky spur in front of the glacier (46.466758 N, 10.581539 E), at about 100 m from the glacier margin (Fig. 1).

Meteorological data were recorded by an automatic weather station (AWS) installed near the glacier front. The AWS (Fig. 1) recorded air temperature and relative humidity at a height of 1.60 m.

An ASTER (Advanced Spaceborne Thermal Emission and Reflection Radiometer) scene of the study area that was acquired on 20/09/2019 at 10.21 (GMT, corresponding to 12.21 local time) was obtained from the Nasa Earth Science Data site (https://earthdata.nasa.gov/), since there were no available scenes of the same day of the thermal images. ASTER is an imaging instrument onboard the Terra satellite that is part of the NASA's Earth Observing System (EOS) and was launched in December 1999. We used from the ASTER level 2 products the ASTER Surface Kinetic Temperature (AST_08) product (Abrams, Hook, and Ramachandran, 2002), generated using the five Thermal Infrared (TIR) bands between 8 and 12 μm spectral range representing the surface temperatures at 90 m spatial resolution. It has an absolute accuracy of 1–4 K and a relative accuracy of 0.3 K.

3.2. Methods

We used the Panorama Tool of the FLIR Tools+ software to combine the multiple thermal images taken to cover the entire glacier surface and create a single panoramic image (Fig. 2a). The same procedure was carried out to obtain a visible panoramic image (Fig. 2b).

The temperatures obtained from the thermal camera are uncorrected *brightness temperatures* that need to be calibrated in order to derive the actual surface temperatures (Shea and Jamieson, 2011; Guerin et al., 2019). The panoramic thermal image was calibrated using the FLIR Tools+ software, setting emissivity, air temperature, relative humidity, distance and reflected temperature. An emissivity of 0.97 was set, as the value is found to be used both for glacier ice (Aubry-Wake et al., 2015) and rock (Cardenas et al., 2014) in literature. Air temperature and relative humidity from the AWS (respectively 2.9 °C and 72.5%) were used to correct the thermal images to obtain surface temperatures. The distance was set at 550 m, as the images were taken at about 100 m from the glacier front, while the further section of the glacier is 1000 m away, so a mean value was chosen. The reflected temperature was set to −20 °C. It was measured using the thermal camera on a crumpled and unfolded aluminium foil, setting an emissivity of one (Usamentiaga et al., 2014). The aluminium foil acts as a Lambert radiator, reflecting the incident radiation in every direction (Porras-Amores, Mazarrón, and Cañas, 2013). The calibration process implies some simplifications,

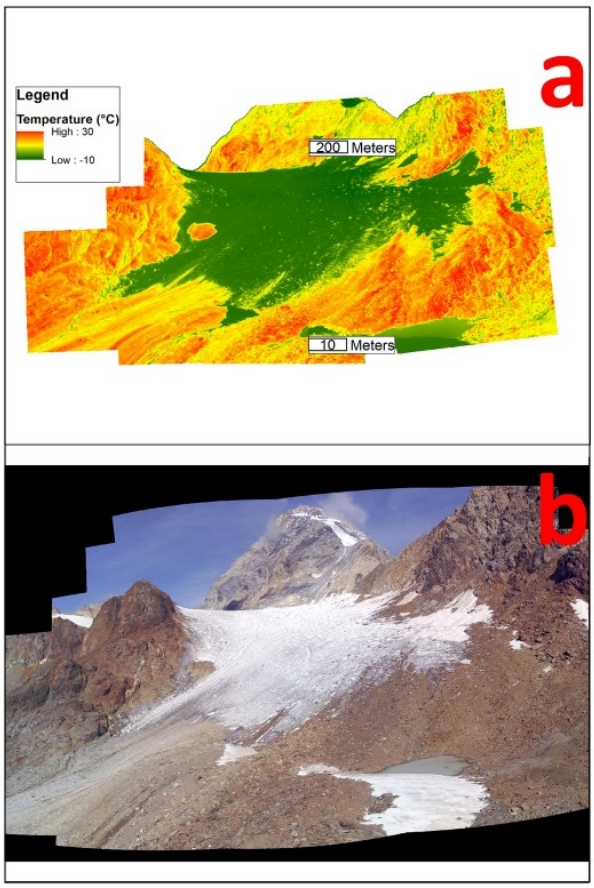

Fig. 2. Thermal (a) and visible (b) panoramic images of the eastern tongue of Gran Zebrù glacier. Images taken on 30/09/2019 at 11.18 (local time) using a FLIR E85 thermal camera.

since the distance between the camera and the object it is not a fixed value but varies between 100 and 1000 m, the air temperature changes with elevation and, the emissivity is taken from literature and not necessarily being the actual emissivity of these surfaces, therefore we investigated the effect of changing these parameters on the image calibration. To quantify the impact of these parameters on the retrieval of surface temperatures, we calculated the difference between the mean temperature of the panoramic thermal image (Fig. 2a) using the setting values and the mean temperature achieved with all the other possible values of emissivity, and the minimum and maximum value of air temperature and distance within the panoramic image.

The temperatures obtained from the thermal image were not compared to in situ temperature measurements or corrected for possible bias.

The thermal image and the corresponding visible image were georeferenced using 281 ground control points that were recognizable both on the images and on a 2019 high resolution orthophoto of the glacier (generated from a drone flight performed on 17 September 2019 using a DJI Matrice 210 RTK, for further details please see Forte et al. (2021)), and reprojected using a thin plate spline (TPS) transformation algorithm using QGIS 10.3.0, obtaining a thermal image and a visible image of the glacier with a resolution of 0.755 m.

The glacier outline was digitized manually (Paul, Kääb, Maisch, Kellenberger, and Haeberli, 2002) on the same 2019 high resolution orthophoto and a supervised maximum likelihood classification (e.g.

Jawak, Wankhede, and Luis, 2019) was performed on the georeferenced visible image in order to discriminate three surface types: ice/snow, supraglacial debris and sparse debris (mixed pixel with both debris and ice/snow, where the supraglacial debris cover is not complete) (Fig. 3). On 30 September both old snow from the previous accumulation season and fresh snow fallen in the previous days were present. Therefore, it was possible to retrieve the surface temperature distribution on the glacier and to analyse its spatial variability, in relation to the different cover types.

Debris thickness was estimated using a method similar to Mihalcea et al. (2008b), based on the empirical relationship between debris thickness and surface temperature.

Debris thickness was measured at 72 points, distancing 5 m one to another, along eight transects parallel to the glacier flow, in the sections of the glacier covered by a continuous debris cover (Fig. 4). At each point one to four measurements were performed, for a total of 163 measurements, to capture the small-scale spatial variability, excavating until reaching the ice. At the points where more than one measurement was needed, the values were averaged to obtain a mean debris thickness.

The debris thickness of 42 of these points ("training points" in Fig. 4) was used to obtain the relationship between debris thickness and debris surface temperature at the corresponding pixels of the georeferenced thermal image, while the remaining 30 points are the validation points ("validation points" in Fig. 4).

An exponential relation between the measured debris thickness and debris surface temperatures was found (Fig. 5), as reported in (1).

$$DT = 0.0218e^{0.1229DST} \quad (1)$$

where DT (m) is debris thickness and DST (°C) the debris surface temperature obtained from the thermal image.

Eq. (1) was applied to the thermal image using ArcMap 10.6 to calculate the debris thickness at each pixel with surface temperature > 0 °C.

To evaluate the results of debris thickness obtained from the thermal image, the debris thicknesses measured at the 30 validation points were compared with calculated thicknesses obtained from eq. 1.

An ASTER Surface Kinetic Temperature scene acquired on 20/09/2019 at 10.21 (GMT, corresponding to 12.21 local time) was used to compare the spatial variability of the surface temperatures with the ones obtained by the thermal camera. Moreover, the same set of debris thickness measurements used to obtain eq. (1), was used to derive the correlation equation with surface temperatures from ASTER (as in Mihalcea et al., 2008b) (Fig. 5). The exponential equation obtained (2),

$$DT = 0.0058e^{0.1952DST} \quad (2)$$

where DT (m) is debris thickness and DST (°C) the debris surface temperature obtained from the ASTER image, was applied to the pixels of the ASTER image with surface temperature > 0 °C, to calculate the debris thickness on the glacier.

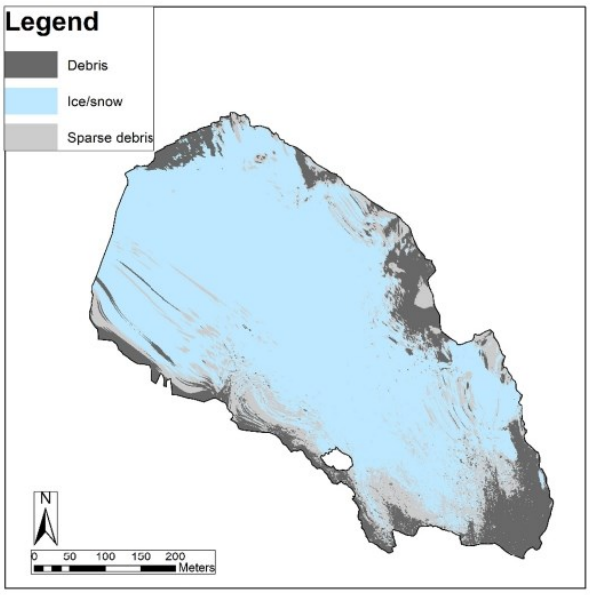

Fig. 3. Supervised classification of the Gran Zebrù glacier surface in three classes: debris, ice/snow and sparse debris.

4. Results

4.1. Image calibration

Testing the effect of setting different parameters during the thermal image calibration on the retrieved surface temperatures, we found that emissivity is the more relevant parameter, while a simplification in the air temperature and distance values impact less the results, at least in our case. Indeed, setting a temperature of 1.5 °C (estimated at 3300 m considering a standard lapse rate of 0.0065 °C/m) instead of the 2.9 °C measured at the AWS, the mean temperature of the panoramic thermal image would decrease by 0.2 °C. The effect of the distance respect the averaged distance of 550 m used in the setting, ranges between −0.2 °C in the case of the minimum distance from the glacier front and the thermal camera (100 m) and + 0.3 °C for the maximum distance to the upper part of the glacier. We calibrated the entire thermal image using the emissivity of ice (0.97), considering that this value has been considered correct also for rocks (e.g. Cardenas et al., 2014) but this simplification can introduce a higher error then the previous. Indeed, different rock types are characterized by different emissivity and even a single lithology can show a range of emissivity values, deriving from the heterogeneity of the rock surface (Mineo and Pappalardo, 2021). Different emissivity values have been used in literature for supraglacial debris, for example 0.94 (Brock et al., 2010; Kraaijenbrink et al., 2018) and 0.95 (Nicholson and Benn, 2006). The effects of these different values of emissivity is much more significant respect the influence of air temperature and of the distance from the thermal camera indeed setting an emissivity of 0.94 the mean temperature of the thermal image would increase by 0.6 °C, while an emissivity of 0.95 of 0.4 °C.

4.2. Spatial variability of surface temperature

The georeferenced thermal image mosaic of the glacier is presented in Fig. 6.

Since the temperatures from the thermal image were not compared to in situ values, it must be considered that they could suffer from a possible bias when examining absolute values.

From the thermal image it results that the glacier surface is characterized by a wide range of temperatures, covering a wide range of 33.6 °C. They range between −6.3 and 27.3 °C, with a mean of −0.5 °C and a median of −2.2 °C.

The temperature distribution of the whole glacier surface is bimodal, with a peak at negative temperatures and one at positive temperatures (Fig. 7). The peaks correspond respectively to ice/snow surfaces the first and to supraglacial debris the latter. 82% of the glacier surface (corresponding to 1.8 km^2) features temperatures lower or equal to 0 °C, while 18% (0.4 km^2) temperatures higher than 0 °C.

Considering the different surface types of coverage identified on the glacier (Fig. 3), the lowest temperatures were found on glacier ice and snow (that cover 70% of the glacier surface). Sparse debris, which covers 15% of the glacier surface, results to be 1.9 °C warmer than ice and snow on average, while the highest temperatures were found on debris,

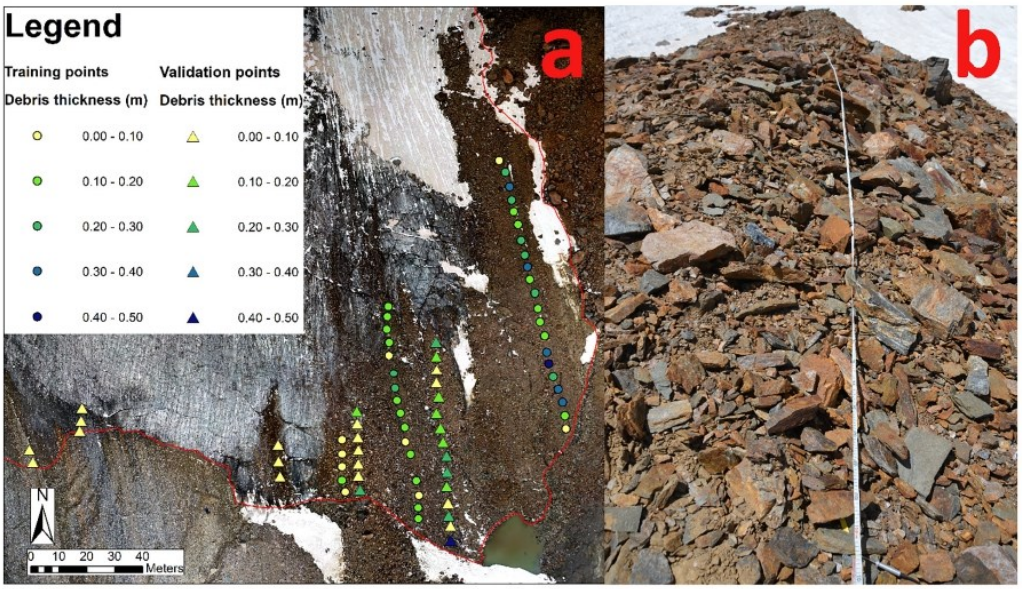

Fig. 4. a) Location and debris thickness (m) of the training points used to derive the relation between debris thickness and debris surface temperature and of the validation points. b) Example: section of the easternmost transect where debris thickness was measured.

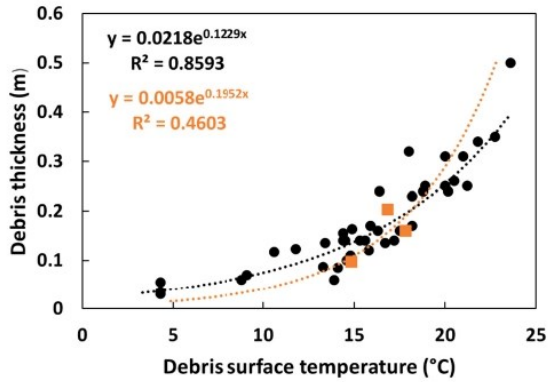

Fig. 5. Scatterplots and exponential equations correlating debris surface temperature (°C) and debris thickness (m) at each pixel. In black the debris surface temperature is retrieved from the ground-based thermal image and in orange from the ASTER image.

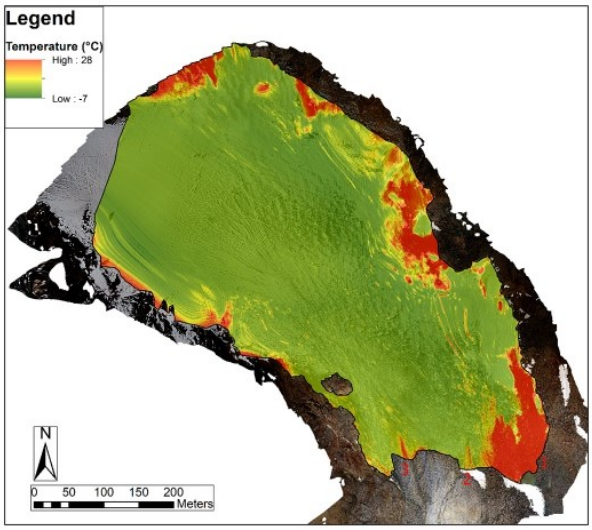

Fig. 6. Georeferenced thermal image of the glacier surface, draped over an orthoimage of the area.

covering 15% of the surface, that show temperatures warmer than ice and snow by 10.4 °C on average.

The absolute maximum temperature is found on debris, while the minimum is found on ice/snow.

The sector with the highest mean temperature is the larger debris-covered area at the eastern sector of the glacier front (area "1" in Fig. 6). The other debris-covered areas at the glacier front have lower mean temperatures: both area "2" and "3" (Fig. 6) have a mean temperature of almost 10 °C colder than "1".

The temperature difference between ice/snow surfaces and debris covered surfaces can be used to automatically segment thermal images, using the 0 °C threshold. At this scope, the thermal image should be taken during the melting season and in the central hour of the day, around peak radiation, to maximize the temperature difference. Comparing Fig. 3 and Fig. 6 it is possible to see a good correspondence between the pixels classified as complete debris on the visible image (15%) and the pixels having a temperature higher than 0 °C in the thermal image (18%). Pixels where sparse debris is present are more difficult to classify, since they contain both the signal of ice/snow and debris, and their temperature depends on the abundance of debris present. In our case the mean temperature of the areas with sparse debris was negative, but warmer than that of clean ice/snow and it is not possible to define a fixed threshold to automatically segment the sparse debris.

4.3. Debris thickness distribution derived from the thermal image

Comparing debris thickness measured at the 30 validation points

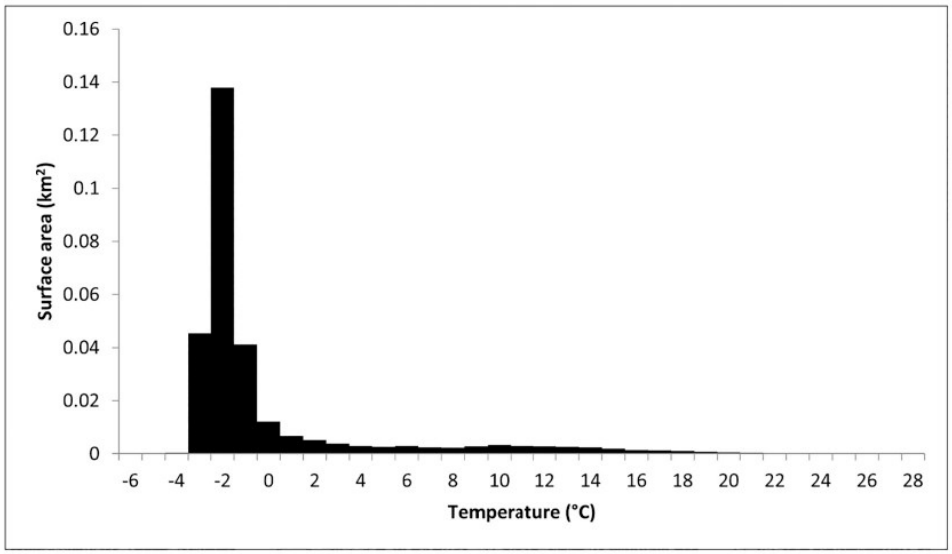

Fig. 7. Histogram of temperature (°C) distribution across the Gran Zebrù glacier surface for 1 °C intervals.

(showed in Fig. 4) and estimated debris thickness extracted at the same points, there is a good agreement between the two datasets, with a root mean squared-error (RMSE) of 0.04 m and a correlation coefficient (r) of 0.92. The mean difference between predicted and true values is 0.03 m, with a maximum underestimation of 0.14 m and a maximum overestimation of 0.05 m at the single points (Fig. 8). The differences between the measured debris thicknesses and estimated debris thicknesses are probably due to the different spatial scales: the field measurements are punctual, while a pixel covers an area of 0.57 m^2, averaging the spatial variability contained it it. The estimated thickness distribution of debris on the glacier is illustrated at Fig. 9.

It results that debris covers an area of 0.04 km^2, 18% of the glacier surface (Table 1). The calculated mean debris thickness derived from the thermal image is 0.07 m, with a minimum value of 0.02 m, a maximum of 0.62 m, and a standard deviation of 0.06 m (Table 1). Considering only the areas previously identified as completely debris-covered (Fig. 3), their mean debris thickness is 0.09 m.

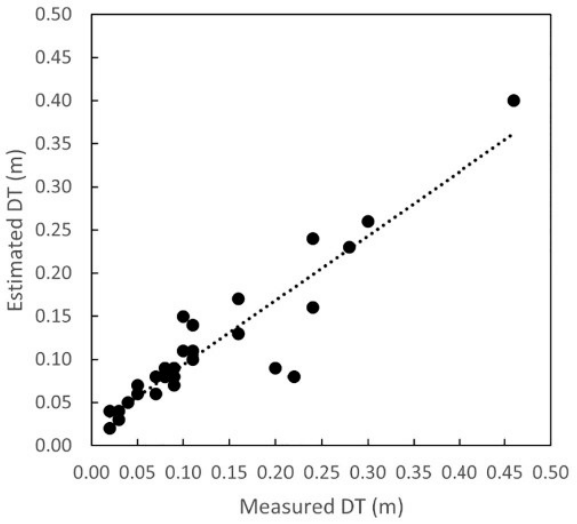

Fig. 8. Scatterplot of measured debris thicknesses (m) against estimated debris thicknesses (m) at the 30 validation points.

4.4. Comparison with ASTER data

Considering the ASTER surface kinetic temperature image acquired on 20/09/2019 at 10.21 (GMT, corresponding to 12.21 local time), the glacier area is covered by 15 entire ASTER pixels and by 27 pixels that are included only partially in the glacier area (Fig. 10a).

Comparing the spatial variability of surface temperatures from the ASTER scene (considering the fraction of the pixels inside the glacier margin) and the ground-based thermal image, the surface temperatures of the glacier area obtained from the ASTER range between −1.1 and 18.9 °C, with a range of 20.0 °C and a mean of 4.8 °C, while the surface temperatures obtained from the thermal image had a range of 33.6 °C, varying between −6.3 and 27.3 °C, with a mean of −0.5 °C. Comparing the absolute temperatures of the two images it must be considered that at the moment at which the ASTER was acquired the air temperature registered at the AWS was 8.2 °C, while the air temperature at the time of the thermal image acquisition was 2.9 °C, therefore warmer temperatures in the ASTER image are expected. The spatial pattern of the temperature distribution is similar, with higher temperatures at the glacier terminus and lower temperatures where the glacier surface is characterized by ice and snow, but it is clear that ASTER has a spatial resolution that is not able to represent the small-scale variability of the surface temperatures of a small glacier like Gran Zebrù. Due to the 90 m spatial resolution mixed pixel occur, where both the glacier and the surrounding rock walls or ice and debris are included. Moreover, also some pixels that contain mainly ice and snow surfaces, have temperatures higher than 0 °C, even if they should be at the melting point (0 °C), but not with a higher temperature. These pixels are probably contaminated by the bleeding from adjacent warmer materials (Ramachandran, Dwyer, Raup, and Kargel, 2014), namely the supraglacial debris, rock walls and periglacial debris (outside the glacier).

The estimated debris thicknesses, calculated from the ASTER image (Fig. 10b), range between 0.01 and 0.22 m, with a mean of 0.03 m, covering a surface of 169,547 m^2, representing 77% of the glacier surface. Considering only the areas previously identified as completely debris-covered (Fig. 10b), their mean debris thickness is 0.06 m. This value doesn't differ much from the 0.09 m obtained from the ground-based thermal image. However, in Fig. 10b it is observed that all

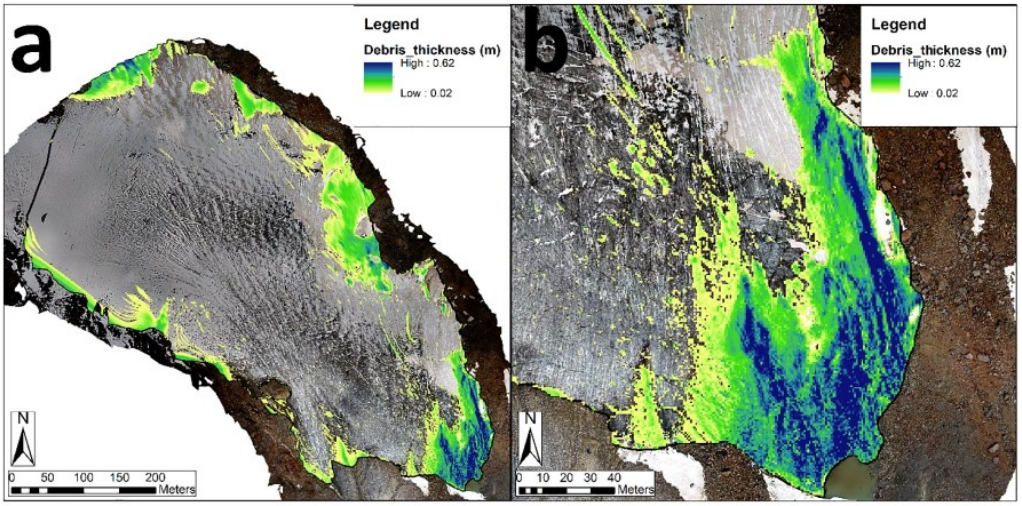

Fig. 9. Estimated debris thickness distribution at the Gran Zebrù glacier: a) entire glacier surface; b) focus on the eastern side of the glacier front, where the widest debris covered area is present.

Table 1
Statistics of the estimated debris thickness at Gran Zebrù glacier. Number of pixels, estimated area covered by debris (m2), fraction of the glacier area covered by debris (%), mean DT (debris thickness) (m), median DT (m), minimum DT (m), maximum (m) and standard deviation.

N. pixel	71,236
Area (m^2)	40,608
% area of the glacier	18
Mean (m)	0.07
Median (m)	0.05
Min (m)	0.02
Max (m)	0.62
SD	0.06

ASTER pixels where a complete debris cover is present are mixed pixels where ice and/or snow and/or the surrounding rock walls and/or periglacial debris are present, causing in the first two cases an underestimation of the surface temperatures and therefore of the debris thickness, in the last two an overestimation. The major problem from estimating the debris thickness from the ASTER is the obtained extension of the supraglacial debris, in fact, according to the ASTER, 77% of the glacier surface is covered by debris (Fig. 10b), while according to the ground-based thermal image it is the 18% (Fig. 9), resulting in an overestimation by the ASTER images of a factor of three.

Moreover, such as for temperatures, the values obtained from the ASTER image are not able to represent the small-scale variability of the debris thicknesses existing on the glacier.

5. Discussion

5.1. Spatial variability of surface temperatures

From the thermal image it resulted that the surface temperatures of

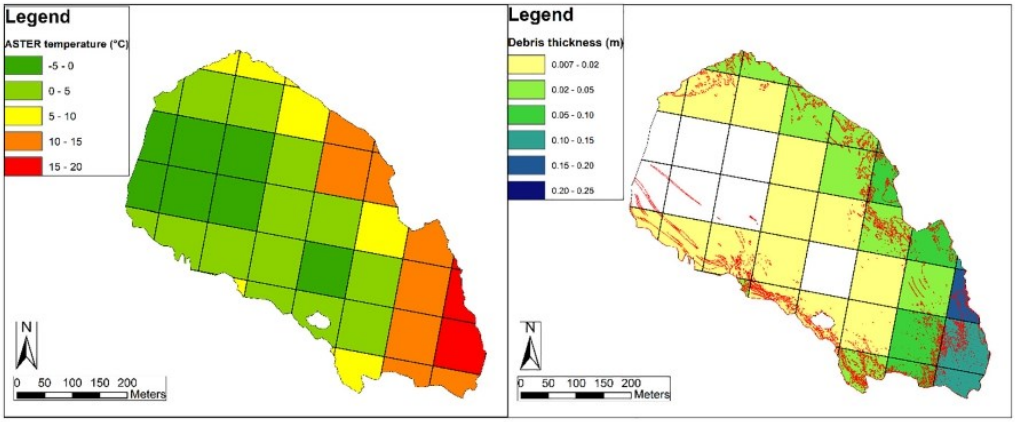

Fig. 10. a) AST08 product (surface kinetic temperature) for Gran Zebrù glacier, having a spatial resolution of 90 m, acquired on 20/09/2019 at 10.21 (GMT, 12.21 local time). b) Debris thickness (m) calculated from the ASTER surface kinetic temperature scene. The completely debris-covered areas are delineated in red (from a supervised maximum likelihood classification). (For interpretation of the references to colour in this figure legend, the reader is referred to the web version of this article.)

ice and snow at 11.18 of 30/09/2019 were negative. Despite it was a sunny day, 30 September was almost at the end of the ablation season. The surface temperatures recorded by the thermocamera on the glacier reflect the occurrence of a visible regelation/superimposed ice. The occurrence of this ice explains the below zero glacier surface temperatures that are probably due to below zero air temperatures. Indeed, the air temperature measured at the AWS at that time was positive (2.9 °C) but the AWS is placed in a rocky area in the glacier forefield and therefore it is reasonable that the values here recorded are higher than the air temperature on the glacier, even at the same altitude as already reported in other glaciers (e.g. Sicart, Hock, and Six, 2008; Reid, Carenzo, Pellicciotti, and Brock, 2012).

Consistently with the only other study that employed ground-based thermal infrared imaging to map surface temperatures on a glacier, Aubry-Wake et al. (2015), colder temperatures are found on snow and ice. The highest temperatures are found on debris, that at the investigated moment reaches up to 27.3 °C, much higher than air temperature, that was 2.9 °C. The presence of debris on a glacier causes an increase of its mean surface temperature. Among the other debris covered areas, the sectors "1" and "2" (Fig. 6) have different mean surface temperatures (with "1" being almost 10 °C warmer than "2"). They are characterized by the same lithology and elevation, so the difference in temperatures is due to the different mean debris thickness (respectively 0.03 and 0.16 m), confirming the importance of the empirical relationship between temperature and debris thickness. Differently, area "3" is located at the same elevation of the other two, but debris is composed of a different lithology (sedimentary instead of metamorphic rocks), and this affects the surface temperatures, having the same mean temperature than area "2" even if the mean measured debris thickness is higher (0.06 versus 0.03 m). Rocks having different lithologies can have different radiative and thermal properties (e.g. emissivity, albedo, heat capacity, thermal conductivity) that influence the surface temperatures. Also slope and aspect can influence surface temperatures, but in this case they are quite similar: aspect is 181 degrees at "2" and 190 degrees at "3", while slope is respectively 17 and 22 degrees.

5.2. *The use of ground-based thermal imaging to investigate glacier surface temperatures and calculate debris thickness*

We showed that for a small glacier, the use of satellite thermal data is limited by its low resolution (60–100 m) for retrieving surface temperature distribution. Also, satellite data have usually long revisit times, fixed overpass hours and can be unavailable if cloud cover conditions occur. Conversely, ground-based thermal imaging can provide a detailed high-resolution distribution of surface temperatures, with the possibility of choosing the date and time at which the investigations can be performed, with the possibility also to monitor surface temperatures at high temporal resolution, for example within the course of the day. However, the use of thermography has also some limitations. Indeed, in thermography many factors can affect the temperature measurement and it is necessary to calibrate the apparent temperatures measured by the camera, in order to obtain values as much as possible similar to the actual surface temperatures. We saw that setting the right value of emissivity is important for retrieving accurate temperatures. While for ice there is a unique value commonly used in literature and considered appropriate (0.97), different rock types are characterized by different emissivity values. Only a limited number of emissivity values experimentally estimated are available in literature, therefore an accurate estimate of the emissivity of the different would be advisable to correctly retrieve surface temperatures.

The method we proposed to estimate debris thicknesses offers multiple advantages over other methods that are commonly used to estimate debris thicknesses on glaciers. In fact, thickness measurements on glaciers are difficult to obtain. Debris thickness can be measured manually (e.g. Nakawo, Iwata, Watanabe, and Yoshida, 1986; Zhang, Fujita, Liu, Liu, and Nuimura, 2011; Reid, Carenzo, Pellicciotti, and Brock, 2012), but digging a large number of pits to the ice surface is time consuming and physically difficult, moreover it yields punctual measurements, resulting in inaccuracies from interpolating them (McCarthy, Pritchard, Willis, and King, 2017). Ground-penetrating radar (GPR) have been used to measure debris thickness, but even if it is possible to obtain high spatial resolution measurements, also carrying out GPR surveys is time consuming and challenging, moreover it is not possible to measure the thickness of thin debris (<0.1 m) (McCarthy, Pritchard, Willis, and King, 2017). Debris thickness can be retrieved from satellite data, by using the correlation between surface temperature and debris thickness (e.g. Mihalcea et al., 2008a; Mihalcea et al., 2008b; Soncini et al., 2016) or combining surface temperature estimates with energy balance models (e.g. Foster, Brock, Cutler, and Diotri, 2012; Rounce and McKinney, 2014; Schauwecker et al., 2015). The low resolution of thermal images (60–100 m) causes the "mixed pixel" effect, with different kind of surfaces present in the same pixel, while energy balance models have uncertainties related to meteorological data and debris properties (Rounce, King, McCarthy, Shean, and Salerno, 2018).

Different studies (e.g. McCarthy, Pritchard, Willis, and King, 2017; Nicholson, McCarthy, Pritchard, and Willis, 2018) showed that debris thickness varies significatively over short distances. Moreover, the supraglacial debris can cover only a fraction of the glacier surface, like in our case, or the debris can be sparse, causing the satellite pixel being mixed and not representative of the inhomogeneous conditions. The use of satellite images it is not adequate for retrieving debris thickness on small glaciers, but also for large debris-covered glaciers where debris thickness can be spatially variable, for example due to the presence of ice cliffs or supraglacial ponds. Since thin debris tends to increase glacier ablation and thicker debris tends to reduce it, it is important to have a detailed debris thickness map, to understand how it can influence the ablation on a glacier. Indeed, Nicholson, McCarthy, Pritchard, and Willis (2018) showed that in their case study, using a mean debris thickness value, instead of considering the small-scale variability can lead to an error in modelling midsummer sub-debris ablation rates, underestimating it by 11%–30%.

Our method permits to obtain high resolution and spatially distributed debris thicknesses of a small glacier, avoiding the problem of the "mixed pixel" effect. Our debris thickness map has a resolution of 0.755 m, but it is possible to reach also higher resolutions, reducing the distance at which the thermal images are captured. The method is not time consuming, as taking a thermal image of the entire glacier takes a few minutes, and a limited number of debris measurements in the field is needed. In our case the number of measurements we performed to obtain the equation was 89 (at 42 points), taking no more than a single day of field work. Moreover, the debris measurements can be performed in the more easily reachable zones of the glacier, and then debris thickness can be calculated for the entire glacier, even in the zones of the glacier that are difficult to reach. In addition, comparing debris thickness measured and estimated at 30 validation points, we calculated a small uncertainty of the results (0.03 m).

The method is probably not able to estimate debris thicknesses greater that a certain value. Mihalcea et al. (2008a) pointed out in their study that estimation of debris thickness from thermal data is not possible for debris thicker than 0.4 m, since surface temperature becomes independent of thickness. Foster, Brock, Cutler, and Diotri (2012) showed that debris surface temperature is sensitive to small variations in debris thickness between 0.0 and 0.5 m, while for debris thickness above ~0.50 m it varies more gradually. This could explain that the maximum debris thickness we obtained is 0.62 m, with only 5 values out of more than 71,000 greater than 0.5 m, while in the field we measured a maximum debris thickness of 0.70 m, in correspondence of a big boulder. Our results indicate as more probable the limit of 0.50 m. Rounce and McKinney (2014) suggested that an underrepresentation of high debris thicknesses (> 0.5 m) is not problematic for the estimation of ablation rates, as they not change much when debris is thicker than 0.5 m.

Future developments could involve the use of UAV thermal imaging, that could offer some advantages over ground-based thermal imaging. It would avoid the problem of having oblique imagery and would enable to obtain surface temperature and debris thickness maps with a resolution higher than from ground-based thermal imaging.

6. Conclusions

Ground-based thermal infrared imaging was used to investigate the spatial variability of surface temperatures on the eastern tongue of Gran Zebrù glacier and to estimate the thickness of the debris layer on the same glacier. Here we demonstrated that ground-based thermal imaging could provide a very high resolution (0.755 m) map of the surface temperature, offering a better spatial detail than what can be obtained by satellite images such as ASTER for example. Moreover, the ground-based thermal images can provide a high resolution map of the debris thickness if a certain number of field measurements are available. The improvements in the mapping of the surface temperature of the glacier and above all of its debris coverage could reduce the errors in the estimation of the glacier ablation rates. The results of the debris thickness mapping using the ground-based thermal image are in good agreement with field data, with an underestimation of the values greater than 50 cm.

Authors responsabilities

Term, Conceptualization, Methodology GT, MG; Software GT; Validation GT, MG; Formal analysis GT;

Investigation GT; Resources MG; Data Curation GT; Writing - Original Draft GT Writing - Review & Editing MG; GT; Visualization GT; Supervision MG; Project administration MG; Funding acquisition MG

Declaration of Competing Interest

The authors declare that they have no known competing financial interests or personal relationships that could have appeared to influence the work reported in this paper.

Acknowledgements

We are thankful to Stefano Ponti and Sofia Astorri for participating in the fieldwork. We also thank Stelvio National Park for logistical support. ASTER data are distributed by the NASA Land Processes Distributed Active Archive Center (LP DAAC), located at USGS/EROS, Sioux Falls, SD (http://lpdaac.usgs.gov). We want to thank you also the four anonymous reviewers that allow to improve significantly the original paper.

References

Abrams, M., Hook, S., Ramachandran, B., 2002. ASTER User Handbook. Jet Propulsion Laboratory, California Institute of Technology.

Aubry-Wake, C., Baraer, M., McKenzie, J.M., Mark, B.G., Wigmore, O., Hellström, R.Å., Lautz, L., Somers, L., 2015. Measuring glacier surface temperatures with ground-based thermal infrared imaging. Geophys. Res. Lett. 42 (20), 8489–8497. https://doi.org/10.1002/2015GL065321.

Brock, B.W., Mihalcea, C., Kirkbride, M.P., Diolaiuti, G., Cutler, M.E., Smiraglia, C., 2010. Meteorology and surface energy fluxes in the 2005–2007 ablation seasons at the Miage debris-covered glacier, Mont Blanc Massif, Italian Alps. J. Geophys. Res.-Atmos. 115 (D9) https://doi.org/10.1029/2009JD013224.

Cardenas, M.B., Doering, M., Rivas, D.S., Galdeano, C., Neilson, B.T., Robinson, C.T., 2014. Analysis of the temperature dynamics of a proglacial river using time-lapse thermal imaging and energy balance modeling. J. Hydrol. 519, 1963–1973. https://doi.org/10.1016/j.jhydrol.2014.09.079.

D'Agata, C., Bocchiola, D., Maragno, D., Smiraglia, C., Diolaiuti, G.A., 2014. Glacier shrinkage driven by climate change during half a century (1954–2007) in the Ortles-Cevedale group (Stelvio National Park, Lombardy, Italian Alps). Theor. Appl. Climatol. 116 (1–2), 169–190. https://doi.org/10.1007/s00704-013-0938-5.

Forte, E., Santin, I., Ponti, S., Colucci, R.R., Gutgesell, P., Guglielmin, M., 2021. New insights in glaciers characterization by differential diagnosis integrating GPR and remote sensing techniques: a case study for the Eastern Gran Zebrù glacier (Central Alps). Remote Sens. Environ. 267, 112715.

Foster, L.A., Brock, B.W., Cutler, M.E.J., Diotri, F., 2012. A physically based method for estimating supraglacial debris thickness from thermal band remote-sensing data. J. Glaciol. 58 (210), 677–691. https://doi.org/10.3189/2012JoG11J194.

Guerin, A., Jaboyedoff, M., Collins, B.D., Derron, M.H., Stock, G.M., Matasci, B., Podladchikov, Y.Y., 2019. Detection of rock bridges by infrared thermal imaging and modeling. Sci. Rep. 9 (1), 1–19. https://doi.org/10.1038/s41598-019-49336-1.

Haq, M.A., Jain, K., Menon, K.P., 2013. Relationship between altitude and LST derived from Landsat-TM. IEEE Int. Geosci. and Remote Sensing Symposium - IGARSS 2013, 248–250. https://doi.org/10.1109/IGARSS.2013.6721138.

Hopkinson, C., Barlow, J., Demuth, M., Pomeroy, J., 2010. Mapping changing temperature patterns over a glacial moraine using oblique thermal imagery and lidar. Can. J. Remote. Sens. 36 (sup2), S257–S265. https://doi.org/10.5589/m10-053.

Jawak, S.D., Wankhede, S.F., Luis, A.J., 2019. Explorative study on mapping surface facies of selected glaciers from Chandra Basin, Himalaya using WorldView-2 data. Remote Sens. 11 (10), 1207. https://doi.org/10.3390/rs11101207.

Kraaijenbrink, P.D., Shea, J.M., Litt, M., Steiner, J.F., Treichler, D., Koch, I., Immerzeel, W.W., 2018. Mapping surface temperatures on a debris-covered glacier with an unmanned aerial vehicle. Front. Earth Sci. 6, 64. https://doi.org/10.3389/feart.2018.00064.

Lo Vecchio, A.L., Lenzano, M.G., Durand, M., Lannutti, E., Bruce, R., Lenzano, L., 2018. Estimation of surface flow speed and ice surface temperature from optical satellite imagery at Viedma glacier, Argentina. Glob. Planet. Chang. 169, 202–213. https://doi.org/10.1016/j.gloplacha.2018.08.001.

McCarthy, M., Pritchard, H., Willis, I.A.N., King, E., 2017. Ground-penetrating radar measurements of debris thickness on Lirung Glacier, Nepal. J. Glaciol. 63 (239), 543–555. https://doi.org/10.1017/jog.2017.18.

Mihalcea, C., Brock, B.W., Diolaiuti, G., D'Agata, C., Citterio, M., Kirkbride, M.P., Cutler, M.E.J., Smiraglia, C., 2008a. Using ASTER satellite and ground-based surface temperature measurements to derive supraglacial debris cover and thickness patterns on Miage Glacier (Mont Blanc Massif, Italy). Cold Reg. Sci. Technol. 52 (3), 341–354. https://doi.org/10.1016/j.coldregions.2007.03.004.

Mihalcea, C., Mayer, C., Diolaiuti, G., D'agata, C., Smiraglia, C., Lambrecht, A., Vuillermoz, E., Tartari, G., 2008b. Spatial distribution of debris thickness and melting from remote-sensing and meteorological data, at debris-covered Baltoro glacier, Karakoram, Pakistan. Ann. Glaciol. 48, 49–57. https://doi.org/10.3189/172756408784700680.

Mineo, S., Pappalardo, G., 2021. Rock Emissivity Measurement for infrared Thermography Engineering Geological applications. Appl. Sci. 11 (9), 3773. https://doi.org/10.3390/app11093773.

Montrasio, A., Berra, F., Cariboni, M., Ceriani, M., Deichmann, N., Ferliga, C., Gregnanin, A., Guerra, S., Guglielmin, M., Jadoul, F., Longhin, M., Mair, V., Mazzoccola, D., Sciesa, E., Zappone, A., 2012. Note illustrative della Carta Geologica d'Italia alla scala 1:50000 - foglio 024 (ISPRA - Servizio Geologico d'Italia).

Nakawo, M., Rana, B., 1999. Estimate of ablation rate of glacier ice under a supraglacial debris layer. Geografiska Annal.: Series A, Phys. Geograph. 81 (4), 695–701. https://doi.org/10.1111/j.0435-3676.1999.00097.x.

Nakawo, M., Iwata, S., Watanabe, O., Yoshida, M., 1986. Processes which distribute supraglacial debris on the Khumbu Glacier, Nepal Himalaya. Ann. Glaciol. 8, 129–131. https://doi.org/10.3189/S0260305500001294.

Nicholson, L., Benn, D.I., 2006. Calculating ice melt beneath a debris layer using meteorological data. J. Glaciol. 52 (178), 463–470. https://doi.org/10.3189/172756506781828584.

Nicholson, L.I., McCarthy, M., Pritchard, H.D., Willis, I., 2018. Supraglacial debris thickness variability: impact on ablation and relation to terrain properties. Cryosphere 12, 3719–3734. https://doi.org/10.5194/tc-12-3719-2018.

Östrem, G., 1959. Ice melting under a thin layer of moraine, and the existence of ice cores in moraine ridges. Geogr. Ann. 41 (4), 228–230. https://doi.org/10.1080/20014422.1959.11907953.

Paul, F., Kääb, A., Maisch, M., Kellenberger, T., Haeberli, W., 2002. The new remote-sensing-derived Swiss glacier inventory: I. Methods. Ann. Glaciol. 34, 355–361. https://doi.org/10.3189/172756402781817941.

Porras-Amores, C., Mazarrón, F.R., Cañas, I., 2013. Using quantitative infrared thermography to determine indoor air temperature. Energ. Build. 65, 292–298. https://doi.org/10.1016/j.enbuild.2013.06.022.

Ramachandran, B., Dwyer, J., Raup, B.H., Kargel, J.S., 2014. ASTER Datasets and Derived Products for Global Glacier monitoring. In: Kargel, J., Leonard, G., Bishop, M., Kääb, A., Raup, B. (Eds.), Global Land Ice Measurements from Space. Springer, pp. 145–162. https://doi.org/10.1007/978-3-540-79818-7_6.

Reid, T.D., Carenzo, M., Pellicciotti, F., Brock, B.W., 2012. Including debris cover effects in a distributed model of glacier ablation. J. Geophys. Res.-Atmos. 117 (D18) https://doi.org/10.1029/2012JD017795.

Reznichenko, N., Davies, T., Shulmeister, J., McSaveney, M., 2010. Effects of debris on ice-surface melting rates: an experimental study. J. Glaciol. 56 (197), 384–394. https://doi.org/10.3189/002214310792447725.

Rounce, D.R., McKinney, D.C., 2014. Debris thickness of glaciers in the Everest area (Nepal Himalaya) derived from satellite imagery using a nonlinear energy balance model. Cryosphere 8, 1317–1329. https://doi.org/10.5194/tc-8-1317-2014.

Rounce, D.R., King, O., McCarthy, M., Shean, D.E., Salerno, F., 2018. Quantifying debris thickness of debris-covered glaciers in the Everest Region of Nepal through inversion of a subdebris melt model. J. Geophys. Res. Earth Surf. 123 (5), 1094–1115. https://doi.org/10.1029/2017JF004395.

Schauwecker, S., Rohrer, M., Huggel, C., Kulkarni, A., Ramanathan, A.L., Salzmann, N., Stoffel, M., Brock, B., 2015. Remotely sensed debris thickness mapping of Bara Shigri

glacier, Indian Himalaya. J. Glaciol. 61 (228), 675–688. https://doi.org/10.3189/2015JoG14J102.
Shea, C., Jamieson, B., 2011. Some fundamentals of handheld snow surface thermography. Cryosphere 5 (1), 55–66. https://doi.org/10.5194/tc-5-55-2011.
Sicart, J.E., Hock, R., Six, D., 2008. Glacier melt, air temperature, and energy balance in different climates: the Bolivian Tropics, the French Alps, and northern Sweden. J. Geophys. Res.-Atmos. 113 (D24) https://doi.org/10.1029/2008JD010406.
Soncini, A., Bocchiola, D., Confortola, G., Minora, U., Vuillermoz, E., Salerno, F., Viviano, G., Shrestha, D., Senese, A., Smiraglia, C., Diolaiuti, G., 2016. Future hydrological regimes and glacier cover in the Everest region: the case study of the upper Dudh Koshi basin. Sci. Total Environ. 565, 1084–1101. https://doi.org/10.1016/j.scitotenv.2016.05.138.
Taschner, S., Ranzi, R., 2002. Comparing the Opportunities of Landsat-TM and Aster Data for Monitoring a Debris Covered Glacier in the Italian Alps within the GLIMS Project, vol. 2. IEEE International Geoscience and Remote Sensing Symposium, Toronto, Ontario, Canada, pp. 1044–1046. https://doi.org/10.1109/IGARSS.2002.1025770.
Usamentiaga, R., Venegas, P., Guerediaga, J., Vega, L., Molleda, J., Bulnes, F.G., 2014. Infrared thermography for temperature measurement and non-destructive testing. Sensors 14 (7), 12305–12348. https://doi.org/10.3390/s140712305.
Zhang, Y., Fujita, K., Liu, S., Liu, Q., Nuimura, T., 2011. Distribution of debris thickness and its effect on ice melt at Hailuogou glacier, southeastern Tibetan Plateau, using in situ surveys and ASTER imagery. J. Glaciol. 57 (206), 1147–1157. https://doi.org/10.3189/002214311798843331.

4. Evolution of the sparse debris cover during the ablation season at two small Alpine glaciers (Gran Zebrù and Sforzellina, Ortles-Cevedale group)

Giulia Tarca[1,2] Mauro Guglielmin[1,2°]

1 Department of Theoretical and Applied Sciences, Insubria University, Varese, Via Dunant, 3, 21100 Varese, Italy

2 Climate Change Research Center, Insubria University, Via San Abbondio, Como, 22100, Italy

°Corresponding author: mauro.guglielmin@uninsubria.it

Manuscript submitted to the Journal Geomorphology.

Abstract

Despite the increase of the sparse debris on many glaciers in the world and his undoubtable impact on glacier ablation, both its evolution and its impact have been poorly investigated yet. In this study we evaluated the evolution of the sparse debris cover during the melting season at two small glaciers of the Ortles-Cevedale group (Central Italian Alps, Italy), the eastern tongue of Gran Zebrù glacier and Sforzellina glacier. We investigated the different effects of the sparse debris on albedo, on the glacier surface temperatures (using ground-based thermal imaging) and on ablation.

The supraglacial debris cover increased three times more at Sforzellina glacier, both in terms of mass and percentage debris cover, with a mean debris coverage rate of 621 g/m^2 per day and a percentage of 2.07% per day, than to Gran Zebrù glacier. As debris accumulates on the surface mainly by melt out of englacial debris, the debris coverage rates depend both on the ablation and on the englacial debris concentration, which was found to be higher at Sforzellina glacier (mean 10810 g/m^3) respect to Gran Zebrù glacier (mean 6131 g/m^3).

Debris is mainly composed by clasts coarser than 25 mm at both glaciers (on average 91% at Gran Zebrù and 89% at Sforzellina), with subangular sedimentary rocks prevailing at Gran Zebrù and angular metamorphic rocks at Sforzellina glacier, suggesting a debris supply from the rockwalls surrounding the glaciers, with a longer englacial transport at Gran Zebrù.

Albedo decreases at increasing percentage of debris covering the surface, linearly at Sforzellina and logarithmically at Gran Zebrù while surface temperatures are positively correlated with the mass of debris present on the glacier surface. The influence of the percentage of debris on the mean ablation rate is explained by a quadratic function, with the ablation rate increasing at increasing debris cover for moderate debris covers, due to the

decreasing albedo, and decreasing ablation rates with high percentages of debris cover (>80%), due to the insulation effect of clasts.

Keywords: glaciers, supraglacial debris, sparse debris cover, albedo, surface temperature, ablation

1. Introduction

It is known that the presence of supraglacial debris influences glacier ablation. Østrem (1959) found higher ablation rates under thin debris (less than the 'critical thickness') compared to clean ice and decreasing ablation rates under thicker debris covers. The critical thickness is defined as the thickness at which the ablation rate for debris covered ice and debris free ice are equal (e.g. Mattson, 1993). A range of critical thicknesses have been measured on different glaciers in the world, with values between 15 mm and 115 mm, decreasing at increasing latitude and elevation, but possibly also influenced by other factors and processes (e.g. meteorological conditions, debris lithology, etc.) (Reznichenko et al., 2010). Other studies showed that a thin debris layer does not enhance glacier melt compared to clean ice, for example in New Zealand (Brook et al., 2013; Hagg et al., 2014) and in the Karakoram (Muhammad et al., 2020). The evolution of the continuous debris cover extent on glaciers has been studied worldwide, showing a general expansion in the Alps (Kellerer-Pirklbauer, 2008; Azzoni et al., 2018; Mölg et al., 2019), Karakoram (Xie et al., 2020), Himalayas (Bolch et al., 2008; Jiang et al., 2018), Caucasus (Stokes et al., 2007) and Patagonia (Glasser et al., 2016). Differently, the temporal evolution of the sparse debris cover on glaciers has been poorly analysed, with only few studies investigating it in detail (e.g. Kirkbride and Deline, 2013; Azzoni

et al., 2016; Fyffe et al., 2020). In particular, Fyffe et al. (2020) reported that at moderate percentage debris covers (c. 30–80%), ablation has similar values and is enhanced (+3.7%) compared to clean ice (with 0-15 % of debris), while when the debris becomes complete, there is a very abrupt decrease in ablation (by 61.6% compared to a partial debris cover). Therefore, especially in a climate change framework the effect of dirty ice (glacier ice with sparse debris cover) on the ablation rate appears as a gap of knowledge to fill.

The aim of this work is: a) to understand the evolution of the sparse debris cover during the melting season, b) to calculate the englacial debris concentration; c) to determine the debris sources; d) to investigate the effect of the sparse debris on albedo, on the glacier surface temperatures (using ground-based thermal imaging) and on ablation in different glacier conditions.

To achieve these goals we chose two different glaciers of the same mountain group (Ortles-Cevedale, Central Italian Alps, Italy), the eastern tongue of Gran Zebrù glacier and Sforzellina glacier, having a similar surface area but different characteristics: different aspect, different elevation, different length and different bedrock lithologies.

2. **Study areas**

The research was performed at Gran Zebrù glacier and Sforzellina glacier, both situated in the Ortles-Cevedale group (Central Italian Alps, Italy) and about 14 km far from each other (Fig. 1). The Ortles-Cevedale group is the largest glacierized mountain group of the Italian Alps and is undergoing rapid glacier shrinkage. An area reduction of about 40% was reported by D'Agata et al. (2014) for the period 1954-2007, while Carturan et al. (2013) reported a reduction of 23% for the period 1987-2009, with an average geodetic mass budget rate of −0.69 ± 0.12 m w.e. a^{-1}. The area is characterized by a continental Alpine climate (Soncini et al., 2017). Annual

precipitation is about 850 mm (40% falling from June to August) and the mean annual temperature is 3.3 °C (1980-2010) at Forni (about 2190 m a.s.l.) (Leonelli et al., 2017). At the Bormio weather station (1225 m a.s.l., ARPA Lombardia), situated respectively 16 km and 17 km far from Gran Zebrù and Sforzellina glaciers, a temperature increase of 0.012 °C y^{-1} was measured between 1924 and 2007, with an increased trend in the period 1981-2007 (0.038 °C y^{-1}), while total precipitation did not seem to substantially change between 1926 and 2003 (Salerno et al., 2014).

Two small glaciers (covering an area < 1 km^2) were chosen, as small glaciers account for more than 90% of the total number of glaciers in Italy (Diolaiuti et al., 2019). The glaciers have similar surface area but different aspect, elevation, length, supraglacial debris cover and bedrock lithologies.

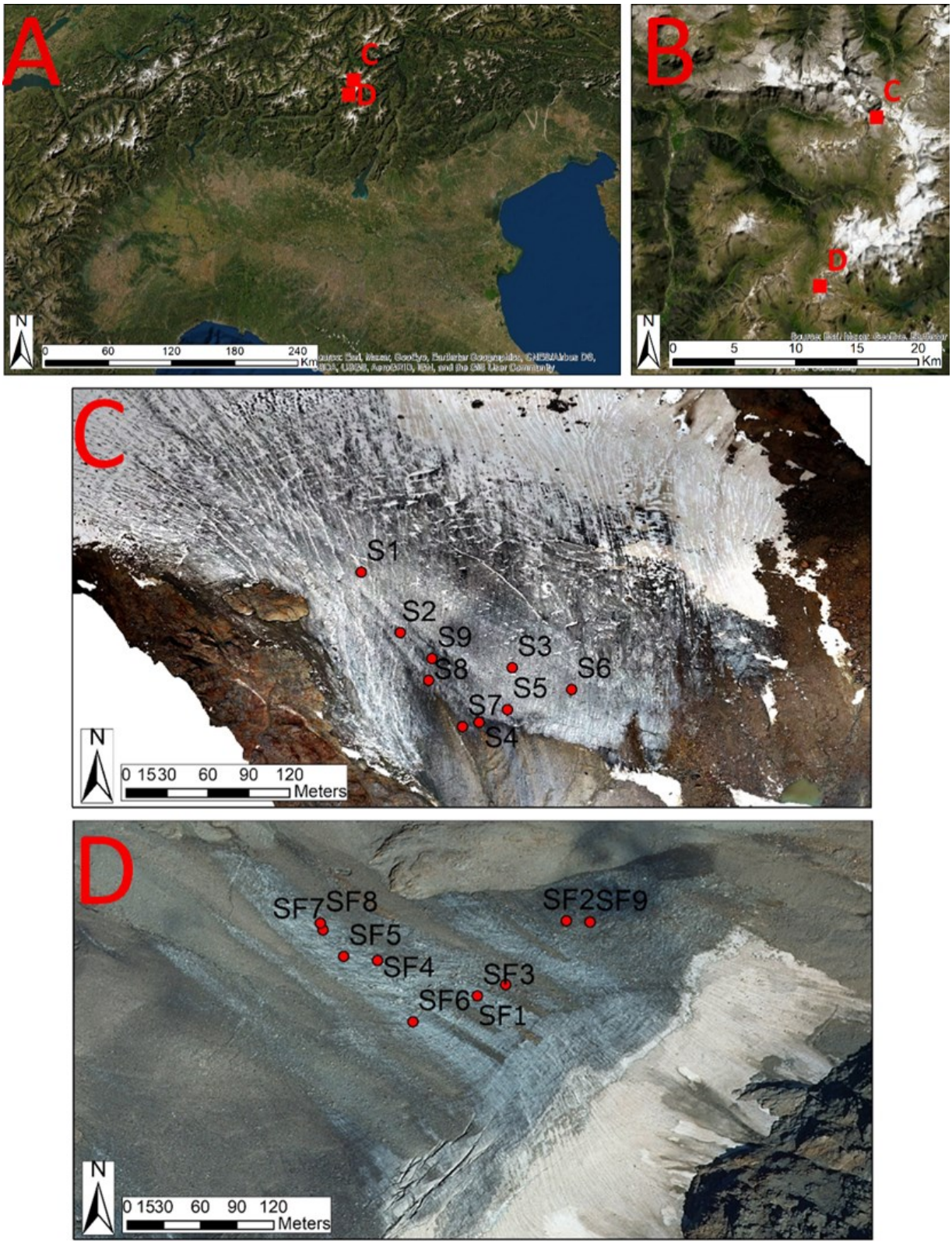

Figure 1 A) and B) Location of of Gran Zebrù glacier (C) and Sforzellina glacier (D) in the Alps; C) position of the 9 quadrats selected on the Gran Zebrù glacier ablation area; D) position of the 9 quadrats selected on the Sforzellina glacier ablation area. Basemap of A and B is Esri World Imagery. Basemap of C is an UAV orthophoto from 2019, basemap of D is orthophoto AGEA 2015 (from Geoportale Regione Lombardia).

Gran Zebrù glacier is located in Cedec Valley (Fig. 1A) and has an area of 0.58 km^2 (surveyed in 2016) (Paul et al., 2019). We worked on the eastern tongue of the glacier, that covers about 0.22 km^2. The glacier front is located at about 3080 m a.s.l. and has a south-east aspect.

Sforzellina glacier is located in Gavia Valley (Fig. 1A) and covers a surface of 0.22 km^2 (surveyed in 2016) (Paul et al., 2019). The glacier front is located at about 2850 m a.s.l. and has a north-west aspect.

Most of the glacier surface of Sforzellina glacier is covered by supraglacial debris (66.8% in 2012), while the debris-covered area at Gran Zebrù glacier is lower (30.1% in 2012) (Azzoni et al., 2018). Considering the eastern tongue of Gran Zebrù glacier, where this work was carried out, the debris covered area is even smaller, representing 15% of the glacier surface (Tarca and Guglielmin, 2022).

Regarding the bedrock, Gran Zebrù glacier is located in an area crossed by the tectonic Zebrù line, that divides the Campo Nappe (south) and the Ortler Nappe (north), the first composed mainly of micaschist and paragneiss, the second of dolomite and limestone (Montrasio et al., 2012). While Sforzellina glacier is entirely located in the Campo Nappe and therefore characterized by micaschist, paragneiss and orthogneiss.

3. Methods

3.1. Meteorological data

Daily mean temperatures and daily precipitation data from the Valfurva S. Caterina weather station (ARPA Lombardia - Servizio Meteorologico Regionale) between July and September of 2019 and 2020 were analysed. The weather station is located at 1730 m a.s.l. and at a distance of about 9 km from Gran Zebrù glacier and about 8 km from Sforzellina glacier. Global radiation data were obtained from Valdisotto Oga S. Colombano weather station (ARPA

Lombardia - Servizio Meteorologico Regionale), located at 2300 m a.s.l and about 21 km from Gran Zebrù glacier and about 20 km from Sforzellina glacier.

3.2. Field work

The research started at both glaciers as soon as the ice was exposed at the glacier front. At Gran Zebrù the research started on 10/08/2019 because a few days earlier only in one sector of the glacier, while most of the glacier was still covered by snow as showed in Fig. 2a (taken on 09/08/2019). At Sforzellina it started on 30/07/2020, with similar conditions (Fig.2b).

Figure 2 A) Photograph of the eastern tongue of Gran Zebrù glacier taken on 09/08/2019; B) Photograph of Sforzellina glacier taken on 30/07/2020.

To study the temporal evolution of the sparse debris cover on the glaciers we used a modified version of the method applied by Azzoni et al. (2016). We selected 1 m x 1 m sampling areas on the glacier surface (Fig. 1), with different amounts of debris. We chose to evaluate the debris evolution at 9 sites at each glacier (more than in Azzoni et al., 2016), to have a more robust statistic sample. At each site we acquired a digital image of the surface using a digital camera. We used a pyranometer to measure incoming and outgoing short-wave radiation at each site, to calculate albedo. The radiation data were acquired every 10 seconds and at least 3 measurements at each site were obtained. Then, to study the temporal evolution of debris, at least 2 cm of the glacier surface were removed, and the ice and debris were collected. The operation was repeated after about one month in the same quadrats, to calculate the debris coverage rate. The sampling areas are coded from S1 to S9 at Gran Zebrù and from SF1 to SF9 at Sforzellina. The suffix "A" refers to the beginning of the study period, "B" to the end.

In addition to the method proposed by Azzoni et al. (2016), we used a FLIR e85 thermal camera to take one to four thermal images to cover the surface of each quadrat, at the beginning and at the end of the study period. The thermal camera used has a spectral range of 7.5 - 14.0 µm, an IR Resolution of 384 x 288 (110,592 pixels) and an accuracy of ±2°K.

To identify the exact location of the quadrats, an ablation stake was drilled at one corner of each quadrat. At quadrats S2 and SF5 the ablation stakes used to identify the exact location were lost between the two measurements and therefore the work was completed at only 8 quadrats at each glacier. Due to logistical issues, we were able to measure the ablation occurred during the entire study periods only at 3 stakes at Gran Zebrù and 4 stakes at Sforzellina glacier. Moreover, we obtained continuous ablation measurements at all the stakes at Sforzellina glacier for the period 30/07/2020 to 26/08/2020, that we will use as an example.

3.3. Samples analyses

The samples composed by ice and debris collected from the quadrats were melted. The samples were sieved through 25 and 2 mm to separate the coarser and the sand fractions of debris that were than weighed. The remaining part of the samples was filtered using filter paper (17-30 µm) to separate meltwater from fine debris. Debris retained by the filter was dried and the particle size distribution was performed by sieving it, using a mechanical sieve shaker (Gregorich and Carter, 2007).

In addition, we selected 10 random coarse clasts (>25 mm) for each sample to reconstruct the transport history of debris, evaluating the clasts roundness (degree of curvature of clast edges), classifying them as angular, sub-angular, sub-rounded or rounded (Benn and Ballantyne, 1994). Moreover, the lithology of each clast was determined visually. In case of stratified sedimentary rocks, 5% HCl was used to discriminate limestone from dolomite.

3.4. Image analyses

The photographs acquired for each sampling area were classified using the software imageJ (Schneider et al., 2012; Schindelin et al., 2015), in particular we used the Fiji distribution of ImageJ (Schindelin et al., 2012), to calculate the percentage of debris covering each area. Initially, the method proposed by Azzoni et al. (2016) for image classification was applied, using a threshold iteratively. Figure 3B shows that in our case the method works well for fine debris, that is correctly classified, but it is not able to classify coarser rock fragments that have light colours (e.g. limestones-dolostones). Therefore, we tested the Trainable Weka Segmentation (Arganda-Carreras et al., 2017) Fiji plugin, a machine learning tool that can be used to produce pixel-based segmentations (Fig. 3C).

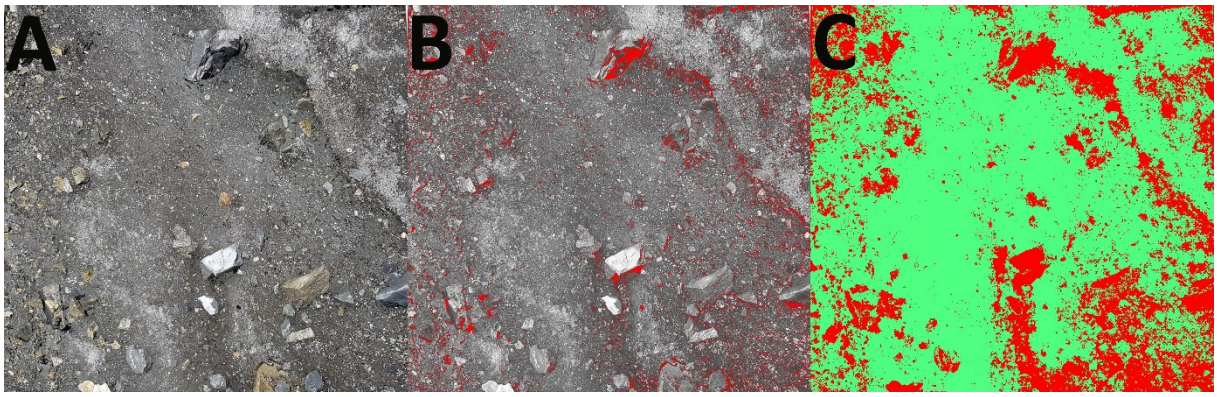

Figure 3 *Example of classification of a quadrat with coarse debris: A) Original frame (S4A); B) Classification of debris selecting a threshold (red should represent debris); C) Segmented image using machine learning (red represents debris pixels, green represents ice pixels).*

Image segmentation is achieved using the FastRandomForest algorithm, a version of random forest, a supervised learning algorithm that uses an ensemble of decision trees for classification. The classifier needs to be trained by drawing regions of interest (ROI) for each class. To evaluate the accuracy of the two classifications, 30 random points were selected on four of the images that were classified using both methods.

The overall accuracy was calculated as the ratio between the number of correctly classified points and the total number of points. The accuracy of the threshold method resulted to be 85% on average, while the machine learning method reached the 94%. Therefore, we chose to classify all the other images using the machine learning method (Fig. 3C).

The thermal images of each quadrat were analysed using the FLIR Tools+ Software to obtain the mean, maximum and minimum temperature of the glacier surface.

3.5 Data analyses

To understand the evolution of debris, we calculated the debris coverage rate as the ratio between the mass of debris accumulated at the glacier surface and the time frame (g m^{-2} per day) (Azzoni et al., 2016).

We also calculated the debris coverage rate in terms of changes in percentage of debris (% per day).

We calculated the englacial debris concentration (g/m^3) as the ratio between the mass of debris accumulated at the glacier surface during the study period and the volume of ice that melted in the same period (Kirkbride and Deline, 2013). The ice melted was measured at the ablation stakes

4. Results

4.1 Meteorological data

The two years (2019 and 2020) experienced similar mean temperatures during the study periods: the mean temperature between July and September was 12.2 °C in 2019 and 12.1 °C in 2020. The thawing degree-days (TDD) were respectively 1123 and 1120 during these three months in 2019 and 2020. In the same period 53 days of precipitation occurred in 2019 and 48 days in 2020, of which respectively 10 and 11 days with precipitation >10 mm/day. The mean global radiation at Valdisotto Oga S. Colombano was 206 W/m^2 between July and September 2019 and 207 W/m^2 in 2020.

Since the meteorological conditions were similar during the two ablation seasons 2019 and 2020, we can reasonably compare the results of the two experiments although they were carried out during two different years.

4.2 Debris coverage and debris mass

At Gran Zebrù glacier the percentage of debris retrieved from the images ranged between 9.6 and 69.8 % in the different quadrats at the beginning of the study period, with a mean of 33.7

while and at the end of the study period for all of the quadrats, except one (S4), the percentage was lower than at the beginning, ranging between 2.7 and 43.4, with a mean of 18.7 % (Fig. 4A, Table A.1).

At Sforzellina glacier, the debris percentage at the beginning was higher than at Gran Zebrù ranging between 17.4 and 77.2 %, with a mean of 52.6 %, with an increase at every quadrat, reaching values between 18.7 and 97.3 % with a mean of 67.9 % at the end of the study period (Fig. 4B, Table A.1).

The mass of debris samples collected on Gran Zebrù glacier was between 668 and 15610 g at the beginning, and between 160 and 16224 g at the end of the study period (Fig. 4C, Table A.1). The total mean mass at Gran Zebrù resulted 6350 g. At Sforzellina glacier the mass ranged from 1132 to 29334 g at the beginning and from 3337 to 47074 g at the end (Fig. 4D, Table A.1) and with a total mean mass of 17977 g.

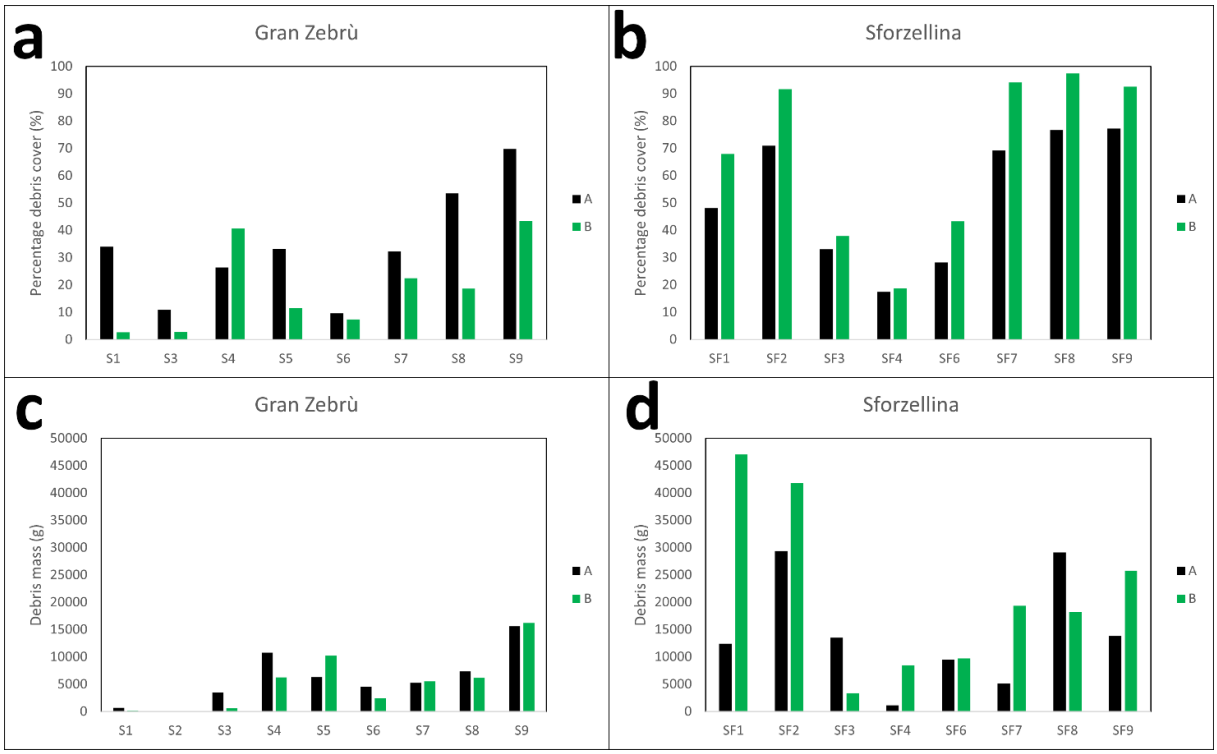

Figure 4 Percentage of debris covering the quadrats at the beginning (A) and at the end of the study period (B) at Gran Zebrù glacier (a) and Sforzellina glacier (b). Mass of debris collected at the quadrats at the beginning (A) and at the end of the study period (B) at Gran Zebrù glacier (c) and Sforzellina glacier (d).

4.3 Debris coverage rate

Gran Zebrù glacier showed a mean debris coverage rate of 211 g/m^2 per day, while Sforzellina glacier revealed an almost triple rate with a mean value of 621 g/m^2(Table 1).

Considering the single quadrats at both glacier the debris coverage rate didn't show any appreciable spatial pattern (Fig. 5).

The mean debris coverage rates in terms of percentage were respectively 0.64 and 2.07 % per day for the two glaciers (Table 1).

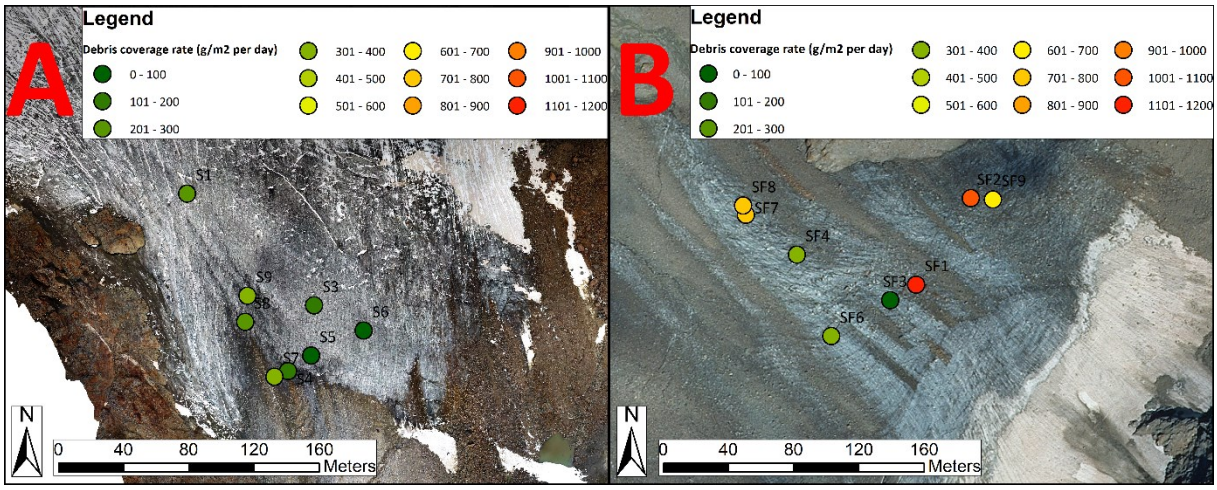

Figure 5 Debris coverage rate (g/m^2 per day) at Gran Zebrù glacier (A) and Sforzellina glacier (B).

Table 1 Debris coverage rate in terms of percentage (% per day) and mass (g/m^2 per day) at the 16 quadrats at Gran Zebrù glacier and Sforzellina glacier, with mean and standard deviation (SD) values.

Sample	Rate (%/day)	Rate (g/m^2 day)	Sample	Rate (%/day)	Rate (g /m^2 day)
S1	0.07	209	SF1	1.66	1148
S3	0.08	122	SF2	2.24	1020
S4	1.10	199	SF3	0.92	81
S5	0.42	6	SF4	0.69	313
S6	0.29	23	SF6	1.60	360
S7	0.87	393	SF7	3.48	717
S8	0.69	203	SF8	3.74	701
S9	1.61	601	SF9	2.26	629
Mean	0.64	211	Mean	2.07	621
SD	0.54	197	SD	1.10	360

4.3 Debris characteristics and composition

4.3.1 Granulometry

From the grain size distribution resulted that most of debris was composed of gravel (>2 mm) (granules, pebbles, cobbles and boulders), composing between 96.56 and 99.93 % of the samples at Gran Zebrù and between 98.07 and 99.99 % at Sforzellina (Table 2). If we consider the fraction >25 mm it represented between the 74.58% and 98.57% at Gran Zebrù and between 69.81 and 98.57% at Sforzellina. Sand represented between the 0.06 and 3.01 % at Gran Zebrù and between the 0.01 and 1.77 % at Sforzellina. The finest fraction, composed of clay and silt, represented the smallest fraction of the debris samples, having values from 0.02 to 0.58 % at Gran Zebrù and from 0.001 to 0.15 % at Sforzellina (Table 2).

Table 2 Characteristics and composition of the debris samples at Gran Zebrù and Sforzellina glaciers. Mass of the debris samples and percentage of clay and silt, sand and gravel (after Wentworth, 1922). Also, minimum, maximum, total mean values, mean values at the beginning of the study period (A) and at the end (B) are reported.

Sample	Mass (g)	Clay & Silt (%)	Sand (%)	Gravel (%)
S1A	668	0.58	3.01	96.65
S3A	3498	0.02	0.11	99.87
S4A	10778	0.02	0.06	99.93
S5A	6278	0.07	0.28	99.65
S6A	4529	0.02	0.13	99.84
S7A	5287	0.08	0.28	99.65
S8A	7361	0.27	0.67	99.06
S9A	15610	0.02	0.10	99.79
S1B	160	0.50	2.75	96.56
S3B	602	0.10	0.71	99.12
S4B	6238	0.04	0.18	99.77
S5B	10208	0.03	0.14	99.82
S6B	2467	0.09	0.99	98.92
S7B	5492	0.03	0.23	99.73
S8B	6203	0.17	0.65	99.17
S9B	16224	0.02	0.11	99.86
Min	160	0.02	0.06	96.56
Max	16224	0.58	3.01	99.93
Mean	6350	0.13	0.65	99.21
Mean A	6751	0.14	0.58	99.30
Mean B	5949	0.12	0.72	99.12
SF1A	12395	0.01	0.03	99.96
SF2A	29334	0.00	0.01	99.99
SF3A	13501	0.00	0.01	99.99
SF4A	1132	0.15	1.77	98.07
SF6A	9491	0.01	0.42	99.57
SF7A	5116	0.04	0.08	99.89
SF8A	29079	0.01	0.05	99.93
SF9A	13814	0.03	0.94	99.03
SF1B	47074	0.00	0.15	99.84
SF2B	41816	0.00	0.03	99.97
SF3B	3337	0.01	0.19	99.80
SF4B	8451	0.01	0.06	99.93
SF6B	9723	0.01	0.18	99.81
SF7B	19367	0.06	0.21	99.73
SF8B	18223	0.04	0.09	99.87
SF9B	25781	0.02	0.24	99.74
Min	1132	0.00	0.01	98.07
Max	47074	0.15	1.77	99.99
Mean	17977	0.02	0.28	99.70
Mean A	14233	0.03	0.41	99.55
Mean B	21721	0.02	0.14	99.84

4.3.2 Lithology and roundness

The coarser fraction (> 25 mm) of debris, representing 91% percent on average, on Gran Zebrù glacier was composed almost only of sedimentary rocks, namely dolomite (68%) and limestone (31%), with a small percentage (1%) of prasinite. On the other side, on Sforzellina glacier, only metamorphic rocks occurred with prevailing paragneiss (62%) and orthogneiss (35%), while marble was only a small fraction (3%).

Clasts collected at Gran Zebrù glacier were mostly subangular (65%), but debris was also formed by subrounded (27%) and angular clasts (8%). Differently at Sforzellina glacier a major part of the clast were angular (75%), with a smaller fraction of subangular (25%), but no subrounded or rounded clast were found. We didn't find any striated or flatiron rocks, at both sites.

4.4 Albedo

The albedo measured at each quadrat ranged between 0.08 and 0.31 at Gran Zebrù (S1A not available), with an average of 0.14 at the beginning of the study period and of 0.18 at the end. Considering the single quadrats, albedo increased always at the end of the study period, except at S8 where it was the same (Fig. 6, Table A.1).

At Sforzellina albedo ranged between 0.07 and 0.21, being 0.13 at the beginning and 0.12 at the end of the study period. Regarding the single quadrats, at two of them there was an increase (SF1 and SF4), at two it was the same (SF2 and SF3), and at four of them (from SF6 to SF9) it decreased (Fig. 6, Table A.1).

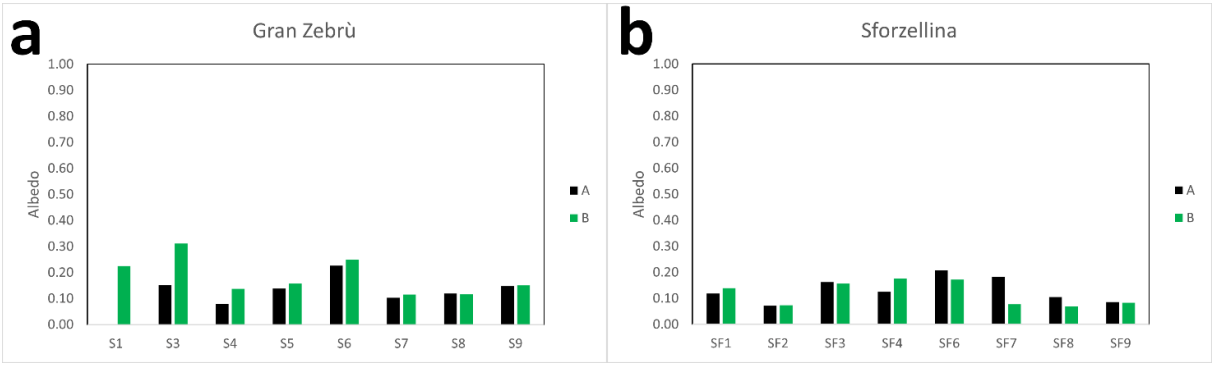

Figure 6 Albedo values measured at the Gran Zebrù (a) and Sforzellina (b) quadrats at the beginning (A) and at the end of the study period (B).

4.5 Surface temperatures

At Gran Zebrù the mean surface temperature of the different quadrats ranged between -1.0 and 1.4 °C, with an average of -0.2 °C (Table 3). At the end of the study period the overall mean surface temperature was slightly colder than at the beginning of the study period (-0.3 °C against -0.1 °C). The maximum temperature measured was 10.9 °C (at S8B) and the minimum -4.0 °C (at S9B).

On the other hand, at Sforzellina glacier the mean surface temperature of the different quadrats ranged between -1.7 and 3.8 °C, with an average of 0.9 °C (Table 3). The overall mean temperature increased from 0.0 °C to 1.7 °C. The maximum temperature measured was 20.1 °C (at SF7B), almost double than at Gran Zebrù while the minimum is similar (Table 3).

Table 3 Maximum, minimum and mean surface temperature (°C) of the glacier surface in the different quadrats and for comparison air temperature (°C) measured in the same quadrats.

Quadrat	Max T (°C)	Min T (°C)	Mean T (°C)	Air T (°C)
S1A	1.4	-1.3	-1.0	13.0
S3A	5.9	-2.2	-0.2	15.0
S4A	8.4	0.0	1.4	15.0
S5A	6.3	-1.7	-0.4	9.0
S6A	6.0	-2.2	-0.5	14.0
S7A	7.5	-2.0	-0.4	14.0
S8A	2.3	-1.8	-0.7	14.0
S9A	9.2	-2.0	0.3	14.0
S1B	3.3	-2.5	0.2	12.0
S3B	4.4	-1.1	-0.1	13.0
S4B	4.7	-1.8	-0.6	13.0
S5B	7.7	-1.5	0.2	12.0
S6B	4.6	-2.5	-0.9	13.0
S7B	4.5	-2.4	-0.6	13.0
S8B	10.9	-1.7	0.3	12.0
S9B	10.1	-4.0	-0.9	12.0
SF1A	8.2	-3.3	0.0	14.0
SF3A	8.7	-2.5	-0.4	14.0
SF4A	2.7	-4.0	-1.7	18.0
SF6A	14.6	-2.0	0.6	18.0
SF7A	8.2	-2.0	-0.4	18.0
SF8A	16.5	-3.1	1.8	14.0
SF9A	NA	NA	NA	NA
SF1B	9.3	0.8	2.8	6.0
SF2B	9.4	0.3	3.8	6.0
SF3B	7.5	-0.5	0.0	6.0
SF4B	8.8	0.0	0.9	9.0
SF6B	8.6	-0.3	1.0	9.0
SF7B	20.1	-4.6	0.7	9.0
SF8B	12.0	-1.5	1.5	9.0
SF9B	8.8	0.5	2.6	6.0

4.6 Ablation and englacial debris concentration

Unfortunately, we obtained ablation measurements for the entire period of the study periods only at 3 stakes at Gran Zebrù and at 4 stakes at Sforzellina respectively (Table 4). At Gran Zebrù glacier the measured ablation rate ranged between 28 and 31 mm water equivalent

(w.e.) per day, with a mean of 30, while at Sforzellina it ranged between 41 and 48 mm w.e. per day, with a mean value of 43 (Table 4), the 32% higher than at Gran Zebrù.

Table 4 Total ablation during the study period (cm), duration of the study period (days), ablation rate (mm w.e. per day), concentration of englacial debris (g/m^3), also mean values and standard deviation for each glacier are reported. GZ stands for Gran Zebrù, SF for Sforzellina.

Quadrat	Ablation (cm)	Days	Ablation rate (mm w.e. per day)	Englacial debris concentration (g/m^3)
S1	135	39	31	119
S5	93	28	30	10976
S8	85	27	28	7297
Mean (GZ)	104		30	6131
SD	27		1	5522
SF4	122	27	41	6927
SF6	145	27	48	6706
SF7	126	27	42	15370
SF8	128	27	43	14237
Mean (SF)	130		43	10810
SD	10		3	4635

Knowing the melt that occurred during the study period it was possible to calculate the quantity of debris present in the ice, reported as englacial debris concentration (g/m^3). We obtained englacial debris concentrations between 119 and 10976 g/m^3 at Gran Zebrù and 6706 and 15370 g/m^3 at Sforzellina (Table 4, Figure 7). At Sforzellina the mean debris

concentration was almost double than at Gran Zebrù (respectively 10810 and 6131 g/m^3) (Table 4, Figure 7).

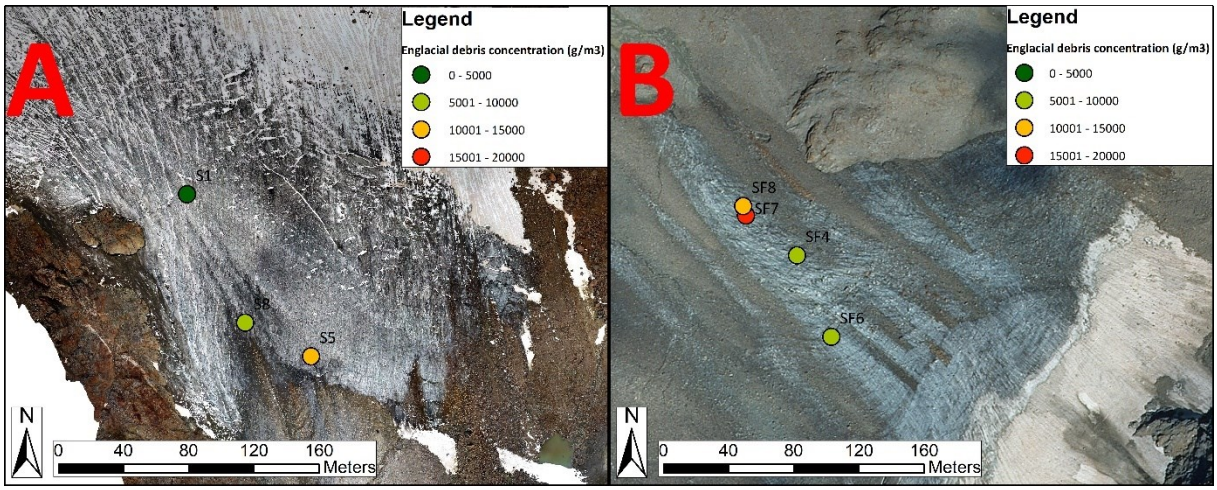

Figure 7 Englacial debris concentrations (g/m^3) at Gran Zebrù glacier (A) and Sforzellina glacier (B).

Considering the distance of each quadrat from the glacier front, we can see that debris concentration tends to increase towards the glacier front at both glaciers (Fig. 7). A negative linear correlation was found between the distance from the glacier front (m) and the englacial debris concentration (g/m^3) at both glaciers (Fig. 8).

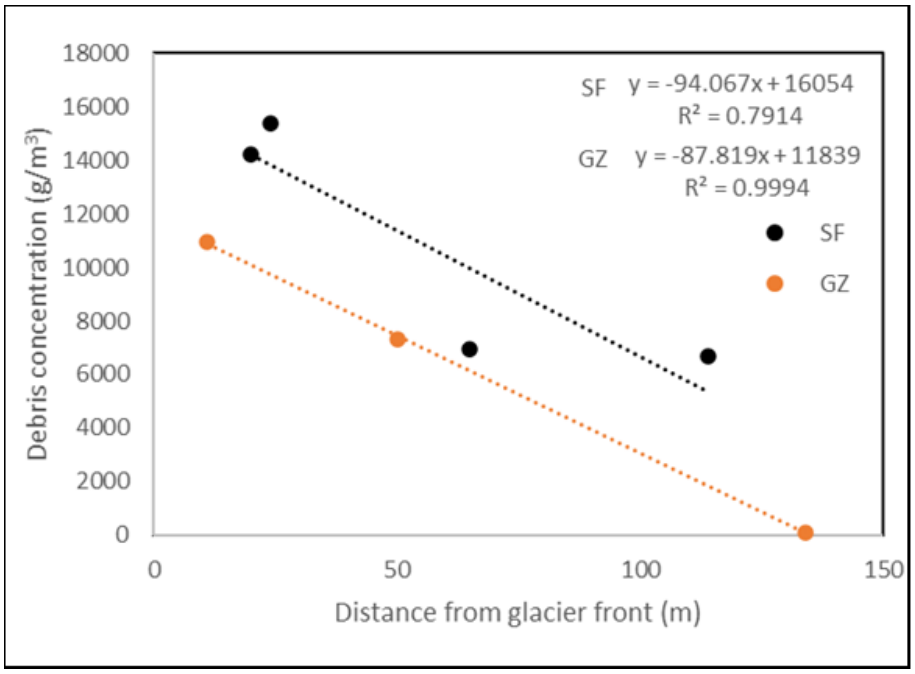

Figure 8 Scatterplot of distance from the glacier front (m) and englacial debris concentration (g/m³) at Gran Zebrù (GZ) (orange) and Sforzellina (SF) glacier (black). In the equations y is debris concentration (g/m³) and x the distance from the glacier front (m).

4.7 The effect of debris on albedo and on the surface temperature

We found a significant negative linear correlation between albedo and the percentage of debris measured at Sforzellina glacier (R=-0.76, p=0.0006) (Fig. 9). Differently, for Gran Zebrù glacier the correlation between the two variables can't be explained by a linear regression but it is best represented by a logarithmic function (R=-0.79, p=0.0005) (Fig.9). Considering only values lower than 30% of debris, there is a linear negative correlation with albedo, while at increasing debris percentage above 30%, the albedo doesn't decrease linearly anymore, probably because it approaches the albedo of the rock.

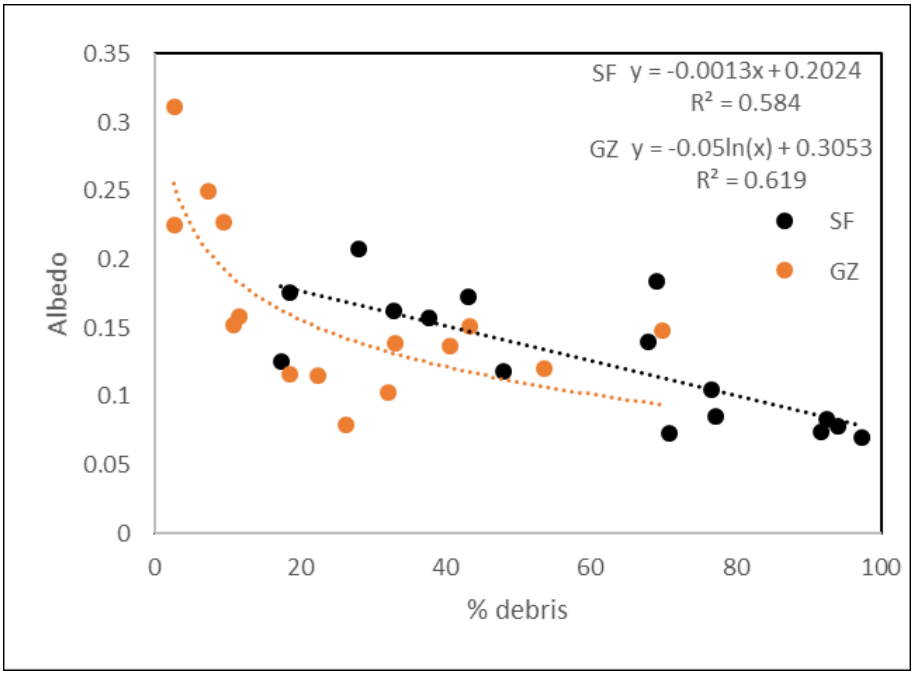

Figure 9 Scatterplot of percentage of debris (%) and albedo at Gran Zebrù (GZ) (orange) and Sforzellina (SF) glacier (black). In the equations y is albedo and x is the percentage of debris (%).

The linear positive correlation between the debris mass at each quadrat and the mean surface temperature measured using infrared thermography (R=0.84; p=7*10^-9) (Fig. 10) suggests that the debris exerts an important impact increasing the glacier surface temperature proportionally to the quantity of debris present at the glacier surface.

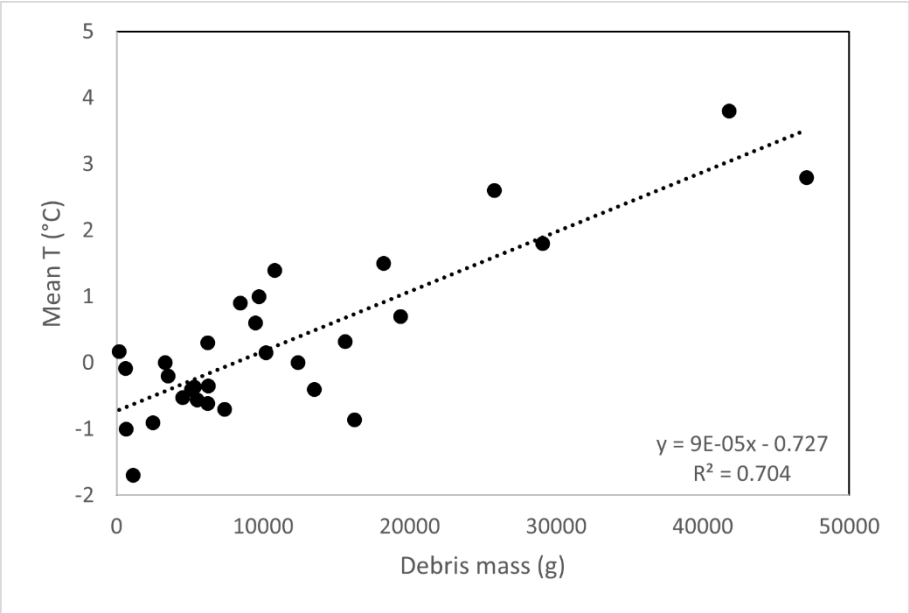

Figure 10 Scatterplot of debris mass (g) and mean surface temperature (°C) at each quadrat at Gran Zebrù and Sforzellina glacier.

4.8 Influence of supraglacial debris on ablation

The supraglacial debris coverage rate not only is influenced by the glacier ablation but also viceversa. Here we consider only Sforzellina glacier as an example and, considering the period 30/07/2020 to 26/08/2020, we found a quadratic relationship between the percentage of debris cover (at the end of the study period) and the mean ablation rate (mm w.e.) (Fig. 11a). Also, the relationship between albedo and ablation rate can be explained by a quadratic function (Fig. 11b). The ablation rate increases from 41 mm w.e.per day to 56 w.e. per day at increasing percentage debris cover between 19% and 68% (Fig. 11a), explained by the decrease of albedo at increasing debris cover (Fig. 11b). At higher percentage debris cover (> 80%), the ablation rates tend to decrease at increasing debris cover, with the quadrats having the highest percentage of debris cover (SF7 and SF8) featuring similar ablation rates (42 and 43 mm w.e. per day) of the quadrat having the lowest debris cover (SF4 with 41 mm w.e. per day) (Fig. 11a). The decrease of the ablation rates is due to the increasing fraction of the

surface covered by clasts that are thicker than the critical thickness, causing the insulation effect of debris overcoming the albedo effect.

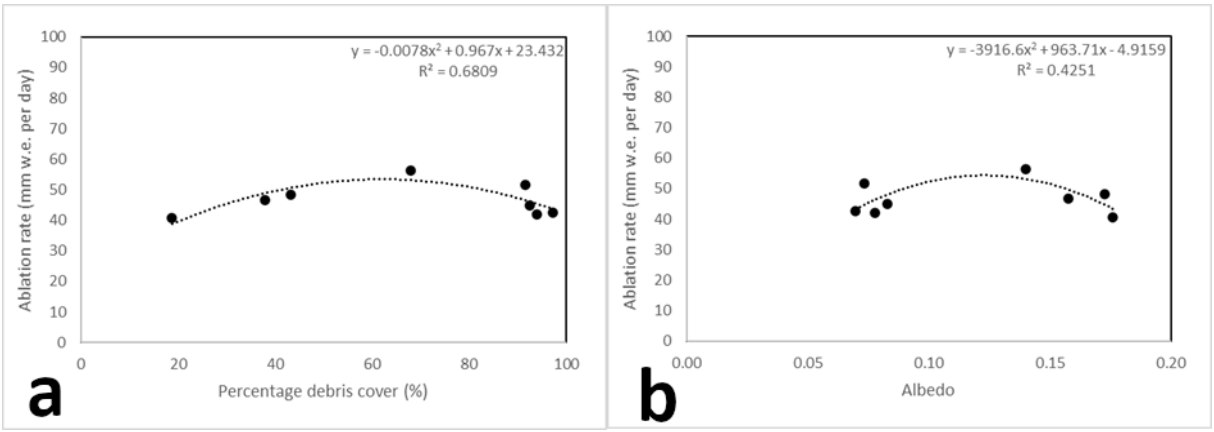

Figure 11 a) Scatterplot of percentage debris cover (%) and ablation rate (mm w.e. per day) at the 8 quadrats at Sforzellina glacier between 30/07/2020 and 26/08/2020. b) Scatterplot of albedo and ablation rate (mm w.e. per day) at the 8 quadrats at Sforzellina glacier between 30/07/2020 and 26/08/2020.

5. Discussion

5.1 Debris coverage evolution and englacial debris concentration

The debris coverage rate at Sforzellina glacier resulted to be much higher than at Gran Zebrù, both in terms of mass and percentage, with mean values almost three times higher in the former in terms of mass.

To our best knowledge only few quantitative analyses regarding the sparse debris evolution on glaciers are reported in the literature, that can be compared to our results. Azzoni et al. (2016) reported a debris coverage rate of 6 g/m^2 per day at Forni Glacier (Ortles-Cevedale group, Italy) during the ablation season of 2013, much lower than our results, but they evaluated the rate of increase of fine debris, while at our site both fine and coarse debris were present, and the latter had a major impact in terms of mass. Moreover, Forni glacier is also a

larger glacier than our sites, covering a much higher area (10.50 km^2, surveyed in 2016, Paul et al., 2019), and the measurements were performed at lower altitude (about 2600-2700 m a.s.l.) although they are located in the same mountain group and not far from our sites (about 7 Km far from Gran Zebrù and about 8 from Sforzellina).

Considering the temporal evolution of the sparse debris cover, differently from us, Fyffe et al. (2020) reported no overall increase in the percentage debris cover in their investigated area of ~180 × 200 m of dirty ice at Miage Glacier (Mont Blanc group, Western Italian Alps, Italy), between 17 July and 22 August 2017. Also, in this case Miage glacier is a valley debris-covered glacier, covers an area of 10.10 km^2 (surveyed in 2015, Paul et al., 2019) and the work was performed at much lower altitude (between 2453 and 2484 m a.s.l.). They observed that fine debris and coarser clasts that melt-out from crevasse traces were washed into hollows and streams channels, increasing the concentration there while the intervening ice became cleaner, not resulting in a uniform increase in debris cover.

At our quadrats at Gran Zebrù and Sforzellina, we consider that the accumulation of debris on the surface has occurred mainly by melt out of englacial debris (primary dispersal according to Kirkbride and Deline, 2013) and not by secondary dispersal (gravitational processes that redistribute debris from features formed by differential ablation according to Kirkbride and Deline, 2013), since our sampling areas were not close to medial moraines with a continuous debris layer. Therefore, the debris coverage rates are surely influenced by the ablation rates. The ablation data measured at the stakes (Table 4) can be used to understand the influence of melt on the release of the englacial debris that accumulates on the surface of the glacier. For example, the total melt at S1 was 135 cm with a mass increase of debris of only 160 g, while at SF7 the melt was lower (126 cm) but the mass increase was of 19367 g (Table 4). Even on the same glacier the highest melt doesn't correspond to the highest mass increase of the

supraglacial debris (e.g. S1 and S5). Therefore, the increase of the debris on the glacier surface doesn't depend only on the quantity of ice that melts out but also on the quantity of debris contained in the ice. Moreover it is also influenced by the geometry of the glacier ice flow lines, as debris is advected through the glacier following englacial flowpaths (Anderson and Anderson, 2016).

Thanks to the ablation data, we were able to obtain the englacial debris concentrations at 3 sites at Gran Zebrù and at 4 sites at Sforzellina. The values obtained (Table 4) show that the concentration was almost double at Sforzellina respect to Gran Zebrù (respectively 10810 and 6131 g/m^3) and the values at each glacier were not homogeneous, confirming that the englacial debris concentration has a certain variability in a glacier. We also found increasing debris concentrations toward the glacier front at both glaciers, similarly to what described by Miles et al. (2021) at Khumbu glacier (Nepal), with 6.4 % of debris (in terms of volume) near the glacier front, while lower values (≤0.7 %) in the mean-to-upper ablation area. A spatial variability of englacial debris concentrations was reported also by Kirkbride and Deline (2013) at Glacier d'Estelette (Mont Blanc group, Western Italian Alps, Italy). They measured debris concentrations between 70 and 140 g/m^3 for dispersed facies, and between 3000 and 332 900 g/m^3 for debris bands. Although our sampling areas can be classified as dispersed facies, as we did not observe debris bands emerging at the quadrats, only one quadrat at Gran Zebrù (S1) has an englacial concentration in the same range of the dispersed facies at Glacier d'Estelette, while all the other quadrats at Gran Zebrù and Sforzellina have concentrations that are in the same range of the debris bands values.

Our data showed that the englacial debris concentration is higher at Sforzellina than at Gran Zebrù. Different factors could have induced this difference between the two glaciers. First, one factor influencing the englacial debris concentration is the sediment supply to the glacier.

Topography of the surrounding terrains, lithology and climate are considered the factors that control the debris supply to a glacier (i.e. Mayr and Hagg, 2019). At these two glaciers we can assume reasonably that debris is supplied mainly from the degradation of the rockwalls surrounding the glaciers (headwalls and sidewalls) by rockfalls and to a lesser extent by snow avalanches. Rockfalls were observed at both glaciers during the visits in the field, and at Gran Zebrù glacier where also a small debris flow occurred. As we didn't find rounded clasts and striated clasts, we can assume that the debris did not suffer a basal transport. At Gran Zebrù rock debris is supplied to the glacier from the rockwalls and talus slopes having an area of 222394 m^2, extending up to 3653 m a.s.l., with a prevalent S and SW aspect and a mean slope of 42 degrees. The source areas are composed at 43% by sedimentary rocks and at 57% by metamorphic rocks. Differently, at Sforzellina glacier, debris is supplied by rockwalls and talus slopes having an area of 135427 m^2, extending up to 3360 m a.s.l. (Corno dei Tre Signori peak), having a prevalent NW aspect, a mean slope of 49 degrees and mainly composed by metamorphic rocks. Despite the smaller extent of the rockwalls and talus at Sforzellina glacier rockfalls are probably favoured both by the steeper slopes, since their source areas are usually expected on slopes >40° (Knoflach et al., 2021) but also for its lower elevations, that could favour freeze-thaw cycles and thermal weathering (e.g. Draebing, 2021).

The influence of the aspect of the debris source areas, can seem paradoxical because the north-facing slopes supply more debris, suggested also by the presence of a debris-covered glacier (Solda glacier/Suldenferner) at the base of the north face of Gran Zebrù, on the opposite side of the mountain respect to Gran Zebrù glacier. This contrasts with what reported for example, by Nagai et al. (2013) in the Bhutan Himalaya, observing that the southwest-facing slopes supply the largest quantity of debris mantle there, since diurnal freeze–thaw cycles are more active there. But it must be considered that their study area is located in a

different climatic environment, affected by the summer monsoon, and glaciers are located at elevations between 4000 m and 7500 m a.s.l..

This apparent paradox can be explained by the structural assessment of the rockwalls, with the presence of a large north-vergent fold having a WSW-ENE direction (large complex syncline of Gran Zebrù) (Montrasio et al., 2012). Moreover, on the Gran Zebrù north face snow tends to remain more

than on the south face during the ablation season, providing meltwater that can infiltrate in the bedrock, causing rock weathering in case of freeze-thaw cycles.

It must also be considered that the rockwalls at Gran Zebrù and Sforzellina glaciers are composed by different lithotypes, having different weathering rates. In particular, the metamorphic rocks, composing all the rockwalls surrounding Sforzellina glacier and the sidewalls at Gran Zebrù glacier appear more fractured than the sedimentary rocks that form the backwall at Gran Zebrù glacier (e.g. Fig. 2). Moreover, considering the entire Gran Zebrù south rockwall, 70% of its area supplies debris to the western tongue of the glacier, while only 30% supplies debris to the eastern tongue, our study area. As a consequence, the western tongue is more debris covered than the eastern one.

Savi et al. (2021) investigated the potential controlling factors of mass movements in the upper Solda basin, located in the Ortles-Cevedale group and neighbouring to Cedec Valley, where Gran Zebrù glacier is located, showing that most detachments at high elevations take place along channel and avalanche tracks and in recently deglaciated areas. Also, they reported a significant decrease in slope stability since 2000s in their study area, especially in the areas near glaciers. This suggests a probable future increase of englacial debris concentrations and of the supraglacial debris cover of glaciers in this area.

Furthermore, the englacial debris concentration depends not only by the debris supply, but also on the contemporary net snow accumulation in the areas of the glacier where rockfalls occur (Kirkbride and Deline, 2013), that in our two cases is higher at Gran Zebrù as demonstrated indirectly by the maximum thickness of the glacier that exceed 60 m at Gran Zebrù (Forte et al., 2021) against 40-42 m at Sforzellina (Santin et al., under rev).

5.2 Debris sources

At both Gran Zebrù and Sforzellina debris was mostly composed by the coarser fraction (>2 mm), while the finer fractions represented only a small percentage in terms of mass. The lithology of the debris reflects the lithology of the rockwalls surrounding the two glaciers as expected. In particular at Gran Zebrù the englacial debris of this area of the glacier (Fig. 1C) derives only from the backwall without any input from the sidewalls (metamorphic) while debris supplied by the metamorphic sidewalls accumulates at the base of the walls and forms the continuous debris cover of the eastern section of the glacier tongue (Fig. 1C). As said before, these two characteristics of debris suggest that it originates mainly from the rockwalls, from which it falls on the glacier, undergoes englacial transport and then melts out. In addition, debris contains a fraction of subrounded clasts, thus suggesting also a possible basal transport although the absence of typical shape of basal transport (e.g. flatiron) or striations in our debris samples indicate a quite short transport and the absence of a bedrock under the glacier harder than the sedimentary rocks composing debris.

5.3. The effect of debris on albedo and on the surface temperature

We found that albedo is inversely correlated with the percentage debris cover both at Gran Zebrù and Sforzellina glaciers, logarithmically at the first and linearly at the second. The decrease of albedo at increasing debris cover is expected, since all the materials composing supraglacial debris have lower albedo values than glacier ice (Brock et al., 2000). Brock et al. (2000) found that albedo is inversely correlated with the percentage debris cover at Haut Glacier d'Arolla (Valais, Switzerland), with values of albedo > 0.30 only with percentage debris cover < 5%. This is true also in our case, where only a single quadrat (S3B) showed an albedo > 0.30, with a value of 0.31 and 2.8 % of debris. Moreover, also Fyffe et al. (2020) found an inverse relationship between albedo and percentage debris cover at Miage glacier, but with a stronger relationship using a quadratic respect to a linear relationship. Azzoni et al. (2016) found a linear relation between the debris cover ratio and albedo natural logarithm values at Forni glacier, with an albedo range of 0.06-0.32 and percentages of debris from 1 to 63%. Our albedo data fall within the same range (0.07-0.21 at Sforzellina and 0.08-0.31 at Gran Zebrù) but are influenced in a different way by the percentage of debris. This suggests that the different characteristics of the debris (e.g. lithology, colour, grain size) and not only its quantity have an impact on the albedo of a glacier, as reported for example by Juen et al. (2013).

The presence of the supraglacial debris also influences the surface temperatures of the glacier. We found that debris increases the glacier surface temperature proportionally to the quantity of debris present on the surface. We observed that the highest temperatures are reached on the surface of the biggest clasts, as for example showed in Figure 12, where in the thermal image of quadrat SF8B it is possible to see that coarse debris has surface temperatures higher than 0°C and the biggest rock fragments feature the highest temperatures. Therefore, like for

albedo, the surface temperature is surely influenced by the granulometry of debris and probably also by the characteristics of the rocks, other than the meteorological conditions.

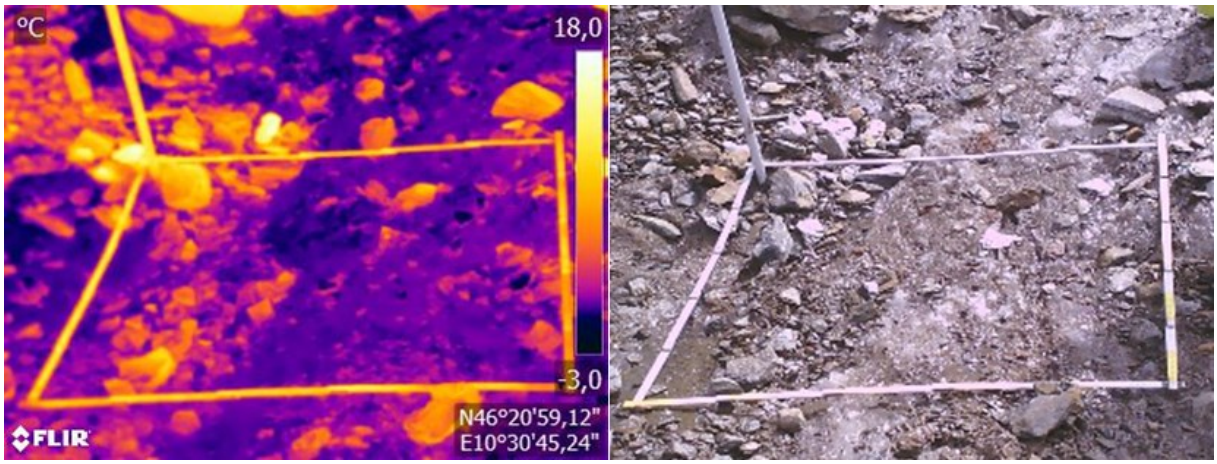

Figure 12 Thermal image and corresponding visible image of quadrat SF8B. Images taken on 18/09/2019 at 13.24 local time.

5.4 Influence of supraglacial debris on ablation

We obtained a quadratic relationship between the percentage debris cover and the mean ablation rate at Sforzellina glacier, with an increase of ablation at increasing debris cover for moderate covers (<80 %) (Fig. 11a). When the cover becomes nearly complete (>80%) the ablation rate started to decline. This fact can be explained as suggested by Fyffe et al., (2020) in which the insulation effect of clasts thicker than the critical thickness overwhelms the reduced albedo of the debris cover. In addition, they reported a constant ablation under moderate covers (~30-80%), while in the same range of coverage our data show a linear increase of the ablation rates at increasing debris cover (Fig. 11a). Fyffe et al., (2020) explained their constant ablation under moderate covers by a simultaneous increase of clast size with percentage of debris cover contrasting the role of albedo; differently in our case the linear increase of the ablation could be related to the constant clast size with the increase of debris

coverage. Unfortunately, we cannot demonstrate this hypothesis because we measure only the percentage of the clasts larger than 25 mm and not the singular diameters of the clasts.

6. Conclusions

Our study shows that the supraglacial debris is increasing rapidly at the two investigated glaciers of the Ortles-Cevedale group, Gran Zebrù glacier and Sforzellina glacier, both in terms of mass and percentage debris cover, with values respectively of 211 g/m^2 per day and 0.64% per day and 621 g/m^2 per day and a percentage of 2.07% per day. The big differences of rate between the two glaciers are mainly due to the quantity of debris contained in the ice and this content is due to the extension and the morphology of the surrounding terrains, their lithology and structural assessment and lastly also to climate.

The englacial debris concentration is higher at Sforzellina Glacier also for the lower net accumulation balance.

The characteristics of debris, composed mainly of coarse rock clasts, suggest a debris supply mainly from the surrounding rockwalls and an englacial transport in both the glaciers. The albedo decreases at increasing percentage of debris covering the glacier surface, linearly at Sforzellina and logarithmically at Gran Zebrù while the surface temperatures are influenced by the presence of debris, increasing linearly at increasing mass of debris present on the glacier surface.

Finally, the relationship between the percentage of debris and the mean ablation rate is explained by a quadratic function, with the ablation rate increasing at increasing debris cover for moderate debris covers and decreasing ablation rates with high percentages of debris cover (>80%).

7. Acknowledgments

We want to thank the Stelvio National Park for their logistical and financial support. A special thanks also to all the other researchers and students that concur in the field activities.

Appendix

Table A.1 Percentage debris cover (%), debris mass (g) and albedo at each quadrat at the beginning (A) and at the end of the study period (B)

Percentage debris cover (%)	**A**	**B**		**Debris mass (g)**	**A**	**B**		**Albedo**	**A**	**B**
S1	34.0	2.7		**S1**	668	160		**S1**	NA	0.23
S2	NA	NA		**S2**	NA	NA		**S2**	NA	NA
S3	11.0	2.8		**S3**	3498	602		**S3**	0.15	0.31
S4	26.4	40.7		**S4**	10778	6238		**S4**	0.08	0.14
S5	33.2	11.6		**S5**	6278	10208		**S5**	0.14	0.16
S6	9.6	7.4		**S6**	4529	2467		**S6**	0.23	0.25
S7	32.3	22.5		**S7**	5287	5492		**S7**	0.10	0.11
S8	53.6	18.7		**S8**	7361	6203		**S8**	0.12	0.12
S9	69.8	43.4		**S9**	15610	16224		**S9**	0.15	0.15

Mean	33.7	18.7		**Mean**	6751	5949		**Mean**	0.14	0.18
SF1	48.1	67.9		**SF1**	12395	47074		**SF1**	0.12	0.14
SF2	70.9	91.7		**SF2**	29334	41816		**SF2**	0.07	0.07
SF3	33.0	37.8		**SF3**	13501	3337		**SF3**	0.16	0.16
SF4	17.4	18.7		**SF4**	1132	8451		**SF4**	0.13	0.18
SF5	NA	NA		**SF5**	NA	NA		**SF5**	NA	NA
SF6	28.2	43.2		**SF6**	9491	9723		**SF6**	0.21	0.17
SF7	69.2	94.1		**SF7**	5116	19367		**SF7**	0.18	0.08
SF8	76.7	97.3		**SF8**	29079	18223		**SF8**	0.10	0.07
SF9	77.2	92.5		**SF9**	13814	25781		**SF9**	0.09	0.08
Mean	52.6	67.9		**Mean**	14233	21721		**Mean**	0.13	0.12

References

Anderson, L. S., & Anderson, R. S. (2016). Modeling debris-covered glaciers: response to steady debris deposition. The Cryosphere, 10(3), 1105-1124.

Arganda-Carreras, I., Kaynig, V., Rueden, C., Eliceiri, K. W., Schindelin, J., Cardona, A., & Sebastian Seung, H. (2017). Trainable Weka Segmentation: a machine learning tool for microscopy pixel classification. *Bioinformatics*, *33*(15), 2424-2426.

Azzoni, R. S., Senese, A., Zerboni, A., Maugeri, M., Smiraglia, C., & Diolaiuti, G. A. (2016). Estimating ice albedo from fine debris cover quantified by a semi-automatic method: the case study of Forni Glacier, Italian Alps. The Cryosphere, 10, 665-679.

Azzoni, R. S., Fugazza, D., Zerboni, A., Senese, A., D'Agata, C., Maragno, D., ... & Diolaiuti, G. A. (2018). Evaluating high-resolution remote sensing data for reconstructing the recent evolution of supra glacial debris: A study in the Central Alps (Stelvio Park, Italy). *Progress in Physical Geography: Earth and Environment*, *42*(1), 3-23.

Benn, D. I., & Ballantyne, C. K. (1994). Reconstructing the transport history of glacigenic sediments: a new approach based on the co-variance of clast form indices. *Sedimentary geology*, *91*(1-4), 215-227.

Bolch, T., Buchroithner, M., Pieczonka, T., & Kunert, A. (2008). Planimetric and volumetric glacier changes in the Khumbu Himal, Nepal, since 1962 using Corona, Landsat TM and ASTER data. *Journal of Glaciology*, *54*(187), 592-600.

Brock, B. W., Willis, I. C., & Sharp, M. J. (2000). Measurement and parameterization of albedo variations at Haut Glacier d'Arolla, Switzerland. Journal of Glaciology, 46(155), 675-688.

Brook, M. S., Hagg, W., & Winkler, S. (2013). Debris cover and surface melt at a temperate maritime alpine glacier: Franz Josef Glacier, New Zealand. New Zealand Journal of Geology and Geophysics, 56(1), 27-38.

Carturan, L., Filippi, R., Seppi, R., Gabrielli, P., Notarnicola, C., Bertoldi, L., ... & Dalla Fontana, G. (2013). Area and volume loss of the glaciers in the Ortles-Cevedale group (Eastern Italian Alps): controls and imbalance of the remaining glaciers. *The Cryosphere*, 7(5), 1339-1359.

D'Agata, C., Bocchiola, D., Maragno, D., Smiraglia, C., & Diolaiuti, G. A. (2014). Glacier shrinkage driven by climate change during half a century (1954–2007) in the Ortles-Cevedale group (Stelvio National Park, Lombardy, Italian Alps). *Theoretical and applied climatology*, 116(1), 169-190.

Diolaiuti, G. A., Azzoni, R. S., D'Agata, C., Maragno, D., Fugazza, D., Vagliasindi, M., ... & Smiraglia, C. (2019). Present extent, features and regional distribution of Italian glaciers. La Houille Blanche, (5-6), 159-175.

Draebing, D. (2021). Identification of rock and fracture kinematics in high alpine rockwalls under the influence of elevation. Earth Surface Dynamics, 9(4), 977-994.

Fischer, M., Huss, M., Barboux, C., & Hoelzle, M. (2014). The new Swiss Glacier Inventory SGI2010: relevance of using high-resolution source data in areas dominated by very small glaciers. Arctic, Antarctic, and Alpine Research, 46(4), 933-945.

Forte, E., Santin, I., Ponti, S., Colucci, R. R., Gutgesell, P., & Guglielmin, M. (2021). New insights in glaciers characterization by differential diagnosis integrating GPR and remote sensing techniques: A case study for the Eastern Gran Zebrù glacier (Central Alps). Remote Sensing of Environment, 267, 112715.

Fyffe, C. L., Woodget, A. S., Kirkbride, M. P., Deline, P., Westoby, M. J., & Brock, B. W. (2020). Processes at the margins of supraglacial debris cover: Quantifying dirty ice ablation and debris redistribution. Earth Surface Processes and Landforms, 45(10), 2272-2290.

Glasser, N. F., Holt, T. O., Evans, Z. D., Davies, B. J., Pelto, M., & Harrison, S. (2016). Recent spatial and temporal variations in debris cover on Patagonian glaciers. *Geomorphology*, *273*, 202-216.

Gregorich, E. G., & Carter, M. R. (2007). *Soil sampling and methods of analysis*. CRC press.

Hagg, W., Brook, M., Mayer, C., & Winkler, S. (2014). A short-term field experiment on sub-debris melt at the highly maritime Franz Josef Glacier, Southern Alps, New Zealand. Journal of Hydrology (New Zealand), 153-161.

Jiang, S., Nie, Y., Liu, Q., Wang, J., Liu, L., Hassan, J., ... & Xu, X. (2018). Glacier change, supraglacial debris expansion and glacial lake evolution in the Gyirong river basin, central Himalayas, between 1988 and 2015. *Remote Sensing*, *10*(7), 986.

Juen, M., Mayer, C., Lambrecht, A., Wirbel, A., & Kueppers, U. (2013). Thermal properties of a supraglacial debris layer with respect to lithology and grain size. Geografiska Annaler: Series A, Physical Geography, 95(3), 197-209.

Kellerer-Pirklbauer, A. (2008). The supraglacial debris system at the Pasterze Glacier, Austria: spatial distribution, characteristics and transport of debris. Zeitschrift für Geomorphologie, Supplementary Issues, 3-25.

Kirkbride, M. P., & Deline, P. (2013). The formation of supraglacial debris covers by primary dispersal from transverse englacial debris bands. *Earth Surface Processes and Landforms*, *38*(15), 1779-1792.

Knoflach, B., Tussetschläger, H., Sailer, R., Meißl, G., & Stötter, J. (2021). High mountain rockfall dynamics: rockfall activity and runout assessment under the aspect of a changing cryosphere. Geografiska Annaler: Series A, Physical Geography, 1-20.

Leonelli, G., Battipaglia, G., Cherubini, P., Saurer, M., Siegwolf, R. T., Maugeri, M., ... & Pelfini, M. (2017). Larix decidua δ18O tree-ring cellulose mainly reflects the isotopic signature of winter snow in a high-altitude glacial valley of the European Alps. Science of the Total Environment, 579, 230-237.

Mattson, L. E. (1993). Ablation on debris covered glaciers: an example from the Rakhiot Glacier, Punjab, Himalaya. Intern. Assoc. Hydrol. Sci., 218, 289-296.

Mayr, E., & Hagg, W. (2019). Debris-covered glaciers. In Heckmann, T., & Morche, D., (eds.) Geomorphology of proglacial systems. Landform and sediment dynamics in recently deglaciated alpine landscapes. Cham: Springer International Publishing, 59–71.

Miles, K. E., Hubbard, B., Miles, E. S., Quincey, D. J., Rowan, A. V., Kirkbride, M., & Hornsey, J. (2021). Continuous borehole optical televiewing reveals variable englacial debris concentrations at Khumbu Glacier, Nepal. *Communications Earth & Environment*, *2*(1), 1-9.

Mölg, N., Bolch, T., Walter, A., & Vieli, A. (2019). Unravelling the evolution of Zmuttgletscher and its debris cover since the end of the Little Ice Age. *The Cryosphere*, *13*, 1889-1909.

Montrasio, A., Berra, F., Cariboni, M., Ceriani, M., Deichmann, N., Ferliga, C., Gregnanin, A., Guerra, S., Guglielmin, M., Jadoul, F., Longhin, M., Mair, V., Mazzoccola, D., Sciesa, E., & Zappone, A. (2012). Note illustrative della Carta Geologica d'Italia alla scala 1:50000 - foglio 024. ISPRA - Servizio Geologico d'Italia.

Muhammad, S., Tian, L., Ali, S., Latif, Y., Wazir, M. A., Goheer, M. A., ... & Shiyin, L. (2020). Thin debris layers do not enhance melting of the Karakoram glaciers. Science of the Total Environment, 746, 141119.

Nagai, H., Fujita, K., Nuimura, T., & Sakai, A. (2013). Southwest-facing slopes control the formation of debris-covered glaciers in the Bhutan Himalaya. *The Cryosphere*, *7*(4), 1303-1314.

Østrem, G. (1959). Ice melting under a thin layer of moraine, and the existence of ice cores in moraine ridges. Geografiska Annaler, 41(4), 228-230.

Paul, F., Rastner, P., Azzoni, R. S., Diolaiuti, G., Fugazza, D., Le Bris, R., Nemec, J., Rabatel, A., Ramusovic, M., Schwaizer, G., Smiraglia, C. (2019). Glacier inventory of the Alps from Sentinel-2, shape files. *PANGAEA*, https://doi.org/10.1594/PANGAEA.909133. Supplement to: Paul, F., Rastner, P., Azzoni, R. S., Diolaiuti, G., Fugazza, D., Le Bris, R., ... & Smiraglia, C. (2020). Glacier shrinkage in the Alps continues unabated as revealed by a new glacier inventory from Sentinel-2. Earth System Science Data, 12(3), 1805-1821.

Reznichenko, N., Davies, T., Shulmeister, J., & McSaveney, M. (2010). Effects of debris on ice-surface melting rates: an experimental study. Journal of Glaciology, 56(197), 384-394.

Salerno, F., Gambelli, S., Viviano, G., Thakuri, S., Guyennon, N., D'Agata, C., ... & Tartari, G. (2014). High alpine ponds shift upwards as average temperatures increase: a case study of the Ortles–Cevedale mountain group (Southern Alps, Italy) over the last 50 years. Global and Planetary Change, 120, 81-91.

Savi, S., Comiti, F., & Strecker, M. R. (2021). Pronounced increase in slope instability linked to global warming: A case study from the eastern European Alps. *Earth Surface Processes and Landforms*.

Schindelin, J., Arganda-Carreras, I., Frise, E., Kaynig, V., Longair, M., Pietzsch, T., ... & Cardona, A. (2012). Fiji: an open-source platform for biological-image analysis. *Nature methods*, *9*(7), 676-682.

Schindelin, J., Rueden, C. T., Hiner, M. C., & Eliceiri, K. W. (2015). The ImageJ ecosystem: An open platform for biomedical image analysis. *Molecular reproduction and development*, *82*(7-8), 518-529.

Schneider, C. A., Rasband, W. S., & Eliceiri, K. W. (2012). NIH Image to ImageJ: 25 years of image analysis. *Nature methods*, *9*(7), 671-675.

Soncini, A., Bocchiola, D., Azzoni, R. S., & Diolaiuti, G. (2017). A methodology for monitoring and modeling of high altitude Alpine catchments. Progress in Physical Geography, 41(4), 393-420.

Stokes, C. R., Popovnin, V., Aleynikov, A., Gurney, S. D., & Shahgedanova, M. (2007). Recent glacier retreat in the Caucasus Mountains, Russia, and associated increase in supraglacial debris cover and supra-/proglacial lake development. *Annals of Glaciology*, *46*, 195-203.

Tarca, G., & Guglielmin, M. (2022). Using ground-based thermography to analyse surface temperature distribution and estimate debris thickness on Gran Zebrù glacier (Ortles-Cevedale, Italy). *Cold Regions Science and Technology*, 103487.

Xie, F., Liu, S., Wu, K., Zhu, Y., Gao, Y., Qi, M., ... & Tahir, A. A. (2020). Upward Expansion of Supra-Glacial Debris Cover in the Hunza Valley, Karakoram, During 1990∼ 2019. *Frontiers in Earth Science*, *8*, 308.

Wentworth, C. K. (1922). A scale of grade and class terms for clastic sediments. *The journal of geology*, *30*(5), 377-392.

5. Using PlanetScope images to investigate the evolution of small glaciers in the Alps

Giulia Tarca [1], Martin Hoelzle[2], Mauro Guglielmin[1*]

1 Department of Theoretical and Applied Sciences, Insubria University, Via Dunant, 3, 21100 Varese, Italy.

2 Department of Geosciences, University of Fribourg, Ch. du Musée 4, 1700 Fribourg, Switzerland

*corresponding author mauro.guglielmin@uninsubria.it

Manuscript submitted to the Journal Remote Sensing of Environment

Abstract

Small glaciers prevail in the Alps and are more sensitive to climate change respect to large one, but despite that, they are less studied. In this study we assessed the potential of daily, high resolution (3 m pixel size) PlanetScope images for monitoring small Alpine glaciers. We compared the evolution of five small glaciers, located in different sectors of the Alps to investigate also the influence of the topographic and climatic variables on them. The investigated glaciers are: Bors (Piedmont, Italy), Seewjinen (Valais, Switzerland), Pizzo Ferrè (Lombardy, Italy), Gran Zebrù (Lombardy, Italy) and Solda Orientale (South Tirol, Italy). We mapped the glacier outline and Equilibrium Line Altitude (ELA) through PlanetScope images from the end of the ablation season for each year and each glacier. We found that the glaciers lost between 5 and 14% of their area between 2017 of 2021, with a mean area loss of -1.6% per year. The strongest shrinkage is recorded in the smallest glacier (Pizzo Ferrè). PlanetScope images, with their high spatial and temporal resolution proved to be a valuable tool for small glaciers monitoring. They permitted to map small glaciers with small uncertainties (between 1.1 and 2.5% of the glacier area), much lower than with medium resolution satellite data and to increase the availability of data. The northern exposed glaciers are located lower than the southern exposed and their ELA is found about 340 m lower on average, being significantly correlated with the potential solar radiation received by the glaciers. The ELA showed a variability in the different year, being probably influenced both by air temperatures and precipitation but also by other factors as wind drift, avalanching or cloud cover.

Keywords: small glaciers, remote sensing, PlanetScope, Alps, climate

1. Introduction

In the Alps small glaciers prevail, indeed 92% of the glaciers have an area smaller than 1 km^2 (Paul et al., 2020). Moreover, small glaciers are showing largest relative area decrease respect to the large glaciers (e.g. Linsbauer et al., 2021). However, despite the relevance of small glaciers, Alpine glacier research focuses mainly on medium and large glaciers (Huss & Fischer, 2016).

The PlanetScope satellite constellation is able to acquire images of the entire land surface of the Earth every day, at a spatial resolution of 3 m (Planet, 2021), offering the possibility to monitor glaciers at higher spatial and temporal resolution than other commonly used satellites (e.g. Landsat, Sentinel) and could therefore be suitable for small glaciers monitoring. PlanetScope satellites are relatively recent, since the first launch was in 2016, but they have been already used for different applications in glacier research. PlanetScope images have been used to map glaciers outlines, for example by Pudełko et al. (2018) on glaciers of 3-14 km^2 surface areas at King George Island (Antarctica), by Chand et al. (2020), for the Parvati glacier (24 km^2) in Himalaya, or by Shaw et al. (2021) for glaciers of 3-26 km^2 areas in the central Chilean Andes.

PlanetScope images have been also used to map surface velocities of glaciers, for example by Millan et al., (2019) in the southern Alps of New Zealand, in the Andes and in the European Alps, and by Steiner et al. (2018) at Khurdopin glacier (Pakistan). PlanetScope images have been used also to generate digital elevation models of glaciers, as Ghuffar (2018) or to detect elevation changes at successive times at the Khurdopin surging glacier (Pakistan) and to calculate the elevation difference caused by the glacier surge at Shisper glacier (Pakistan, Aati & Avouac, 2020)). PlanetScope images have also been used to study giant ice avalanches from two glaciers in Tibet by Kääb et al. (2018) and to map glacier lakes in the Hindu Kush,

Karakoram and Himalaya region by Qayyum et al. (2020). Although they have been used for a wide range of applications, at our knowledge PlanetScope images haven't been used to monitor small glaciers (<1 km^2). Therefore for these reasons the first aim of this work is to assess the potential of PlanetScope images for mapping small glaciers and monitoring their surface evolution, both at seasonal and interannual time scales.

In addition here we want also to compare the evolution of the selected 5 different alpine small glaciers, all with a comparable size but different aspect and located in different climatic sectors of the Alps, to investigate the relation between their evolution and climatic and topographic variables.

2. Study areas

Five glaciers located in different sectors of the Alps were chosen, covering an area lower or slightly higher than 1 km^2. The glaciers are, from west to east: Bors (Piedmont, Italy), Seewjinen (Valais, Switzerland), Pizzo Ferrè (Lombardy, Italy), Gran Zebrù (Lombardy, Italy) and Solda Orientale (South Tirol, Italy) (Fig. 1). Bors glacier and Seewjinen glacier belong to the Monte Rosa group, Pizzo Ferrè glacier to the Tambò-Stella group and Gran Zebrù glacier and Solda Orientale glacier to the Ortles-Cevedale group. Bors glacier covers an area of 0.645 km^2 (surveyed in 2017), Seewjinen 1.339 km^2 (surveyed in 2015), Pizzo Ferrè 0.442 km^2 (surveyed in 2016), Gran Zebrù 0.579 km^2 (surveyed in 2016) and Solda Orientale 0.829 km^2 (surveyed in 2016) (Paul et al. 2019).

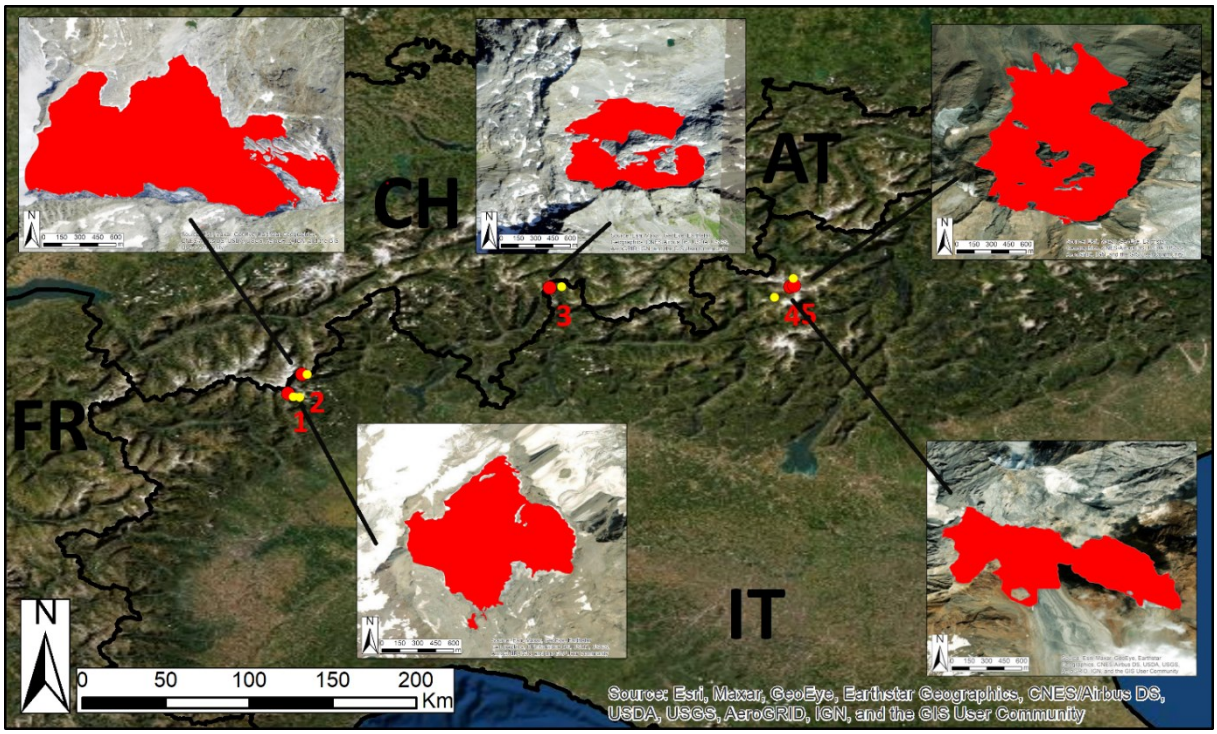

Figure 1 Geographic location of the five glaciers investigated (red points): 1) Bors glacier; 2) Seewjinengletscher; 3) Pizzo Ferrè glacier; 4) Gran Zebrù glacier; 5) Solda orientale glacier. Yellow points represent the location of the automatic weather stations (AWS) used in the study. Basemap: Esri World Imagery.

The climate of the Alps is characterized by a high complexity, caused by the interaction between the topography and the general circulation, and by the coexistence of four different climatological regimes: Mediterranean, Continental, Atlantic and Polar (Beniston, 2005). Mean annual precipitation in the Alps show a wide range of values, from about 400 to more than 3000 mm per year (Isotta et al., 2014). At the scale of the entire mountain range, the distribution of precipitation is characterized by a wet anomaly elongated along the northern rim of the Alps (about 600 km long), two major wet zones located south of the main crest (one over Lago Maggiore and one over the Julian Alps) and comparatively dry conditions at several inner-Alpine regions (Frei & Schär, 1998). The Greater Alpine Region experienced a temperature increase of 1.2 °C in the 20th century, rising about twice as much as the global mean (Auer et al., 2007). Glaciers in the Alps have been retreating since the end of the Little

Ice Age (e.g. Zemp, 2006) and are undergoing a rapid shrinkage and downwasting, with an area loss of ~39 ± 9 km² a^{-1} (~1.8% a^{-1}), regionally variable ice thickness changes (−0.5 to −0.9 m a^{-1}) and a mass loss of 1.3 ± 0.2 Gt a^{-1} between 2000 and 2014 (Sommer et al., 2020).

3. Data and methods

3.1. Data

3.1.1. Meteorological data

Table 1 List of the AWS used in this work for each glacier, sources of the data, elevation of the AWS (m a.s.l.), distance from the glacier (km) and data used (T is temperature, P is precipitation).

Glacier	AWS	Source	Elevation (m a.s.l.)	Distance from the glacier (km)	Data used
Bors	Alagna Miniere	ARPA Piemonte	1347	6	P
	Bocchetta delle Pisse	ARPA Piemonte	2410	3.5	T
Seewjinen	Passo del Moro	ARPA Piemonte	2820	2	T, P
Pizzo Ferrè	Madesimo Spluga	ARPA Lombardia	1915	5	T, P
Gran Zebrù	Santa Caterina Valfurva	ARPA Lombardia	1730	9	T, P
Solda Orientale	Solda	Provincia autonoma di Bolzano - Alto Adige	1905	4.5	P
	Solda Madriccio	Provincia autonoma di Bolzano - Alto Adige	2825	2.5	T

We used daily temperature and precipitation data recorded between 1 October 2016 and 30 September 2021 at 7 AWS located nearby the glaciers, at distances between 2 and 9 km (Fig. 1, Table 1).

3.1.2. Digital elevation models

We downloaded the available Digital Terrain Model (DTM) or Digital Surface Model (DSM) of the glaciers and their surroundings. For Gran Zebrù and Pizzo Ferrè glaciers a regional DTM with 5 m resolution from 2015 is available (source: Geoportale della Lombardia https://www.geoportale.regione.lombardia.it/), for Solda Glacier a DSM (DSM - Ghiacciai 2016/2017) with 0.5 m resolution from 2016 (source: Geoportale Alto Adige http://geocatalogo.retecivica.bz.it/geokatalog/#!), for Bors glacier a DTM with 5 m resolution (source: Geoportale Piemonte https://www.geoportale.piemonte.it/) and for Seewjinengletscher a DTM (swissALTI3D) with 2 m resolution from 2015 (source: Federal Office of Topography swisstopo https://www.swisstopo.admin.ch/).

3.1.3. Satellite images

PlanetScope 4-band (Blue: 455 - 515 nm, Green: 500 - 590 nm, Red: 590 - 670 nm, NIR: 780 - 860 nm) images were used, the level 3B PlanetScope Ortho Scene Surface Reflectance data, that are orthorectified, geometrically-, radiometrically- and atmospherically- corrected (Planet, 2021). The images have a spatial resolution of 3 m and daily temporal resolution. The PlanetScope constellation is composed by more than 180 satellites, each satellite is a CubeSat 3U form factor (10 cm by 10 cm by 30 cm). Cloud free images from the ablation seasons between 2017 and 2021 were downloaded for each glacier, as the images were not available before.

3.2. Methods

3.2.1. Meteorological data analysis

Mean monthly and annual (hydrological year) air temperatures and the sum of monthly and annual total precipitation were calculated from the daily data. The temperatures measured at the AWS were extrapolated to the median elevation of the corresponding glacier, using a standard environmental lapse rate of -0.0065 °C m^{-1} (e.g. Immerzeel et al., 2014).

3.2.3. Topographic parameters

From each DEM/DSM we calculated slope (degrees), aspect (degrees) and potential solar radiation (Wh/m^2) over one year (2021) using ArcGIS 10.6. Potential solar radiation is global radiation and includes both direct and diffuse radiation, and its calculation is based on the hemispherical viewshed algorithm (Rich, 1990; Rich et al., 1994; Fu & Rich, 2000, 2002).

For each glacier the minimum, maximum, mean and median elevation (m a.s.l.), mean slope and mean potential solar radiation (Wh/m^2) was retrieved. The general aspect of the glaciers was derived according to the main flow direction.

3.2.2. Mapping glacier outlines

The glacier outlines of the five glaciers for each year (from 2017 to 2021) were manually delineated on the satellite images. For each year we chose a cloud-free image from the end of the ablation season, with the minimum seasonal snow (Paul et al., 2013), all the images were acquired between 23/08 and 30/09. To reduce inconsistencies, the outlines were digitized by the same surveyor and on the same type of data (Racoviteanu et al., 2009). In case

of debris-covered ice, we used very high-resolution images (e.g. Google Earth, aerial orthoimagery) to guide decision on boundaries delineation, as suggested by Paul et al. (2017). Moreover, at the two glaciers where the debris cover is more extended (Gran Zebrù and Solda Orientale glaciers), also field observations were performed (see Tarca and Guglielmin, 2022 for the measurement protocol and for the former glacier data). For each glacier we obtained the glacier area (km^2) in the different years. To calculate area uncertainties, we considered an error of ±0.5 pixel (e.g. Ragettli et al., 2016).

3.2.4. End-of-summer snow line altitude

The end-of-summer snowlines were manually digitized for each year on the PlanetScope images. The lines were rasterized and the average elevation was extracted along each line from the digital elevation models (e.g. Racoviteanu et al., 2019). Since for mid-latitude mountain glaciers superimposed ice is considered negligible, the end-of-summer snow line altitude retrieved from remote sensing is an accurate approximation of the glacier Equilibrium Line Altitude (ELA, Rabatel et al., 2005), therefore we will therefore use the term ELA. The term ELA can be used for the environmental ELA, that is the regional altitude of zero mass balance, not considering the effects of shading, avalanching, snow drifting, glacier geometry and debris cover, while the effective ELA accounts for these effects (Anderson et al., 2018; Žebre et al., 2021).

3.2.5. Satellite images classification

For the glacier surface classification only two of the glaciers were chosen as example, namely Gran Zebrù glacier and Seewjinen glacier, the first representative of the Central Alps and southern-exposed, the second of the Western Alps and northern-exposed. The classification of the glaciers surface was performed using a maximum likelihood supervised classification (e.g. Shukla et al., 2009) of the surface reflectance data with the software ArcMap 10.6. Three classes were mapped: snow, supraglacial debris and ice. In case of saturation of the visible bands (1, 2 or 3), we performed the classification on the band 4 if possible, usually not affected by the problem. For Seewjinen glacier, the upper area of the glacier which in many of the satellite images resulted in shadow was removed to avoid misclassification, as the classifier is not able to discriminate the different surface types covered by shadow.

4. Results

4.1. Meteorological data

The temperatures extrapolated to the median elevation of the glaciers show mean temperatures between -2.1 and -5.9 °C at the different glaciers in the entire period (October 2016 to September 2021) (Table 2), with the warmer temperatures (-2.1 and -2.3 °C) corresponding to the two glaciers with median elevations lower than 3000 m a.s.l. (Solda Orientale and Pizzo Ferrè glaciers), while lower temperatures (-4.6 to -5.9 °C) characterize the other three glaciers, having median elevations higher than 3000 m a.s.l..

Considering the different hydrological years, the lowest mean annual temperature was recorded at all the glaciers in the 2020/2021 hydrological year, while the highest mean temperature was in the 2016/2017 hydrological year at the two glaciers located in the

Western Alps (Bors and Seewjinen glaciers) and in 2019/2020 at the three glaciers located in the Central Alps (Pizzo Ferrè, Gran Zebrù and Solda Orientale glaciers) (Fig. 2, Table 2).

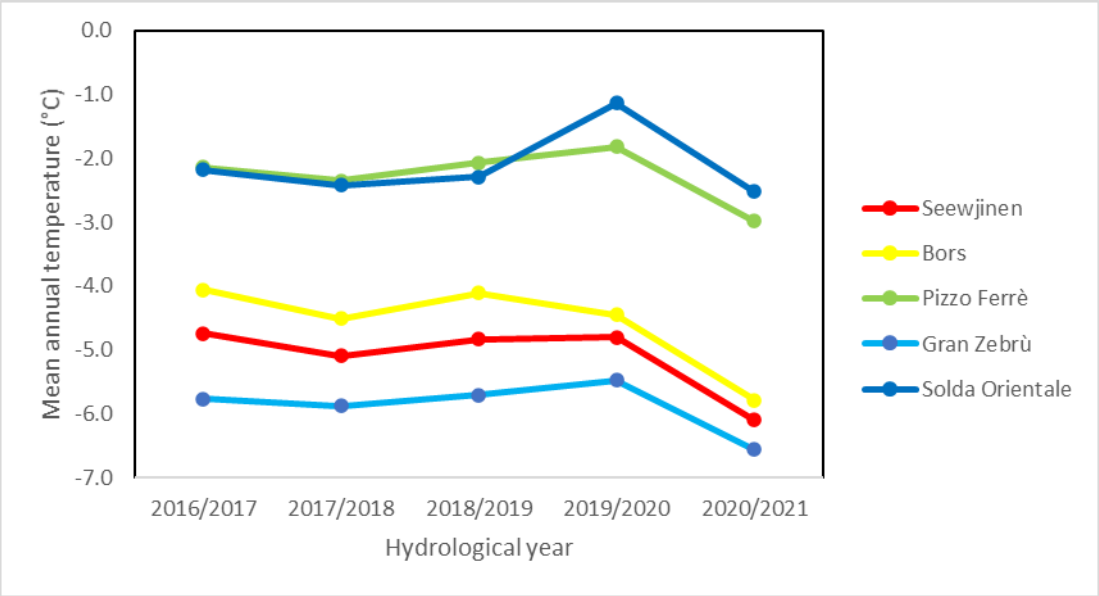

Figure 2 Mean annual (hydrological year) air temperatures extrapolated to the median glacier elevation of the glaciers for the period from October 2016 to September 2021.

Table 2 Mean annual (hydrological year) air temperatures (°C) extrapolated to the median glacier elevation of the glaciers for the period from October 2016 to September 2021 and mean of the entire study period.

Hydrological year	**Seewjinen**	**Bors**	**Pizzo Ferrè**	**Gran Zebrù**	**Solda Orientale**
2016/2017	-4.7	-4.1	-2.1	-5.8	-2.2
2017/2018	-5.1	-4.5	-2.3	-5.9	-2.4
2018/2019	-4.8	-4.1	-2.1	-5.7	-2.3
2019/2020	-4.8	-4.4	-1.8	-5.5	-1.1
2020/2021	-6.1	-5.8	-3.0	-6.6	-2.5
Mean	-5.1	-4.6	-2.3	-5.9	-2.1

The summer air temperature (from June to August, JJA) at the glaciers ranges between 2.3 °C (at Seewjinen glacier) and 6.0 °C (at Pizzo Ferrè) on average in the period 2017-2021. The coldest summer was 2021 at all the glaciers, except Gran Zebrù glacier where it was 2020, while the warmest was summer 2019 at all the glaciers (Fig. 3).

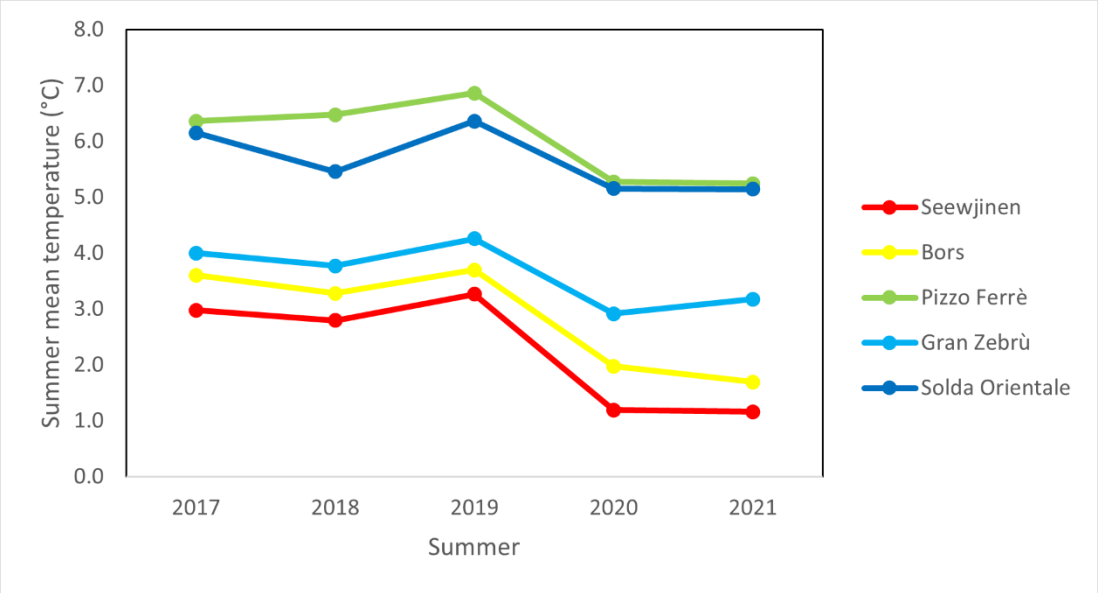

Figure 3 Summer mean (JJA) air temperatures extrapolated to the median glacier elevation of the glaciers from 2017 to 2021.

Precipitation measured at the closest available stations show that the highest precipitation occur in Alagna Miniere (average of 1288 mm), while the lowest at Passo del Moro (average of 760 mm) (Table 3). At the three glaciers in the Central Alps minimum precipitation occurred in the hydrological year 2017/2018, while maximum in the 2019/2020 (Fig. 4, Table 3). Differently, at the other two glaciers in the Western Alps precipitation follow different trends, with a maximum at both in the 2017/2018 hydrological year, while the minimum occurred in different years (Fig. 4, Table 3).

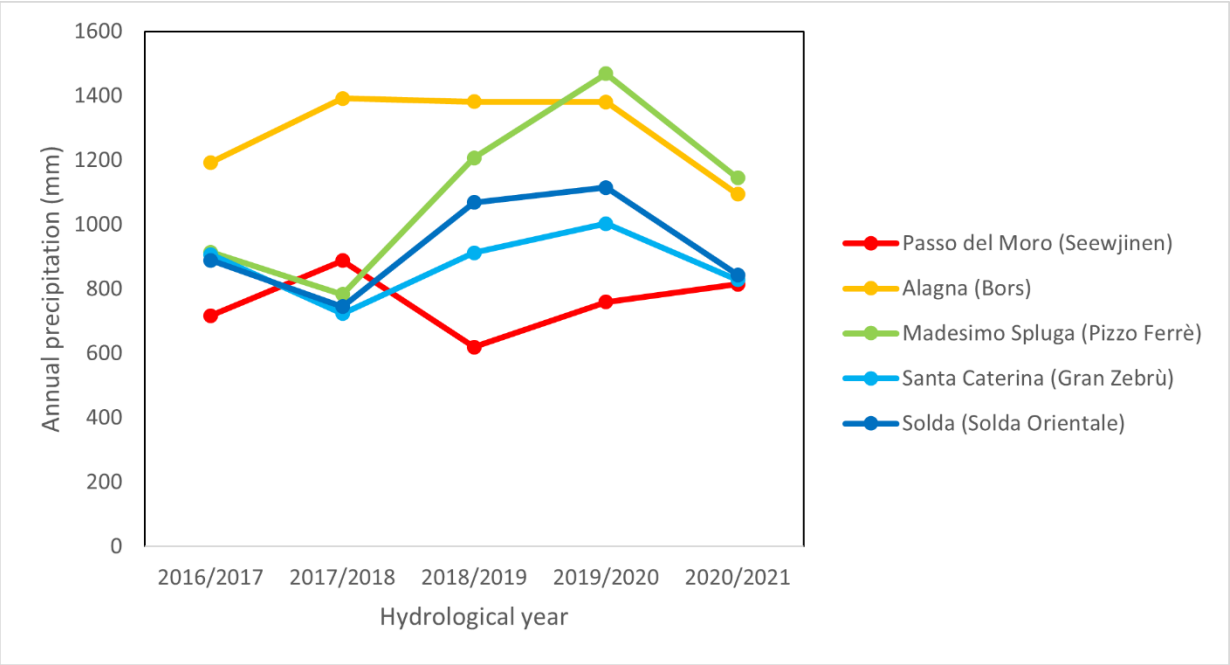

Figure 4 Annual (hydrological year) precipitation (mm) registered at the five AWS from October 2016 to September 2021.

Table 3 Annual (hydrological year) precipitation (mm) registered at the five AWS from October 2016 to September 2021 and mean annual value of the entire period.

Hydrological year	**Santa Caterina Valfurva (Gran Zebrù)**	**Alagna Miniere (Bors)**	**Solda (Solda Orientale)**	**Madesimo Spluga (Pizzo Ferrè)**	**Passo del Moro (Seewjinen)**
2016/2017	907	1193	889	914	717
2017/2018	723	1392	746	783	888
2018/2019	912	1382	1069	1208	619
2019/2020	1002	1380	1115	1468	759
2020/2021	829	1094	844	1144	815
Mean	875	1288	932	1104	760

4.2. Topographic parameters

Two of the glaciers have a southern exposition (Bors and Gran Zebrù glaciers), while three of them have a northern exposition (Seewjinen, Pizzo Ferrè and Solda glaciers) (Table 4). The glaciers have mean elevations ranging between 2834 m a.s.l. (Pizzo Ferrè glacier) and 3413 m a.s.l. (Bors glacier). The minimum elevation is reached at Solda glacier, where the glacier front reaches 2662 m a.s.l., while the maximum is reached at Bors glacier (3713 m a.s.l.). All the glaciers have similar mean aspects between 19 and 22 degrees, except Solda glacier that is slightly steeper (27 °) (Table 4). The potential annual solar radiation received by the glaciers ranges between 979998 (at Solda Orientale glacier) and 1707967 Wh/m^2 (at Bors glacier).

Table 4 Topographic parameters retrieved from the digital elevation models for each glacier. Aspect, mean slope (degrees), minimum, maximum, mean and median elevation (m a.s.l.) and potential annual solar radiation 2021 (Wh/m^2) are reported.

			Elevation (m a.s.l.)				
	Aspect	**Mean slope (deg)**	**Min**	**Max**	**Mean**	**Median**	**Potential annual solar radiation 2021 (Wh/m^2)**
Bors	S	22	3147	3713	3413	3411	1707967
Seewjinen	N	19	2768	3243	3007	3011	1179822
Pizzo Ferrè	NE	21	2671	3024	2834	2831	1095892
Gran Zebrù	SE	21	3047	3420	3202	3200	1392031
Solda	N	27	2662	3366	2993	2985	979998

4.3. Glacier area

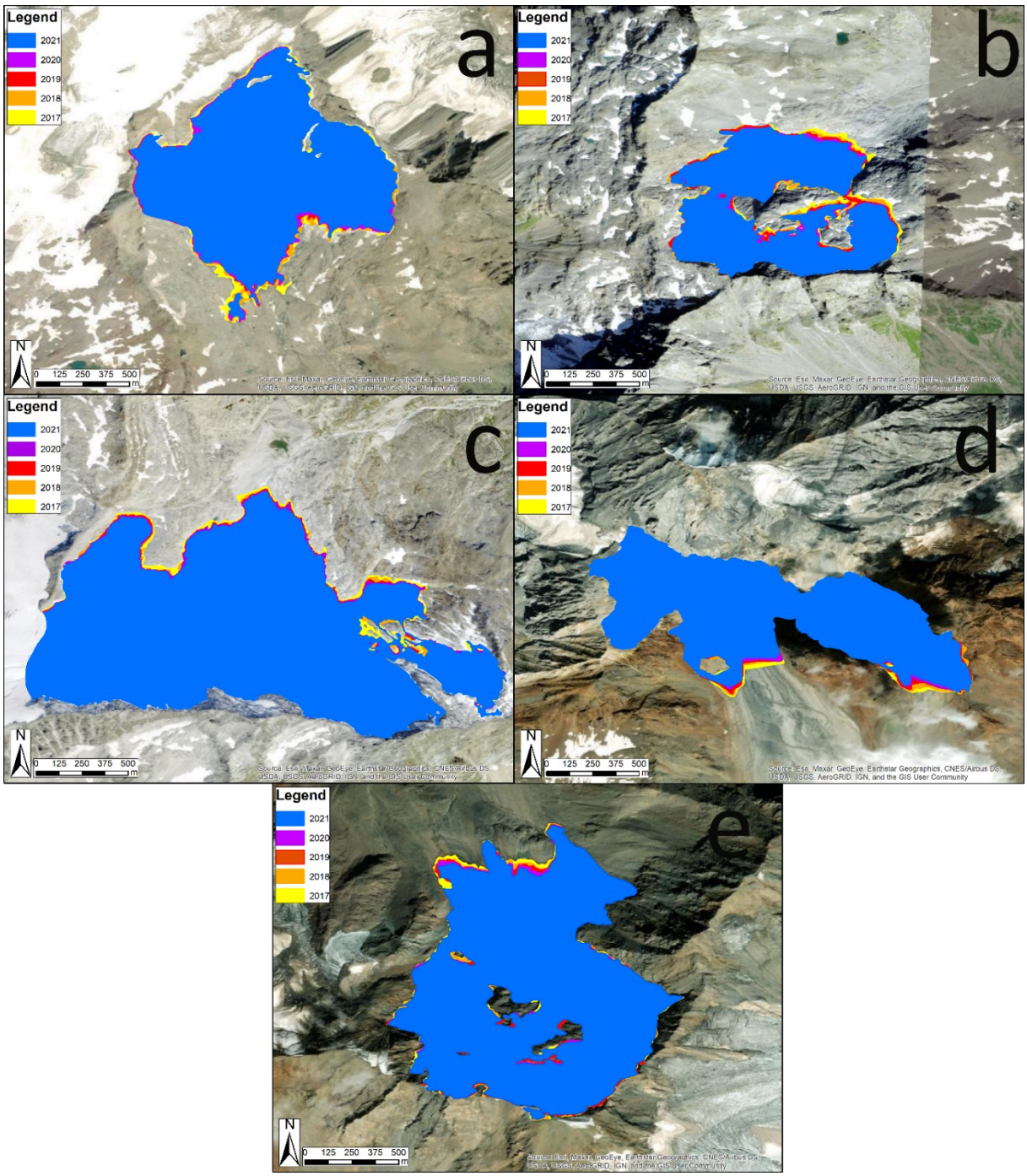

Figure 5 Surface area covered by the glaciers from 2017 to 2021: a) Bors glacier; b) Seewjinen glacier; c) Pizzo Ferrè glacier; d) Gran Zebrù glacier; e) Solda orientale glacier. Basemap: Esri World Imagery.

Glacier mapping on the Planetscope images allowed us to retrieve the surface area of the five glaciers for each year from 2017 to 2021 (Fig. 5, Fig. 6). All the glaciers underwent an area

retreat in the considered period, with reductions between 0.029 and 0.068 km^2 (Table 5). In terms of percentage, three of them, Seewjinen, Gran Zebrù and Solda Orientale glaciers, showed an area decrease of 5%, Bors glacier of 8% and Pizzo Ferrè glacier of 14% of the initial area (Fig. 6, Table 5). The glacier that showed the strongest area reduction corresponds to the smallest one (0.445 km^2 in 2017).

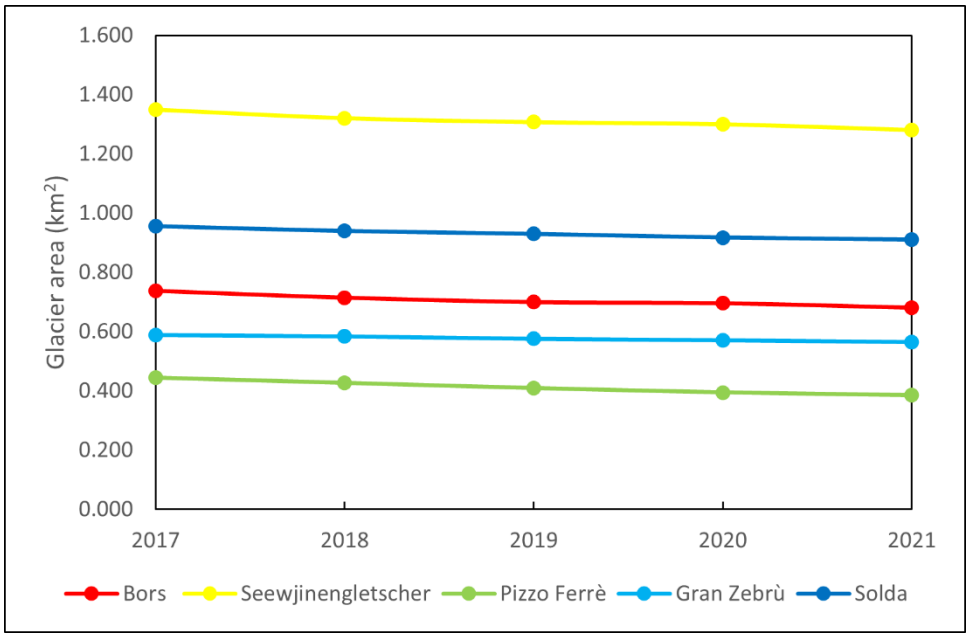

Figure 6 Area decrease of the five glaciers between 2017 and 2021.

Considering all the glaciers, the area decreased most in 2018 (-0.094 km^2) while the lowest decrease occurred in 2020 (-0.045 km^2).

Table 5 Glacier area (km^2) of the five glaciers from 2017 to 2021, total area decrease (km^2) and percentage of decrease (%).

Area km^2	**Bors**	**Seewjinen**	**Pizzo Ferrè**	**Gran Zebrù**	**Solda**
2017	0.738 ±0.009	1.349 ±0.015	0.445 ±0.009	0.614 ±0.009	0.957 ±0.012
2018	0.715 ±0.010	1.321 ±0.016	0.427 ±0.009	0.606 ±0.009	0.940 ±0.012
2019	0.700 ±0.010	1.307 ±0.016	0.410 ±0.010	0.597 ±0.009	0.930 ±0.013
2020	0.696 ±0.010	1.300 ±0.016	0.395 ±0.010	0.591 ±0.009	0.918 ±0.013
2021	0.681 ±0.010	1.281 ±0.016	0.385 ±0.010	0.585 ±0.009	0.910 ±0.013
Total area decrease (km^2)	0.056	0.068	0.061	0.029	0.047
% decrease	8	5	14	5	5

4.3. Equilibrium line altitude (ELA)

The five glaciers showed different effective ELAs in the study period (Fig. 7). On average, the lowest ELA was found at Pizzo Ferrè glacier (2955 m a.s.l.), while the highest at Bors glacier (3442 m a.s.l.), the other three glaciers had intermediate ELAs: 3040 m Seewjinen, 3096 m Solda Orientale and >3301 m Gran Zebrù. At Gran Zebrù glacier in 2017 and 2018 almost no snow from the current year was present at the end of the ablation season, with only few sparse snow patches and therefore a snow line was not drawn(Fig. 7d).

The annual ELAs showed a temporal variability in the different years. The highest ELA was found at almost every glacier in 2018, except at Bors in 2019 and the lowest was found in 2019 at Pizzo Ferrè and Gran Zebrù, 2020 at Seewjinen and Solda and 2021 at Bors (Fig. 7e). The evolution of the ELA follows different trends at the glaciers, with similar patterns at Seewjinen and Pizzo Ferrè glaciers and at Gran Zebrù and Solda glaciers, while Bors glaciers differs from all the others (Fig. 7e). The maximum range of ELAs occurred at Solda Orientale glaciers, with

a difference between the highest and lowest ELA (respectively in 2018 and 2020) of 232 m (Fig. 7e). Differently, at the other glaciers the interannual variability was always ≤100 m.

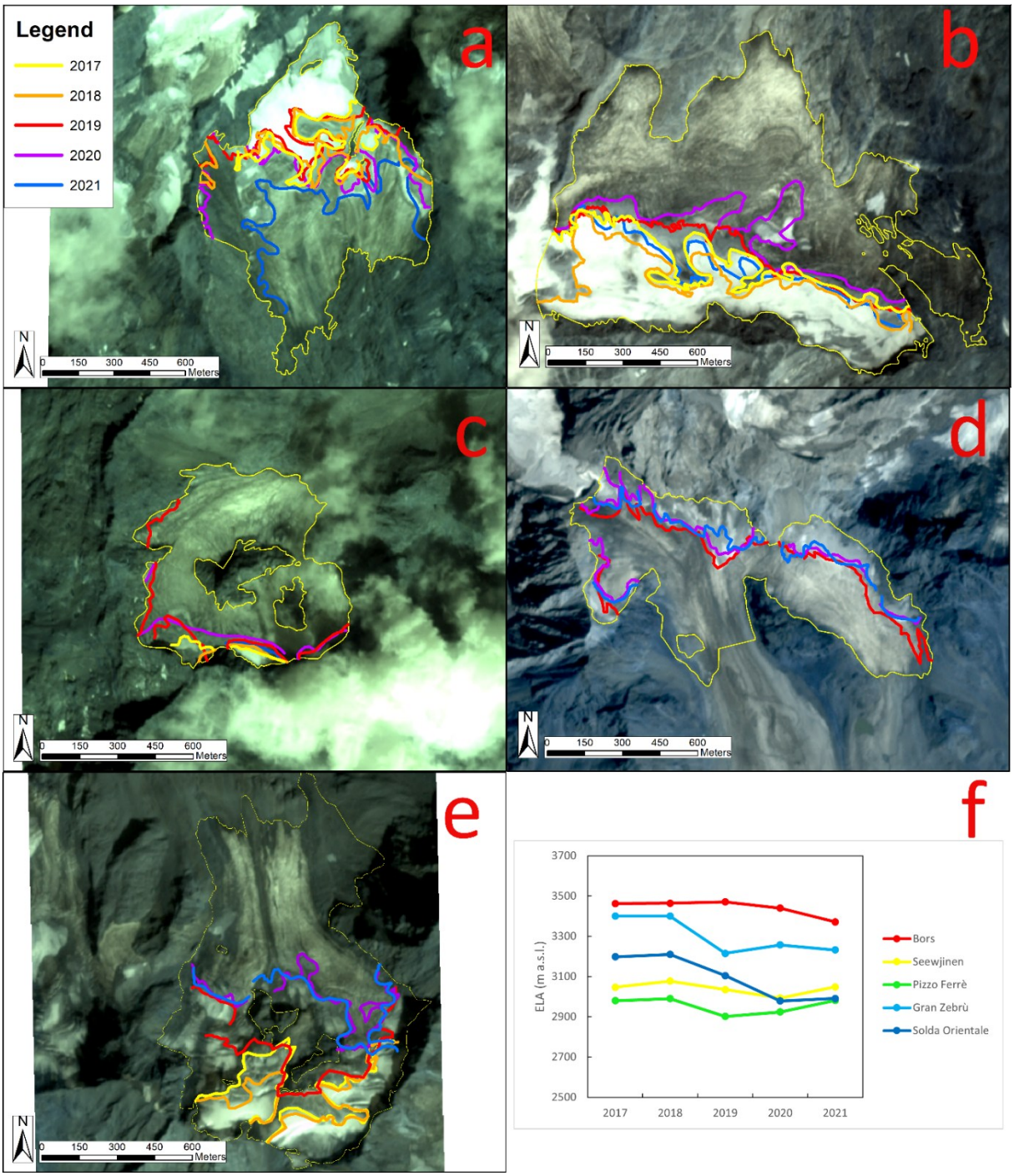

Figure 7 Annual equilibrium line altitudes between 2017 and 2021 for: a) Bors glacier; b) Seewjinen glacier; c) Pizzo Ferrè glacier; d) Gran Zebrù glacier; e) Solda Orientale glacier; f) temporal variability of annual ELAs for the five glaciers.

4.4. Image classification

Here we report the image classification results of the two glaciers (Gran Zebrù and Seewjinen glaciers) as preliminary results. Although PlanetScope images are daily, a limited number of images are usable, as images with cloud cover or other problems (as band saturation on snow areas) must be discarded. Only the images where ice/debris was exposed on the glaciers were classified, as in the previous and successive images the glaciers are 100% snow covered. A total number of 65 images were classificable for Gran Zebrù glacier and 60 for Seewjinen glacier.

Ice/debris surfaces start being exposed earlier at Seewjinen glacier (between 04 June and 02 July in the different years) than at Gran Zebrù glacier (between 26 June and 17 July). The ablation season usually ends at the end of September at both glaciers. Exceptions are 2017, when it ended earlier: on 29 August at Gran Zebrù and 7 September at Seewjinen and later at Gran Zebrù in 2018, when it lasted until 26 October (Figure 8). After snow depletion starts, snow cover decreases and ice and debris surfaces increase, with different trends at the different glaciers and in the different years (Figure 8). One or more snowfall events usually occur during the ablation season at both glaciers. At Seewjinen glacier the snow covered area never decreased below 30%, while at Gran Zebrù it reached a minimum of 6% in September 2018.

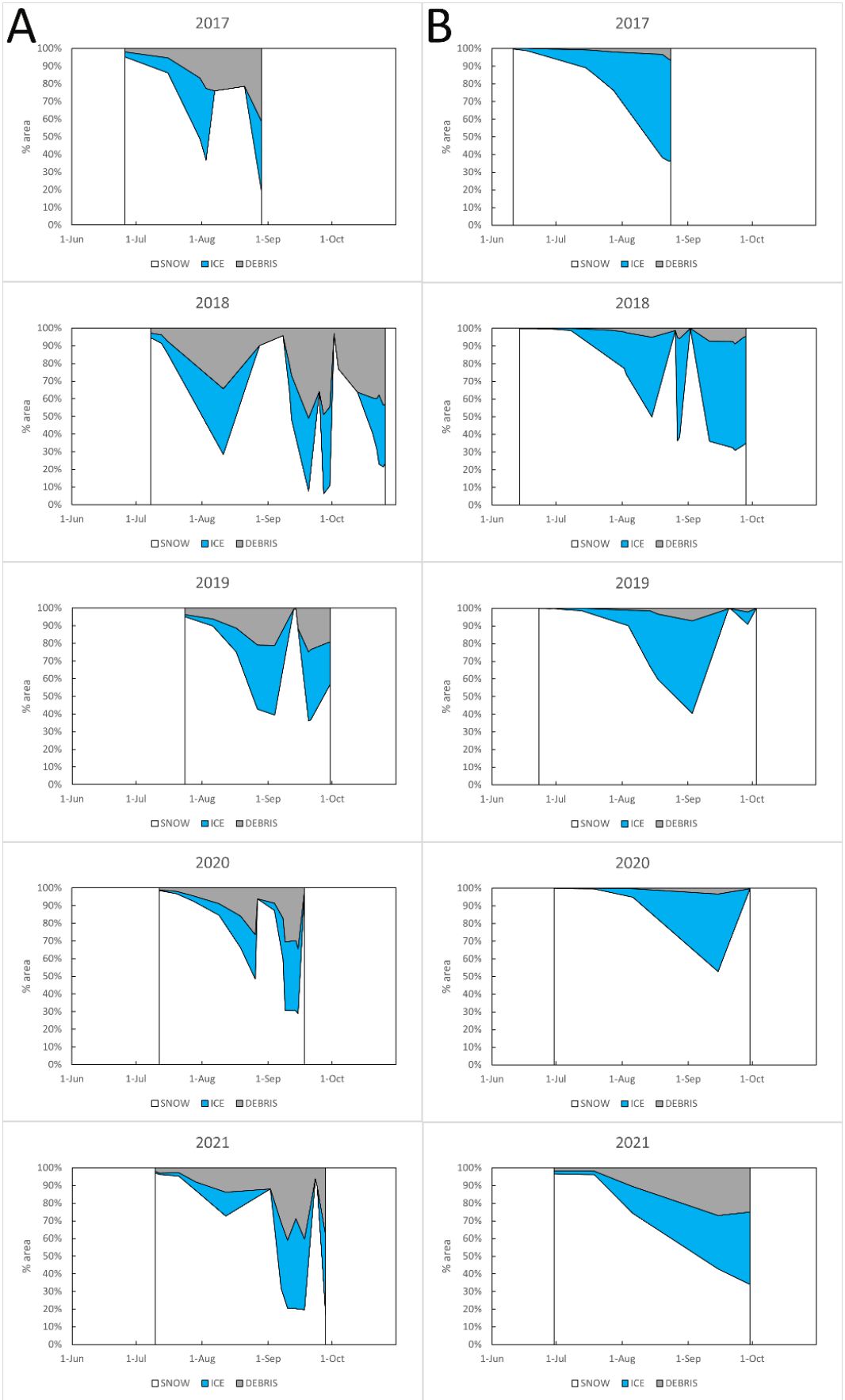

Figure 8 Evolution of the different surface types (snow, ice, debris) during the 2017-2021 ablation seasons at Gran Zebrù (A) and Seewjinen (B) glaciers.

5. Discussion

5.1. The use of PlanetScope satellite images for small glacier monitoring

The PlanetScope images offer advantages both in terms of spatial and temporal resolution in glacier monitoring. Regarding glacier mapping, we calculated small uncertainties, between 1.1 and 2.5% of the glacier area (Tab. 5). Since uncertainties in the glacier area are calculated considering possible errors of ±0.5 pixel, they would increase significantly using medium-resolution images. Among the commonly used satellite imagery, Sentinel-2 has the highest spatial resolution of 10 m, while Landsat 8 of 30 m, ten times the pixel size of PlanetScope. So for example, if we calculate the uncertainties of the glacier areas using the pixel size of the Landsat, we would obtain uncertainties between 10% and 24%.

In Figure 9, as an example, it is possible to see the different spatial detail of a PlanetScope image (3 m resolution, Fig. 9a) and a Landsat 8 image of the same glaciers (Fig. 9b) on the same day (27/08/2019).

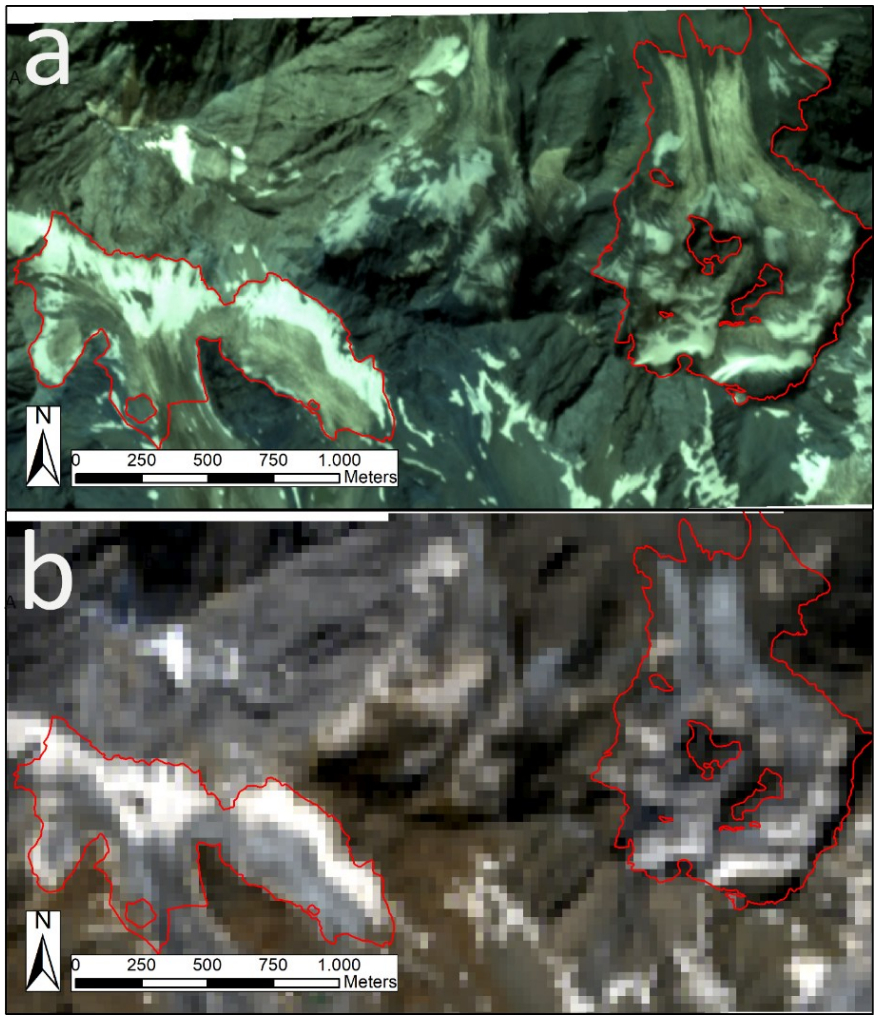

Figure 9 Satellite images of Gran Zebrù glacier and Solda Orientale glacier acquired on 27/08/2019: a) PlanetScope image; b) Landsat 8 image.

The advantages of high resolution images for small gaciers have been already demonstrated in literature, for example Fischer et al. (2014) showed that using medium-resolution satellite images can lead to a misclassification of more than 25% of the area of very small glaciers (<0.5 km^2), recommending the use of high-resolution images.

Moreover using higher resolution images for glacier mapping also enhances the visibility of the debris-covered glacier parts and permits to obtain more accurate outlines (Paul et al., 2017).

Other than the high spatial resolution, the other main advantage of using PlanetScope images is the daily revisit time. The short revisit time increases the probability of obtaining data also in regions that are frequently cloud-covered. Indeed, when mapping glaciers outlines or the ELA, cloud-free images from the end of the ablation season and with minimum snow cover are needed, but when using other satellites with lower temporal resolution it is often not possible to obtain images from a specific period with these conditions (Paul et al., 2020). As the revisit time of Sentinel 2 is 5 days, and it's 16 days for Landsat, the amount of available data is lower than for PlanetScope. Moreover,thanks to their daily availability, PlanetScope images can be used to monitor the glacier surface at sub-seasonal time scales.

Although Planet's satellites are commercial, a limited and non-commercial access to data is offered through the Education and Research Program for research purposes.

PlanetScope images have however some disadvantages. One is the absence of a SWIR band, not permitting the automated mapping of glaciers using band ratio methods. Another problem is pixels saturation occurring principally on snow areas, already reported by Ghuffar (2018) and Aati & Avouac, (2020). But the NIR band is usually not affected by this problem and could be used alone for some applications. In addition, the first PlanetScope satellites were launched in 2016 and so long timeseries of data are not yet available.

5.2. Glacier evolution and relation to topographic and meteorological parameters

Considering the aspect of the glaciers, glaciers with a northern aspect showed on average a slightly higher area change (-8%) than southern-exposed glaciers (-6%). This is in agreement to what already reported by Linsbauer et al. (2021) in the Swiss Alps, explaining that smaller area changes are experienced by the south-facing glaciers due to the fact that they are located at higher elevations, they are less sensitive to temperature changes, as they are usually colder. Also in our case the southern-exposed glaciers are located at higher elevations with an average median elevation of 3306 m a.s.l., more than 350 m higher than the average of northern exposed glaciers, being 2942 m a.s.l. and with the average minimum elevation reached by southern exposed glaciers being 3097 m a.s.l., while 2700 m a.s.l. by northern exposed.

Dividing the glaciers in size classes (0.10–0.5 km^2, 0.5–1 km^2, 1–2 km^2) (introduced by Paul et al., 2004) there is a decrease of the percentage area change at increasing size class, with -13.6% in the class 0.10–0.5 km^2, -5.7% for 0.5–1 km^2 and -5.0% for 1–2 km^2. Considering the single glaciers, there's a negative correlation between the initial area of 2017 and the percentage of area change, but not significant ($r=-0.64$, $p>0.05$), while no relationship was found between the area change and the mean slope of the glaciers. In our sample, Pizzo Ferrè glacier is the one that lost the larger relative area (-14%) and is both the smallest, covering an area of 0.445 km^2 in 2017 and thus being considered a very small glacier (<0.5 km^2), and the one having the lowest median elevation (2831 m a.s.l.). The tendency towards an increasing percentage area retreat with decreasing glacier size had already been reported in the Alps, for example by Carturan et al. (2013a), D'Agata et al. (2014), Smiraglia et al. (2015) and Linsbauer et al. (2021). Differently, the resilience of some very small glaciers was reported in some areas of the Alps, as in the Julian Alps (Eastern Italian Alps) (by Carturan et al.,2013b; Colucci, 2016;

Colucci et al., 2021 and De Marco et al.,2020) and in the Orobie (Central Italian Alps) (by Scotti et al., 2014), zones characterized by high mean annual precipitation.

Regarding the relations with climate, also between the mean air temperature of the entire period and the percentage of area change there's a positive but not significant correlation ($r=0.68$; $p>0.05$), with the glaciers located where higher temperatures occur losing more area than the others with lower temperatures. The non-significance of the correlation is probably related to the small number of glaciers considered.

If we consider the two southern-exposed glaciers, Gran Zebrù and Bors glaciers, the first showed a lower area decrease, losing the 5% of the area respect to the 8% lost by the second. Despite that Gran Zebrù has a lower median elevation (ca. 200 m respect to Bors), its mean annual air temperatures is lower (Tab. 2). Moreover, other factors could concur to reduce the retreat of Gran Zebrù, as the presence of rockwalls surrounding the glacier shadowing it and reducing the radiation received and favouring accumulation by avalanching, or the extensive supraglacial debris cover present on the western tongue. It is known that these factors (avalanches, shadow effects and debris cover) lead to accumulation and ablation anomalies on small glaciers (Capt et al., 2016).

The total measured area changes of the five glaciers, showed an area loss of 6.3% of the initial area between 2017 and 2021, with a rate of decrease of about -1.6% per year, are in agreement with other studies carried out in the alpine region, although they refer to previous periods respect to the one investigated in this study. For example, D'Agata et al. (2018) reported a mean area change of -1.6% per year between 1991 and 2007 for the glaciers of the Sondrio Province (Italy) (to which Pizzo Ferrè glacier and Gran Zebrù glacier belong). Knoll & Kerschner (2009) found an area change of -1.4% per year in South Tirol (Italy) and in particular of -1.1% in the Ortles Cevedale group (to which Solda Orientale glacier belong) in the period

1983-2006. Huss et al. (2012) found an area decrease of -1.7% from 1999 to 2008 for 36 glaciers of the Swiss Alps. Paul et al. (2020) reported an area loss of -15% (-1.3% per year) from 2003 to 2015/2016 for glaciers in the Alps.

Regarding the equilibrium line altitude, we found a significant correlation between the potential annual solar radiation received by the glaciers and their average ELA (r=0.90; p=0.039) (Fig. 10). No statistically significant correlation was found between the average ELA and average annual mean temperature, average summer mean temperature (June-August), average of the total annual precipitation or average of the total precipitation in the accumulation season (October-May), suggesting that the spatial variability of the ELA is most influenced by the topographic factors that determine the solar radiation received by glaciers than by climatic factors. In fact, the effective ELA is affected not only by climate but also by the local topoclimatic factors and therefore it differs from the regional environmental ELA (Žebre et al., 2021).

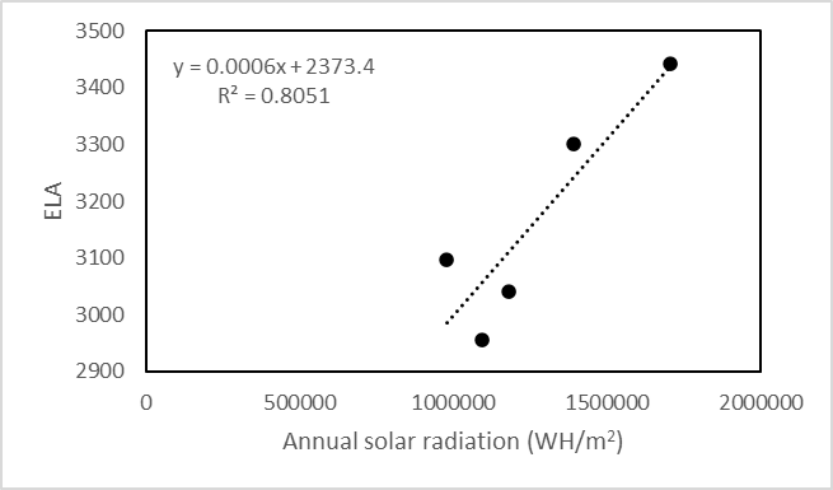

Figure 10 Scatterplot of annual solar adiation (Wh/m^2) and mean ELA of the five glaciers.

The average ELA of the glaciers is also strongly positively correlated with their median (r=0.98; p=0.003) and mean elevation (r=0.99; p=0.002). This result is similar to what previously

reported in other studies, finding a correlation between ELA and mean elevation (e.g. Leonard et al., 2003) or median elevation (e.g. Braithwaite & Raper, 2009).

The average ELA of the northern exposed glaciers was 3031 m a.s.l., while the average ELA of the southern exposed ones was 3371 m a.s.l. This result is comparable to what reported by Carturan et al. (2013a), finding an average snowline altitude shortly before the end of the ablation season of 3094 m a.s.l. for northern exposed glaciers and 3335 for southern exposed ones in the Ortles-Cevedale for the years 1987 and 2009.

At all the glaciers the ELA showed an interannual variability (Fig. 7). Due to the small altitudinal range of small glaciers, the variations in the ELA have important impact on glacier mass balance, as they rapidly change the proportion of accumulation and ablation areas (Capt et al., 2016). Analysing what causes the temporal variability of the ELA, we tested possible correlations between the annual ELA and mean annual air temperature, mean summer temperature, mean temperature of the ablation season (June-September), mean temperature of July and August (the warmest months) annual precipitation, winter precipitation and precipitation in the accumulation season (October-May). Only for Bors glacier a statistically significant correlation between mean annual air temperature and the ELA ($r=0.96$; $p=0.009$) was found and between the mean temperature of July and August and the ELA ($r=0.99$; $p=0.001$), suggesting a predominance of temperature changes influencing the ELA at this glacier. Differently, at the other glaciers a combined effect of summer temperatures and precipitation during the accumulation season concur to the interannual variability of the ELA (e.g. Scotti & Brardinoni, 2018), but also, as explained before, others factors influence it, as wind-drifting, snow avalanching, that influence accumulation (Kuhn et al., 1995), or possibly also the cloud cover.

Also in this case, it must be considered that the absence of significancy of the correlations is probably affected by the small sample size (5 years). Extending the length of the timeseries, using remote sensing images of satellites operative before 2017, and increasing the number of glaciers investigated could improve the understanding of the topographic and climatic factors that influence the evolution of small glaciers.

6. Conclusions

In this paper we showed that PlanetScope satellite images, thanks to their high temporal (daily) and spatial (3 m) resolution are valuable for small glaciers monitoring, offering different advantages respect to medium-resolution satellite images. We were able to retrieve the glacier area of five small glaciers in the Alps with low uncertainties (1.1-2.5% of the area) and to see their evolution from 2017 to 2021. They lost between 5 and 14% of the area, with the smallest glacier being the one that retreated most. As expected the northern-exposed glaciers are located at lower elevations (average elevation of 2942 m a.s.l.) than the southern-exposed (average 3306 m a.s.l.) and also their ELA is located about 340 m lower on average. The mean ELA of the glaciers is significantly correlated with the mean/median altitude and also with the annual potential solar radiation. The ELAs showed interannual variability, being probably influenced both by temperatures and precipitation, with different temporal trends at the different glaciers. Monitoring the evolution of the glacier surface of two of the glaciers during the ablation season, we saw differences in the length of the ablation season and in the evolution of the snow cover. PlanetScope images, with their daily availability offer an increased number of images respect to other commonly used satellites, allowing to monitor glacier not only annually but also sub-seasonally. In the future, extending the length of the

timeseries to more than five years would improve the understanding of the climatic and topographic factors influencing the evolution of small glaciers.

Acknowledgements

We are thankful to Planet Labs for providing access to the satellite images used in this study through the Education and Research program. We also thank ARPA Piemonte, ARPA Lombardia and Provincia autonoma di Bolzano - Alto Adige for providing meteorological data and Geoportale della Lombardia, Geoportale Alto Adige, Geoportale Piemonte and Federal Office of Topography swisstopo for providing the digital elevation models.

References

Aati, S., & Avouac, J. P. (2020). Optimization of optical image geometric modeling, application to topography extraction and topographic change measurements using PlanetScope and SkySat imagery. Remote Sensing, 12(20), 3418.

Anderson, R. S., Anderson, L. S., Armstrong, W. H., Rossi, M. W., & Crump, S. E. (2018). Glaciation of alpine valleys: The glacier–debris-covered glacier–rock glacier continuum. Geomorphology, 311, 127-142.

Auer, I., Böhm, R., Jurkovic, A., Lipa, W., Orlik, A., Potzmann, R., ... & Nieplova, E. (2007). HISTALP—historical instrumental climatological surface time series of the Greater Alpine Region. International Journal of Climatology: A Journal of the Royal Meteorological Society, 27(1), 17-46. https://doi.org/10.1002/joc.1377

Braithwaite, R. J., & Raper, S. C. B. (2009). Estimating equilibrium-line altitude (ELA) from glacier inventory data. Annals of Glaciology, 50(53), 127-132.

Capt, M., Bosson, J. B., Fischer, M., Micheletti, N., & Lambiel, C. (2016). Decadal evolution of a very small heavily debris-covered glacier in an Alpine permafrost environment. Journal of Glaciology, 62(233), 535-551.

Carturan, L., Filippi, R., Seppi, R., Gabrielli, P., Notarnicola, C., Bertoldi, L., ... & Dalla Fontana, G. (2013a). Area and volume loss of the glaciers in the Ortles-Cevedale group (Eastern Italian Alps): controls and imbalance of the remaining glaciers. The Cryosphere, 7(5), 1339-1359.

Carturan, L., Baldassi, G. A., Bondesan, A., Calligaro, S., Carton, A., Cazorzi, F., ... & Tarolli, P. (2013b). Current behaviour and dynamics of the lowermost Italian glacier (Montasio Occidentale, Julian Alps). Geografiska Annaler: Series A, Physical Geography, 95(1), 79-96.

Chand, P., Jain, S. K., Thakur, H. P., Kumar, S., & Sharma, M. C. (2020). Recessional pattern and surface elevation change of the Parvati Glacier, North-Western Himalaya (1965-2018) using remote sensing. International Journal of Remote Sensing, 41(24), 9360-9392.

Colucci, R. R. (2016). Geomorphic influence on small glacier response to post-Little Ice Age climate warming: Julian Alps, Europe. Earth Surface Processes and Landforms, 41(9), 1227-1240.

Colucci, R. R., Žebre, M., Torma, C. Z., Glasser, N. F., Maset, E., Del Gobbo, C., & Pillon, S. (2021). Recent increases in winter snowfall provide resilience to very small glaciers in the Julian Alps, Europe. Atmosphere, 12(2), 263.

D'Agata, C., Bocchiola, D., Maragno, D., Smiraglia, C., & Diolaiuti, G. A. (2014). Glacier shrinkage driven by climate change during half a century (1954–2007) in the Ortles-Cevedale

group (Stelvio National Park, Lombardy, Italian Alps). Theoretical and applied climatology, 116(1), 169-190.

D'Agata, C., Bocchiola, D., Soncini, A., Maragno, D., Smiraglia, C., & Diolaiuti, G. A. (2018). Recent area and volume loss of Alpine glaciers in the Adda River of Italy and their contribution to hydropower production. Cold Regions Science and Technology, 148, 172-184.

De Marco, J., Carturan, L., Piermattei, L., Cucchiaro, S., Moro, D., Dalla Fontana, G., & Cazorzi, F. (2020). Minor Imbalance of the Lowermost Italian Glacier from 2006 to 2019. Water, 12(9), 2503.

Frei, C., & Schär, C. (1998). A precipitation climatology of the Alps from high-resolution rain-gauge observations. International Journal of Climatology: A Journal of the Royal Meteorological Society, 18(8), 873-900.

Ghuffar, S. (2018). DEM generation from multi satellite PlanetScope imagery. Remote Sensing, 10(9), 1462.

Huss, M., Hock, R., Bauder, A., & Funk, M. (2012). Conventional versus reference-surface mass balance. Journal of Glaciology, 58(208), 278-286.

Huss, M., & Fischer, M. (2016). Sensitivity of very small glaciers in the Swiss Alps to future climate change. Frontiers in Earth Science, 4, 34.

Immerzeel, W. W., Petersen, L., Ragettli, S., & Pellicciotti, F. (2014). The importance of observed gradients of air temperature and precipitation for modeling runoff from a glacierized watershed in the Nepalese Himalayas. Water Resources Research, 50(3), 2212-2226.

Isotta, F. A., Frei, C., Weilguni, V., Perčec Tadić, M., Lassegues, P., Rudolf, B., ... & Vertačnik, G. (2014). The climate of daily precipitation in the Alps: development and analysis of a high-

resolution grid dataset from pan-Alpine rain-gauge data. International Journal of Climatology, 34(5), 1657-1675.

Kääb, A., Leinss, S., Gilbert, A., Bühler, Y., Gascoin, S., Evans, S. G., ... & Yao, T. (2018). Massive collapse of two glaciers in western Tibet in 2016 after surge-like instability. Nature Geoscience, 11(2), 114-120.

Knoll, C., & Kerschner, H. (2009). A glacier inventory for South Tyrol, Italy, based on airborne laser-scanner data. Annals of Glaciology, 50(53), 46-52.

Kuhn, M. (1995). The mass balance of very small glaciers. Zeitschrift für Gletscherkunde und Glazialgeologie, 31(1), 171-179.

Leonard, K. C., & Fountain, A. G. (2003). Map-based methods for estimating glacier equilibrium-line altitudes. Journal of Glaciology, 49(166), 329-336.

Linsbauer, A., Huss, M., Hodel, E., Bauder, A., Fischer, M., Weidmann, Y., Bärtschi, H., & Schmassmann, E. (2021). The New Swiss Glacier Inventory SGI2016: From a Topographical to a Glaciological Dataset. Frontiers in Earth Science, 9.

Millan, R., Mouginot, J., Rabatel, A., Jeong, S., Cusicanqui, D., Derkacheva, A., & Chekki, M. (2019). Mapping surface flow velocity of glaciers at regional scale using a multiple sensors approach. Remote Sensing, 11(21), 2498.

Paul, F., Kääb, A., Maisch, M., Kellenberger, T., & Haeberli, W. (2004). Rapid disintegration of Alpine glaciers observed with satellite data. Geophysical research letters, 31(21).

Paul, F., Barrand, N. E., Baumann, S., Berthier, E., Bolch, T., Casey, K., ... & Winsvold, S. (2013). On the accuracy of glacier outlines derived from remote-sensing data. Annals of Glaciology, 54(63), 171-182.

Paul, F., Bolch, T., Briggs, K., Kääb, A., McMillan, M., McNabb, R., ... & Wuite, J. (2017). Error sources and guidelines for quality assessment of glacier area, elevation change, and velocity products derived from satellite data in the Glaciers_cci project. Remote Sensing of Environment, 203, 256-275.

Paul, F., Rastner, P., Azzoni, R. S., Diolaiuti, G., Fugazza, D., Le Bris, R., Nemec, J., Rabatel, A., Ramusovic, M., Schwaizer, G., Smiraglia, C. (2019). Glacier inventory of the Alps from Sentinel-2, shape files. PANGAEA, https://doi.org/10.1594/PANGAEA.909133. Supplement to: Paul, F., Rastner, P., Azzoni, R. S., Diolaiuti, G., Fugazza, D., Le Bris, R., ... & Smiraglia, C. (2020). Glacier shrinkage in the Alps continues unabated as revealed by a new glacier inventory from Sentinel-2. Earth System Science Data, 12(3), 1805-1821.

Paul, F., Rastner, P., Azzoni, R. S., Diolaiuti, G., Fugazza, D., Le Bris, R., ... & Smiraglia, C. (2020). Glacier shrinkage in the Alps continues unabated as revealed by a new glacier inventory from Sentinel-2. Earth System Science Data, 12(3), 1805-1821.

Planet (2021). Planetscope product specifications. https://assets.planet.com/docs/Planet_Combined_Imagery_Product_Specs_letter_screen.pdf

Pudełko, R., Angiel, P. J., Potocki, M., Jędrejek, A., & Kozak, M. (2018). Fluctuation of glacial retreat rates in the eastern part of Warszawa Icefield, King George Island, Antarctica, 1979–2018. Remote sensing, 10(6), 892.

Qayyum, N., Ghuffar, S., Ahmad, H. M., Yousaf, A., & Shahid, I. (2020). Glacial lakes mapping using multi satellite PlanetScope imagery and deep learning. ISPRS International Journal of Geo-Information, 9(10), 560.

Rabatel, A., Dedieu, J. P., & Vincent, C. (2005). Using remote-sensing data to determine equilibrium-line altitude and mass-balance time series: validation on three French glaciers, 1994–2002. Journal of glaciology, 51(175), 539-546.

Racoviteanu, A. E., Paul, F., Raup, B., Khalsa, S. J. S., & Armstrong, R. (2009). Challenges and recommendations in mapping of glacier parameters from space: results of the 2008 Global Land Ice Measurements from Space (GLIMS) workshop, Boulder, Colorado, USA. Annals of Glaciology, 50(53), 53-69.

Racoviteanu, A. E., Rittger, K., & Armstrong, R. (2019). An automated approach for estimating snowline altitudes in the Karakoram and eastern Himalaya from remote sensing. Frontiers in Earth Science, 7, 220.

Ragettli, S., Bolch, T., & Pellicciotti, F. (2016). Heterogeneous glacier thinning patterns over the last 40 years in Langtang Himal, Nepal. The Cryosphere, 10(5), 2075-2097.

Scotti, R., Brardinoni, F., & Crosta, G. B. (2014). Post-LIA glacier changes along a latitudinal transect in the Central Italian Alps. The Cryosphere, 8(6), 2235-2252.

Scotti, R., & Brardinoni, F. (2018). Evaluating millennial to contemporary time scales of glacier change in Val Viola, Central Italian Alps. Geografiska Annaler: Series A, Physical Geography, 100(4), 319-339.

Shaw, T. E., Ulloa, G., Farías-Barahona, D., Fernandez, R., Lattus, J. M., & McPhee, J. (2021). Glacier albedo reduction and drought effects in the extratropical Andes, 1986–2020. Journal of Glaciology, 67(261), 158-169

Shukla, A., Gupta, R. P., & Arora, M. K. (2009). Estimation of debris cover and its temporal variation using optical satellite sensor data: a case study in Chenab basin, Himalaya. Journal of Glaciology, 55(191), 444-452.

Smiraglia, C., Azzoni, R. S., D'Agata, C. A. R. L. O., Maragno, D., Fugazza, D., & Diolaiuti, G. A. (2015). The evolution of the Italian glaciers from the previous data base to the New Italian Inventory. Preliminary considerations and results. Geografia Fisica e Dinamica Quaternaria, 38(1), 79-87.

Sommer, C., Malz, P., Seehaus, T. C., Lippl, S., Zemp, M., & Braun, M. H. (2020). Rapid glacier retreat and downwasting throughout the European Alps in the early 21 st century. Nature communications, 11(1), 1-10.

Steiner, J. F., Kraaijenbrink, P. D., Jiduc, S. G., & Immerzeel, W. W. (2018). Brief communication: The Khurdopin glacier surge revisited–extreme flow velocities and formation of a dammed lake in 2017. The Cryosphere, 12(1), 95-101.

Tarca, G., & Guglielmin, M. (2022). Using ground-based thermography to analyse surface temperature distribution and estimate debris thickness on Gran Zebrù glacier (Ortles-Cevedale, Italy). Cold Regions Science and Technology, 103487.

Ye, B. S., Ding, Y. J., & Liu, C. H. (2001). Response of valley glaciers in various sizes and their runoff to climate change. J. Glaciol. Geocryol, 23(2), 103-110.

Žebre, M., Colucci, R. R., Giorgi, F., Glasser, N. F., Racoviteanu, A. E., & Del Gobbo, C. (2021). 200 years of equilibrium-line altitude variability across the European Alps (1901− 2100). Climate Dynamics, 56(3), 1183-1201.

Zemp, M. (2006). Glaciers and climate change: spatio-temporal analysis of glacier fluctuations in the European Alps after 1850 (Doctoral dissertation, University of Zurich).

6. Conclusions

In this thesis, different remote sensing applications were used to monitor and study the cryosphere. Snow cover and glaciers were investigated in different case studies, both in Antactic and Alpine environments, that are among the most impacted by climate change. Our results showed that both snow cover and the glacier surfaces can be characterized by a high spatial variability, can evolve rapidly and are strictly related to climate and its changes. It is therefore of primary importance their monitoring to understand their current state and their possible future evolution. In order to capture their variability, techniques that can investigate them at high spatial and/or temporal resolution are often needed. In this context, close-range and high-resolution satellite remote sensing techniques used in these case studies proved to be useful to capture this spatial and temporal variability and to improve our knowledge about snow cover and glaciers state and evolution. In particular:

- In the case study (1) we showed that snow cover can have a really heterogeneous distribution even inside a small (~15x20 m) and almost flat area, being influenced by the microtopography and by winds and its temporal evolution it is strictly correlated to air temperatures, suggesting that a future air warming could impact it. Time-lapse photography capturing daily images of multiple stakes can capture this variability and permits to obtain snow depth time series with high accuracy, while measuring snow depth at a single point would not be representative.
- In the case study (2) we used for the first time ground-based thermal imaging to estimate debris thickness on a glacier. We showed that surface temperatures and debris thicknesses can have an high spatial variability on a glacier. We demonstrated that ground-based thermal imaging can provide very high-resolution maps of glacier

surface temperatures and of debris thickness, that can be used for the estimation of glacier ablation, with a spatial resolution more suitable than that offered by satellite thermal data, especially for glaciers with a small area and with a heterogeneous surface.

- In the case study (3) we showed that the sparse debris cover on a glacier can evolve rapidly during the ablation season, with different rates at different glaciers and in different areas of the same glacier, depending on the englacial debris concentration and on the ablation rates. We found that sparse debris impacts glacier albedo, surface temperature and ablation, with different effects depending on the quantity of debris present on the surface. The detailed evolution of the sparse debris and its impact can be study using ground-based photography and thermal-imaging, integrated with field measurements.
- In the case study (4) we showed that recently launched PlanetScope satellites with their high spatial and high temporal resolution are a useful tool for the study and monitoring of small glaciers, overcoming the limitations of conventional medium resolution satellites. We found that small Alpine glaciers are influenced in their evolution by their characteristics, as their dimensions, by their topographic characteristics, as aspect and elevation, and by climate. The relation with these variables need to be better studied in order to understand their future evolution.

6.1. Future perspectives

Regarding the case study (1), further investigation could involve the study of the impact that this high spatial and temporal variability of snow cover have on the ground thermal regime. In terms of methodology, a method that automatically detects the snow depth at each stake should be applied, in order to significantly reduce the long processing time required to measure it manually.

Regarding supraglacial debris, experiments to assess the critical thickness for the glaciers of the Ortles-Cevedale group and how it is influenced by the different lithologies and debris characteristics (as granulometry) should be carried out. In fact, as the geology of the Ortles-Cevedale group is characterized by both metamorphic rocks (of the Campo Nappe) and sedimentary rocks (of the Ortler Nappe) and they compose the supraglacial debris, it is important to investigate the different effect these different lithologies could have on the glaciers ablation, on the albedo and of the surface temperatures of the glaciers.

In addition, for the case study (2) the use of UAV instead of ground-based thermal imaging could increase the spatial resolution of the results both for the temperatures and for the debris thickness distribution. Moreover field measurement of temperatures at the same time of taking the thermal image would permit to correct the surface temperatures of the thermal images, in order to obtain more accurate absolute temperatures. Also to study the evolution of the sparse debris (case study (3)), using repeated UAV flights would help to evaluate the evolution of the sparse debris at the scale of the entire glacier instead of only at a limited number of sampling areas

For the case study (4) it should be desirable to increase the number of the investigated glaciers, as five is a small sample, and to extend the length of the timeseries to more than five

years, to better understand the role of the topographic and climatic factors influencing their evolution.

References

Auer, I., Böhm, R., Jurkovic, A., Lipa, W., Orlik, A., Potzmann, R., ... & Nieplova, E. (2007). HISTALP—historical instrumental climatological surface time series of the Greater Alpine Region. International Journal of Climatology: A Journal of the Royal Meteorological Society, 27(1), 17-46.

Azzoni, R. S., Fugazza, D., Zerboni, A., Senese, A., D'Agata, C., Maragno, D., ... & Diolaiuti, G. A. (2018). Evaluating high-resolution remote sensing data for reconstructing the recent evolution of supra glacial debris: A study in the Central Alps (Stelvio Park, Italy). Progress in Physical Geography: Earth and Environment, 42(1), 3-23.

Barry, R., & Gan, T. Y. (2011). The global cryosphere: past, present and future. Cambridge University Press.

Beniston, M. (2012). Impacts of climatic change on water and associated economic activities in the Swiss Alps. Journal of Hydrology, 412, 291-296.

Bolch, T., Buchroithner, M., Pieczonka, T., & Kunert, A. (2008). Planimetric and volumetric glacier changes in the Khumbu Himal, Nepal, since 1962 using Corona, Landsat TM and ASTER data. Journal of Glaciology, 54(187), 592-600.

Borner, A. P., Kielland, K., & Walker, M. D. (2008). Effects of simulated climate change on plant phenology and nitrogen mineralization in Alaskan arctic tundra. Arctic, Antarctic, and Alpine Research, 40(1), 27-38.

Breithaupt, B. H., & Matthews, N. A. (2001). Crossing boundaries in park management: preserving paleontological resources using photogrammetry and geographic information

systems. In 11th Conference on research and resource management in parks and on public lands: the 2001 GWS biennial conference (No. 11, pp. 62-70). The George Wright Society.

Brown, R.D., & Robinson, D.A. (2005). Snow and Snow Cover. In: Oliver, J.E. (Eds.), Encyclopedia of World Climatology. Encyclopedia of Earth Sciences Series. Springer, Dordrecht.

Brook, M. S., Hagg, W., & Winkler, S. (2013). Debris cover and surface melt at a temperate maritime alpine glacier: Franz Josef Glacier, New Zealand. New Zealand Journal of Geology and Geophysics, 56(1), 27-38.

Callaghan, T. V., Johansson, M., Brown, R. D., Groisman, P. Y., Labba, N., Radionov, V., ... & Wood, E. F. (2011). Multiple effects of changes in Arctic snow cover. Ambio, 40(1), 32-45.

Campbell, J. B., & Wynne, R. H. (2011). Introduction to remote sensing. Guilford Press.

Cannone, N., Evans, J. E., Strachan, R., & Guglielmin, M. (2006). Interactions between climate, vegetation and the active layer in soils at two Maritime Antarctic sites. Antarctic Science, 18(3), 323-333.

Cannone, N., Diolaiuti, G., Guglielmin, M., & Smiraglia, C. (2008). Accelerating climate change impacts on alpine glacier forefield ecosystems in the European Alps. Ecological Applications, 18(3), 637-648.

Carturan, L., Filippi, R., Seppi, R., Gabrielli, P., Notarnicola, C., Bertoldi, L., ... & Dalla Fontana, G. (2013a). Area and volume loss of the glaciers in the Ortles-Cevedale group (Eastern Italian Alps): controls and imbalance of the remaining glaciers. The Cryosphere, 7(5), 1339-1359.

Carturan, L., Baldassi, G. A., Bondesan, A., Calligaro, S., Carton, A., Cazorzi, F., ... & Tarolli, P. (2013b). Current behaviour and dynamics of the lowermost Italian glacier (Montasio Occidentale, Julian Alps). Geografiska Annaler: Series A, Physical Geography, 95(1), 79-96.

Chiarle, M., Iannotti, S., Mortara, G., & Deline, P. (2007). Recent debris flow occurrences associated with glaciers in the Alps. Global and Planetary Change, 56(1-2), 123-136.

Clark, D. H., Clark, M. M., & Gillespie, A. R. (1994). Debris-covered glaciers in the Sierra Nevada, California, and their implications for snowline reconstructions. Quaternary Research, 41(2), 139-153.

Colucci, R. R. (2016). Geomorphic influence on small glacier response to post-Little Ice Age climate warming: Julian Alps, Europe. Earth Surface Processes and Landforms, 41(9), 1227-1240.

Colucci, R. R., Žebre, M., Torma, C. Z., Glasser, N. F., Maset, E., Del Gobbo, C., & Pillon, S. (2021). Recent increases in winter snowfall provide resilience to very small glaciers in the Julian Alps, Europe. Atmosphere, 12(2), 263.

D'Agata, C., Bocchiola, D., Maragno, D., Smiraglia, C., & Diolaiuti, G. A. (2014). Glacier shrinkage driven by climate change during half a century (1954–2007) in the Ortles-Cevedale group (Stelvio National Park, Lombardy, Italian Alps). Theoretical and applied climatology, 116(1), 169-190.

De Marco, J., Carturan, L., Piermattei, L., Cucchiaro, S., Moro, D., Dalla Fontana, G., & Cazorzi, F. (2020). Minor Imbalance of the Lowermost Italian Glacier from 2006 to 2019. Water, 12(9), 2503.

Fyffe, C. L., Woodget, A. S., Kirkbride, M. P., Deline, P., Westoby, M. J., & Brock, B. W. (2020). Processes at the margins of supraglacial debris cover: Quantifying dirty ice ablation and debris redistribution. Earth Surface Processes and Landforms, 45(10), 2272-2290.

Franzetti, A., Pittino, F., Gandolfi, I., Azzoni, R. S., Diolaiuti, G., Smiraglia, C., ... & Ambrosini, R. (2020). Early ecological succession patterns of bacterial, fungal and plant communities along a chronosequence in a recently deglaciated area of the Italian Alps. FEMS Microbiology Ecology, 96(10), fiaa165.

Glasser, N. F., Holt, T. O., Evans, Z. D., Davies, B. J., Pelto, M., & Harrison, S. (2016). Recent spatial and temporal variations in debris cover on Patagonian glaciers. Geomorphology, 273, 202-216.

Gobiet, A., Kotlarski, S., Beniston, M., Heinrich, G., Rajczak, J., & Stoffel, M. (2014). 21st century climate change in the European Alps—A review. Science of the Total Environment, 493, 1138-1151.

Gooseff, M. N., Barrett, J. E., Doran, P. T., Fountain, A. G., Lyons, W. B., Parsons, A. N., ... & Wall, D. H. (2003). Snow-patch influence on soil biogeochemical processes and invertebrate distribution in the McMurdo Dry Valleys, Antarctica. Arctic, Antarctic, and Alpine Research, 35(1), 91-99.

Hagg, W., Brook, M., Mayer, C., & Winkler, S. (2014). A short-term field experiment on sub-debris melt at the highly maritime Franz Josef Glacier, Southern Alps, New Zealand. Journal of Hydrology (New Zealand), 153-161.

Huss, M., & Fischer, M. (2016). Sensitivity of very small glaciers in the Swiss Alps to future climate change. Frontiers in Earth Science, 4, 34.

IPCC (2019). IPCC Special Report on the Ocean and Cryosphere in a Changing Climate [H.-O. Pörtner, D.C. Roberts, V. Masson-Delmotte, P. Zhai, M. Tignor, E. Poloczanska, K. Mintenbeck, A. Alegría, M. Nicolai, A. Okem, J. Petzold, B. Rama, N.M. Weyer (eds.)]. In press.

Jiang, S., Nie, Y., Liu, Q., Wang, J., Liu, L., Hassan, J., ... & Xu, X. (2018). Glacier change, supraglacial debris expansion and glacial lake evolution in the Gyirong river basin, central Himalayas, between 1988 and 2015. Remote Sensing, 10(7), 986.

Kappen, L., Sommerkorn, M., & Schroeter, B. (1995). Carbon acquisition and water relations of lichens in polar regions—potentials and limitations. The lichenologist, 27(6), 531-545.

Kellerer-Pirklbauer, A. (2008). The supraglacial debris system at the Pasterze Glacier, Austria: spatial distribution, characteristics and transport of debris. Zeitschrift für Geomorphologie, Supplementary Issues, 3-25.

Kotwicki, V. (2009). Water balance of Earth/Bilan hydrologique de la Terre. Hydrological sciences journal, 54(5), 829-840.

Kirkbride M.P. (2011) - Debris-Covered Glaciers. In: Singh V.P., Singh P., Haritashya U.K. (eds) Encyclopedia of Snow, Ice and Glaciers. Encyclopedia of Earth Sciences Series. Springer, Dordrecht.

Linsbauer, A., Huss, M., Hodel, E., Bauder, A., Fischer, M., Weidmann, Y., Bärtschi, H., & Schmassmann, E. (2021). The New Swiss Glacier Inventory SGI2016: From a Topographical to a Glaciological Dataset. Frontiers in Earth Science, 9.

Lintz, J. and Simonett, D. S. (1897). Remote sensing of environment. Reading, Mass., Addison-Wesley Publishing.

Mattson, L. E. (1993). Ablation on debris covered glaciers: an example from the Rakhiot Glacier, Punjab, Himalaya. Intern. Assoc. Hydrol. Sci., 218, 289-296.

Mölg, N., Bolch, T., Walter, A., & Vieli, A. (2019). Unravelling the evolution of Zmuttgletscher and its debris cover since the end of the Little Ice Age. The Cryosphere, 13, 1889-1909.

Muhammad, S., Tian, L., Ali, S., Latif, Y., Wazir, M. A., Goheer, M. A., ... & Shiyin, L. (2020). Thin debris layers do not enhance melting of the Karakoram glaciers. Science of the Total Environment, 746, 141119.

Neumann, N. N., Derksen, C., Smith, C., & Goodison, B. (2006). Characterizing local scale snow cover using point measurements during the winter season. Atmosphere-Ocean, 44(3), 257-269.

Ohmura, A. (2014). Snow and Ice in the Climate System. In Haeberli, W., Whiteman, C. A., & Shroder, J. F. (Eds.). Snow and ice-related hazards, risks, and disasters. Waltham, MA: Academic Press.

Oliva, M., Navarro, F., Hrbáček, F., Hernandéz, A., Nývlt, D., Pereira, P., ... & Trigo, R. (2017). Recent regional climate cooling on the Antarctic Peninsula and associated impacts on the cryosphere. Science of the Total Environment, 580, 210-223.

Østrem, G. (1959). Ice melting under a thin layer of moraine, and the existence of ice cores in moraine ridges. Geografiska Annaler, 41(4), 228-230.

Patro, E. R., De Michele, C., & Avanzi, F. (2018). Future perspectives of run-of-the-river hydropower and the impact of glaciers' shrinkage: The case of Italian Alps. Applied Energy, 231, 699-713.

Paul F., Huggel C., & Kääb A. (2004) - Combining satellite multispectral image data and a digital elevation model for mapping debris-covered glaciers. Remote sensing of Environment, 89(4), 510-518.

Paul, F., Rastner, P., Azzoni, R. S., Diolaiuti, G., Fugazza, D., Le Bris, R., ... & Smiraglia, C. (2020). Glacier shrinkage in the Alps continues unabated as revealed by a new glacier inventory from Sentinel-2. Earth System Science Data, 12(3), 1805-1821.

Pröbstl-Haider, U., Dabrowska, K., & Haider, W. (2016). Risk perception and preferences of mountain tourists in light of glacial retreat and permafrost degradation in the Austrian Alps. Journal of Outdoor Recreation and Tourism, 13, 66-78.

Puspitarini, H. D., François, B., Zaramella, M., Brown, C., & Borga, M. (2020). The impact of glacier shrinkage on energy production from hydropower-solar complementarity in alpine river basins. Science of The Total Environment, 719, 137488.

Reznichenko, N., Davies, T., Shulmeister, J., & McSaveney, M. (2010). Effects of debris on ice-surface melting rates: an experimental study. Journal of Glaciology, 56(197), 384-394.

Ritter, F., Fiebig, M. & Muhar, A. (2012). Impacts of global warming on mountaineering: a classification of phenomena affecting the Alpine trail network. Mt. Res. Dev. 32, 4–15.

Schaefli, B., Manso, P., Fischer, M., Huss, M., & Farinotti, D. (2019). The role of glacier retreat for Swiss hydropower production. Renewable energy, 132, 615-627.

Scotti, R., Brardinoni, F., & Crosta, G. B. (2014). Post-LIA glacier changes along a latitudinal transect in the Central Italian Alps. The Cryosphere, 8(6), 2235-2252.

Scotti, R., & Brardinoni, F. (2018). Evaluating millennial to contemporary time scales of glacier change in Val Viola, Central Italian Alps. Geografiska Annaler: Series A, Physical Geography, 100(4), 319-339.

Smiraglia, C., Azzoni, R. S., D'Agata, C. A. R. L. O., Maragno, D., Fugazza, D., & Diolaiuti, G. A. (2015). The evolution of the Italian glaciers from the previous data base to the New Italian Inventory. Preliminary considerations and results. Geografia Fisica e Dinamica Quaternaria, 38(1), 79-87.

Smith, R.I.L. (1984). Terrestrial plant biology. In LAWS, R.M., ed. Antarctic ecology, vol. 1. London: Academic Press, 61–162.

Sommer, C., Malz, P., Seehaus, T. C., Lippl, S., Zemp, M., & Braun, M. H. (2020). Rapid glacier retreat and downwasting throughout the European Alps in the early 21 st century. Nature communications, 11(1), 1-10.

Stokes, C. R., Popovnin, V., Aleynikov, A., Gurney, S. D., & Shahgedanova, M. (2007). Recent glacier retreat in the Caucasus Mountains, Russia, and associated increase in supraglacial debris cover and supra-/proglacial lake development. Annals of Glaciology, 46, 195-203.

Turner, J., Barrand, N. E., Bracegirdle, T. J., Convey, P., Hodgson, D. A., Jarvis, M., ... & Klepikov, A. (2014). Antarctic climate change and the environment: an update. Polar Record, 50(3), 237-259.

Winkler, J. B., Kappen, L., & Schulz, F. (2000). Snow and ice as an important ecological factor for the cryptogams in the maritime Antarctic. Antarctic Ecosystems: Models for, 220-224.

Xie, F., Liu, S., Wu, K., Zhu, Y., Gao, Y., Qi, M., ... & Tahir, A. A. (2020). Upward Expansion of Supra-Glacial Debris Cover in the Hunza Valley, Karakoram, During 1990∼ 2019. Frontiers in Earth Science, 8, 308.

Žebre, M., Colucci, R. R., Giorgi, F., Glasser, N. F., Racoviteanu, A. E., & Del Gobbo, C. (2021). 200 years of equilibrium-line altitude variability across the European Alps (1901− 2100). Climate Dynamics, 56(3), 1183-1201.

Zekollari, H., Huss, M., & Farinotti, D. (2019). Modelling the future evolution of glaciers in the European Alps under the EURO-CORDEX RCM ensemble. The Cryosphere, 13(4), 1125-1146.

Zemp, M. (2006). Glaciers and climate change: spatio-temporal analysis of glacier fluctuations in the European Alps after 1850 (Doctoral dissertation, University of Zurich).

Zhang, T. (2005). Influence of the seasonal snow cover on the ground thermal regime: An overview. Reviews of Geophysics, 43(4).

Acknowledgements

I would like to thank my supervisor Professor Mauro Guglielmin for providing guidance throughout this research. Thanks also to Professor Nicoletta Cannone for her contribution to one of the papers and for giving me the possibility to stay in her laboratory.
Thank to Silvia, Francesco, Alessandro, Stefano, Silvia and Chiara, for the time spent together in the laboratory and outside.
I'm also grateful to Professor Martin Hoelzle who kindly hosted me for some months at Fribourg University.
Thanks to Dr. Renato R. Colucci and Dr. Andrea Fischer who evaluated this thesis, providing useful comments.
Thanks to Davide, who always helped and supported me. Thanks to my family and friends for always being there.